Structural and Morphological TEM Characterization of GaAs based Nanowires

Dissertation zur Erlangung des
Doktorgrades der Naturwissenschaften (Dr. rer. nat.)
der Fakultät für Physik der Universität Regensburg

vorgelegt von

Marcello Soda

aus San Giovanni Rotondo

durchgeführt am
Institut für Experimentelle und Angewandte Physik
der Universität Regensburg
unter Anleitung von

Prof. Dr. J. Zweck

Structural and Morphological TEM Characterization of GaAs based Nanowires

Dissertation zur Erlangung des
Doktorgrades der Naturwissenschaften (Dr. rer. nat.)
der Fakultät für Physik der Universität Regensburg

vorgelegt von

Marcello Soda

aus San Giovanni Rotondo

durchgeführt am
Institut für Experimentelle und Angewandte Physik
der Universität Regensburg
unter Anleitung von

Prof. Dr. J. Zweck

Promotionsgesuch eingereicht am 22.12.2011
Tag der mündlichen Prüfung: 03.02.2012

Diese Arbeit wurde angeleitet von: Prof. Dr. Josef Zweck

Prüfungsauschuss:

Vorsitzende:	Prof. Dr. K. Rincke
1. Gutachter:	Prof. Dr. J. Zweck
2. Gutachter:	Prof. Dr. D. Bougeard
weiterer Prüfer:	Prof. Dr. J. Repp

Contents

1 III-V semiconductor nanowires **3**

1.1 Definition, general concepts and growth model 3

1.1.1 General growth mechanism 5

1.1.2 Au-assisted growth: thermodynamical and kinetic aspects 7

1.2 Properties of III-V semiconductor nanowires 12

1.2.1 Crystal structure 12

1.2.2 Nucleation theory 14

1.2.3 Shape and morphology 16

2 Low temperature growth of (Ga,Mn)As layers **19**

3 Molecular Beam Epitaxy **23**

3.1 Basic phenomena of MBE growth 23

3.2 Kossel´s model of crystallization 25

4 MBE chamber and sample growth **27**

4.1 MBE chamber 27

4.2 NWs growth 29

5 Transmission Electron Microscopy **31**

5.1 The microscope 31

5.2 Sample preparation 33

5.2.1 NW transfer on carbon film 33

5.2.2 Standard TEM cross section preparation 34

5.2.3 Ultramicrotomy 35

5.3 Conventional TEM techniques 37

5.3.1 High Resolution TEM imaging 37

5.3.2 Diffraction patterns . . . 40

5.3.3 Determination of the NWs crystal structure . . . 41

5.4 Analytical techniques . . . 42

5.4.1 Electron Energy Loss Spectroscopy . . . 43

5.4.2 Energy Dispersive Spectroscopy . . . 45

6 Growth parameters and crystal structure 51

6.1 Ga content of the crystallized droplets . . . 51

6.2 Droplet state during growth . . . 55

6.3 NWs crystal structure and droplet state . . . 57

6.4 Calculation of the Ga content during growth . . . 59

6.5 Summary . . . 63

7 Core/shell heterostructures: crystal structure and morphology 65

7.1 Epitaxial growth and crystal structure . . . 65

7.2 Cross section morphology . . . 74

7.3 Mn segregation . . . 77

7.4 Summary . . . 79

8 Summary 80

Introduction

Nanowires (NWs) are quasi one dimensional structures with an aspect ratio of 100 or more, the smaller length being in the order of tens of nanometers [1].
In general the interest in the realization of quasi one dimensional structures relies in the possibility to study quantization effects like e.g. quantum transport [2, 3, 4, 5]. Also the high surface to volume ratio of the nanowires is of high interest e.g. for increasing the photon emission and absorption efficiency in light emitting diodes and solar cells. [6, 7, 8, 9]. Furthermore the high aspect ratio of nanowires allows the integration of heterogeneous materials in the form of axial, radial or even branched one dimensional heterostructures [10, 11, 12, 13].

Nanowire growth promoted by a seed particle is the common used technique for realizing semiconductor nanowires [1]. The technology evolved following the Vapor Liquid Solid (VLS) growth mechanism developed over 40 years ago [14]. A liquid alloy forms from the seed particle and from the precursor(s) resulting in crystal growth by precipitation from a supersaturated solution. For III-V semiconductors Hiruma et al. developed in the 1990s the growth of wires with dimensions on the nanoscale according to the VLS mechanism. They realized GaAs p-n junctions used for producing nanowire light-emitting diodes demonstrating the potential of III-V nanowires. They also demonstrated the principles of formation of heterostructure interfaces [15, 16]. Due to the variety of semiconductor materials and heterostructures that can be realized, nanowires can find applications in many technological fields. Devices for electronic, optoelectronic and spintronic applications were already realized as e.g. field effect transistors (FETs) or single electron transistors (SETs) [16, 17, 18, 19, 20, 21, 22]. Light emitting diodes for a variety of materials have been fabricated with the advantage of a tunable band gap with nanowire diameter [23, 24]. Lieber et al. realized Si nanowires as highly sensitive biosensors devices, allowing electrical detection of the selective adsorption of molecules [25, 26]. Memory devices based on nanowire heterostructure superlattices show enhanced write speeds compared to conventional memory, and may lead to more efficient memory devices [27].

One of the goals of the research on semiconductor nanowires is the development of a model describing their growth and their general characteristics as e.g. the shown crystal structure or their morphology.
Publications on this topic use a kinematic model and the standard nucleation theory for describing nanowire growth [22-46]. Adatom diffusion length and composition of the seed particle are the principal quantities identified by the autors which determine the morphology and the crystal structure of the axial grown nanowires.

One peculiarity of the semiconductor nanowire growth is that nanowires do not necessarily adopt the crystal structure of the bulk material and crystal phase mixing is commonly observed [47]. This may lower the performance of devices or even make their fabrication impossible. Therefore the achievement of control over the adopted crystal structure is essential and motivates this work.

Ferromagnetic semiconductor nanowires as building blocks for spintronic applications receives increasing attention [48, 49, 50, 51]. The possibility to integrate heterogeneous materials in nanowires provides an interesting approach for synthesizing functional ferromagnet/semiconductor hybrid structures [48, 49, 52, 53, 54, 26, 55]. As a promising material for spintronic applications the ferromagnetic semiconductor (Ga,Mn)As and its magnetic properties were widely investigated in the last decades [56, 57, 58, 59, 60, 61]. A negligible conductivity mismatch between (Ga,Mn)As and GaAs leading to a high spin polarization degree of injected currents is the main advantage of an all semiconductor system compared to a ferromagnetic metal/non magnetic semiconductor system [62, 63].
Ferromagnetic nanowires composing of a GaAs core and a (Ga,Mn)As shell have the objective to allow the study of spin phenomena in low dimensions [64, 65]. The magnetic characterization of the core/shell nanowires shows a Curie temperature of about 20 K [64, 65]. In order to achieve Curie temperatures about 180 K, comparable to those obtainable by (Ga,Mn)As layers [66], optimization of the growth parameters is mandatory and requires the structural and morphological characterization of the nanowires.

In this thesis the crystal structure of GaAs nanowires grown by molecular beam epitaxy is studied with standard transmission electron microscopy techniques. The existing relation between the growth parameters and the adopted crystal structure is investigated, and the necessity to relate the observed crystal structures to nanowire specific parameters and not to global growth conditions is introduced.
(Ga,Mn)As was deposited by molecular beam epitaxy as shell on GaAs core nanowires [64]. The transmission electron microscopy analysis on the crystal structure and morphology of the heterostructured nanowires, as well as the investigation of Mn segregation effects contribute to the optimization of the shell growth parameters indicating the major thermodynamical and kinetic effects affecting the radial growth of (Ga,Mn)As.

This thesis is structured as follows: in chapter 1 and 2 the basics of nanowire and (Ga,Mn)As growth are sketched, followed by the principles of molecular beam epitaxy in chapter 3. The experimental techniques are described in chapter 4 and 5.
The results are presented and discussed in the experimental part. Chapter 6 is dedicated to the crystal structure investigation of the core nanowires, presenting new achievements obtained by high resolution transmission electron microscopy.
The (Ga,Mn)As crystal structure of nanowire shells is investigated in chapter 7 together with manganese segregation effects.

Theoretical aspects

1 III-V semiconductor nanowires

Description and analysis of the morphology and the crystal structure of nanowires requires on the one hand to assign their growth to a general growth model and on the other hand to identify and describe particular processes involved in forming their shape and their atomic arrangement.
These two tasks compete with each other due to the wide range of growth methods (MOVPE, MBE, VPE, CBE, CVD[1]), materials (e.g. III-V, II-VI and IV semiconductors) and specific growth techniques (metal catalyst, self catalyzed, without catalyst) used for the realisation of semiconductor nanowires.
This chapter describes common concepts on nanowires growth and presents a general model that answers the question *why do nanowires grow?*

1.1 Definition, general concepts and growth model

Nanowires (NWs) are one dimensional structures with an aspect ratio of 100 or more, the smaller length being in the order of tens of nanometers. In figure 1.1 a Scanning Electron Microscopy (SEM) micrograph of free standing NWs should impart an idea of the aspect of the investigated NWs.

A nanowire has not to be strictly a wire. It could be for example a stripe realized structuring a given bulk material [67, 68]. The way in which NWs are realized can be classified in top-down and bottom-up techniques. *Top-down* approaches are based on lithographic, electron beam or laser structuring, and are also optimized to realize free standing patterned NWs [69]. The resulting device properties are limited by fabrication induced damage and imperfect lateral control [70]. Such techniques are always restricted to the wavelenght of the structuring beam.
Bottom-up techniques allow a variety of elemental composition maintaining the crystal quality of bulk material. Those are based on epitaxial growth and on a self assembling principle yielding thus nanometer scale structures [1].

[1] Metal Organic Vapor Phase Epitaxy (MOVPE), Molecular Beam Epitaxy (MBE), Vapor Phase Epitaxy (VPE), Chemical Beam Epitaxy (CBE), Chemical Vapor Deposition (CVD)

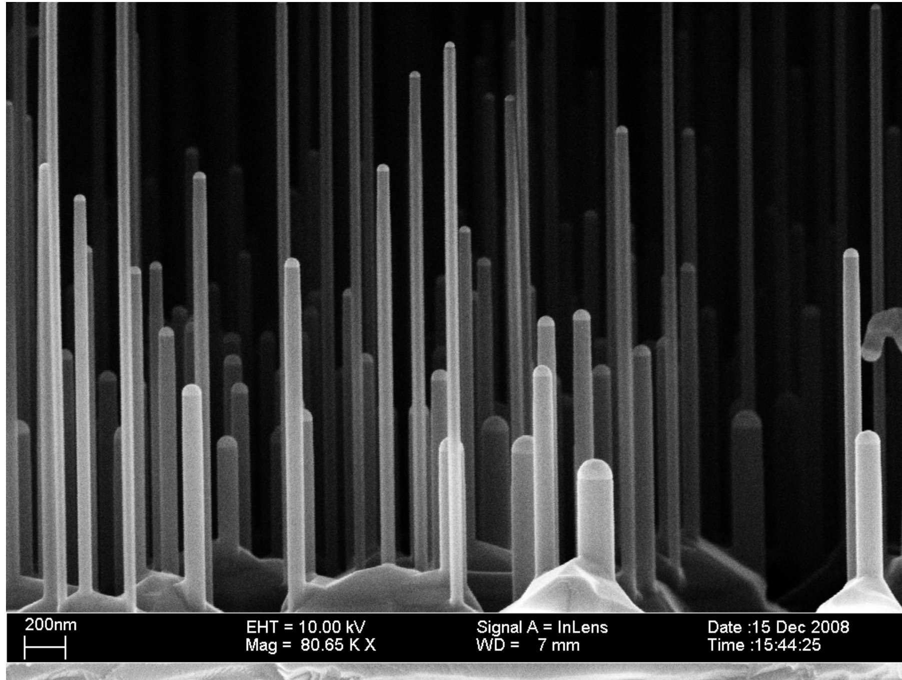

Figure 1.1: ***SEM micrograph of GaAs NWs*** - *NWs grow perpendicular to the substrate surface. The length of the NWs is influenced by the dimension of the gold droplet which can be seen at the top of each wire.*

Since one dimensional epitaxial growth does not occur normally on a planar substrate, an element breaking the crystal symmetry has to be introduced in the growing system. Typically a metal particle acting as *catalyst* is used. The technique is called *particle-assisted growth*. In figure 1.1, on top of each NW the presence of a crystallized particle can be recognized.
By definition a catalyst is a material that increases the rate of a reaction by lowering its activation barrier. Since there is no agreement whether the activation energy of NWs growth changes in the presence of a seed particle or not, Dick concludes that particle catalysis may play a role in some systems, but is not a universal effect and is not sufficient to explain the general mechanism of particle-assisted NW growth [1, 71, 72, 73, 74, 75]. In the case of MOVPE the growth of crystals is by chemical reaction and the presence of a catalyst enhances the reaction between the precursor and the substrate. The growth rate of the crystal underneath the liquid droplet is higher than the growth rate of the substrate.
In the specific case of MBE, catalysis does not occur because no chemical reaction is involved in the growth.
The expression catalyst particle is nevertheless widely used and indicates that the introduced material promotes one dimensional growth. The particle determines also the diameter of the wire [5].
Au is the most used material as seed particle. It is relatively inert and does not react with gas phase carriers. Au performs well as catalyst particle for a wide range of materials interacting with the growth substrates forming solid solutions, binary compounds and eutectic melts [76]. Many stable compounds between Au and the group-III materials exist [77, 78]. These eutectic mixtures have intermediate melting points between that of Au and that of the corresponding group-III material [1].
Au forms an eutectic melt with Ga, with an eutectic point of about 350 °C [79]. For GaAs growth to occur, the Au catalyst has not to be strictly liquid. NWs growth from Au particles

was observed for growth temperatures below the eutectic temperature of the Au-Ga alloy [1, 32].

III-V semiconductor NWs that grow from particles composed of one of the components of the semiconductor are called *self catalyzed* [80, 81, 82, 83]. For GaAs NWs the catalyst is a Ga particle. Since some experiments have shown evidence of Au atoms incorporated in Si NWs during growth, self catalyzed growth techniques are of great interest for obtaining pure crystalline phases avoiding degradation of the optical and electrical properties of NWs [84].

More generally it has been demonstrated that one dimensional growth from a particle occurs in many different techniques (MOVPE, MBE, VPE, CBE) using different materials (Si, III-V and II-VI semiconductors) and showing different phases of the particle (solid, liquid). Generally the particle-assisted growth is described as a three phase system as for example the Vapor-Liquid-Solid (VLS) theory does, where NWs growth depends on thermodynamic conditions influencing the state of the particle and kinetic processes governing the mass transfer. Those depend on the growth system, growth method and material used. Developing a *NW growth model* is therefore a non trivial task since a consistent description cannot depend either on the state or properties of the supply phase, or on the state or material type of the particle, and has to be general to describe all the results that have been reported [1, 85].

1.1.1 General growth mechanism

Wagner and Ellis first proposed a growth mechanism called Vapor Liquid Solid (VLS) for their Au-assisted grown Si whiskers. It can be summarized as follows [14]:

- Au and Si form a low temperature liquid alloy
- the Au-Si alloy has a sticking coefficient of one for the precursor material
- Si precipitates from the particle at the interface between solid Si and liquid alloy.

According to the VLS mechanism Si whiskers grow due to the enhanced capability of the liquid alloy to accommodate Si atoms in respect to the other surfaces in the system.

Wacaser et al. expanded the VLS mechanism to a more general description of the growth mechanism, calling them *Preferential Interface Nucleation* (PIN) [86].
In this model any three phase system is represented. The phase or composition of supply, collector and crystal (see figure 1.2, left), does not influences the growth mechanism but only NWs properties.
During particle-assisted growth accommodation of the growth species in the collector is not ideal, even with a liquid, because it is a saturated solution. The accommodation will not be ideal because thermodynamically the chemical potential in a saturated accommodating solution will be the same as the chemical potential in the supply [86].
This will cause the accommodation process to stop.
The phase of the collector becomes therefore irrelevant for the growth process, it must only be able to collect material and become supersaturated. For this reason Wacaser et al. propose to adopt the terminology supply and collector, that relates to the function fulfilled from the material precursor and the particle, instead of indicating their specific phase.

Moreover the model indicates that *supersaturation* conditions alone, defined as supply-collector $\Delta\mu_{sc}$, collector-crystal $\Delta\mu_{sk}$ and supply-crystal $\Delta\mu_{sk}$ differences of chemical potential of the growth species, does not provide one dimensional growth. In crystal growth supersaturation is the thermodynamic driving force and in a three phase system it will favor the growth at the supply-crystal interfaces because of its higher value (see figure 1.2, left) [86, 87].

The *local increase of concentration* at the collector-crystal boundary due for example to kinetic factors or temperature gradients is one condition that may provide one dimensional growth [86].
This represents the main difference between the growth model proposed from Wacaser et al. and the VLS model. Not the accommodation coefficient of the liquid phase of the particle, but a local increase of concentration of growth material in the particle has to be identified as the general argument for explaining the NWs growth mechanism.

The most probable site for nucleation to occur is the Three Phase Boundary (TPB) defined as the line connecting all three phases.
At the TPB the supersaturation is high because the nucleus is in direct contact with the supply phase, yielding a high concentration of growth material. The Gibb´s free energy can be minimized because of the possibility for the nucleus to minimize the total surface energy, changing the ratio of lateral facets in contact with the supply and in contact with the collector. In figure 1.2 right, the model describing the nucleation at the TPB is shown. Wacaser et al. suggest therefore that the TPB is the most preferential interface for nucleation.

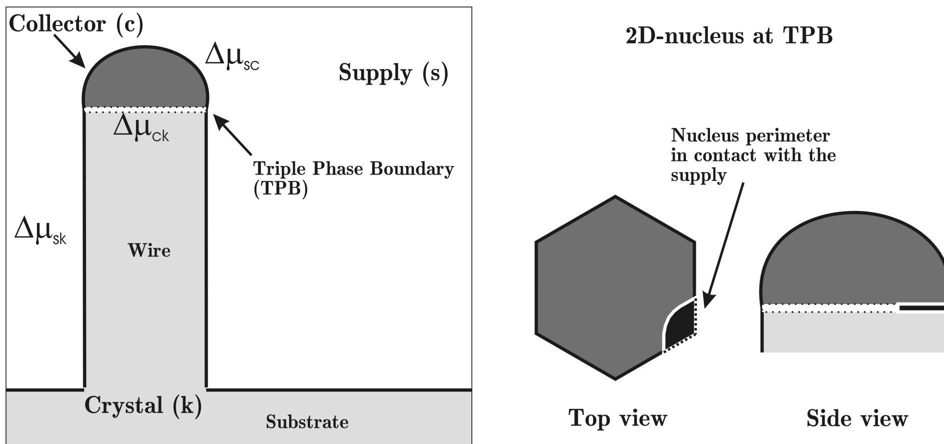

Figure 1.2: ***Preferential Interface Nucleation (PIN) growth model*** - *Left, model of a NW explaining the terminology supply (s), collector (c) and crystal (k). Supply-collector and supply-crystal differences in chemical potential μ favor the growth at the supply-crystal interface ($\Delta\mu_{sk} > \Delta\mu_{sc}$). However a local increase of concentration of the growth species at the triple phase boundary enhances the wire growth. The triple phase boundary coincide with the perimeter of the supply-crystal interface directly under the droplet. Right, most probable position of a 2D nucleus. The portion of the perimeter of the nucleus in contact with the supply can adjust in order to minimize the change in Gibbs free energy. The cross section of NWs is accounted to be hexagonal, reproducing the atomic arrangement on the (111)B surface.*

Preferential nucleation in particle-assisted nanowires systems is treated also by other authors [88, 89, 33]. There are different approaches to justify the enhanced nucleation probability at the TPB and a consistent explanation cannot be deduced.
Cheyssac et al. e.g. describes the TPB as the point of minimum curvature, where mobility is lower and thus nucleation highest.
In these works the common result is that nucleation is kinetically hindered on the substrate and wire facets, but the collector-crystal interface acts as sink.

Even if the particle-assisted growth of GaAs NWs by MBE can be generally regarded to be a consequence of PIN, it has also to be considered as result of an interplay of thermodynamical and kinetic processes influenced by the growth system and its growth parameters as e.g. temperature and partial pressures.
Analysis of morphology and crystal structure of NWs has to take into account NWs growth conditions. Moreover the PIN mechanism describes the growth in the situation in which NWs are already formed and does not provide a complete picture of the growth, i.e. it does not describe how NWs growth starts. Only the general growth mechanism is indicated.
As described by Kolasinski the growth of NWs is accounted to proceed under three different regimes that he called *initiation*, *steady state* and *termination*. Each of them can influence the properties of the wires respectively in their lower, middle and upper part [85].

1.1.2 Au-assisted growth: thermodynamical and kinetic aspects

In order to provide a general picture of NW growth three different growth phases are introduced: initiation, steady state and termination.
Each of them performs a different task and therefore corresponds to different settings of growth parameters. Theoretical models and experiments will be discussed, in order to introduce the most important processes involved in the MBE growth of GaAs NWs.

Initiation

Prior to NW growth, the catalyst material has to be deposited on the substrate. Techniques using aerosol phase or lithography can produce particles with controllable size [90, 91]. The most used technique is the evaporation of a thin Au film on the native GaAs oxide or on a clean GaAs surface.
The initial phase of the Au-assisted growth of GaAs NWs includes the formation on the substrate surface of the gold particles and the achievement of the thermodynamical equilibrium of the system.
Annealing of the thin Au film at high temperatures, typically about 550°C promotes the formation of Au droplets due to Ostwald ripening, and in the case that the thin film was deposited on the native GaAs oxide, its desorption [85].
The size of the droplets can be controlled only indirectly by changing the thickness of the film, the annealing time, the temperature and the pressure in the MBE chamber.

In an MBE chamber, annealing of GaAs substrates occurs under As overpressure in order to prevent a strong incoherent dissolution of the substrate surface. The latter would happen due to the different partial pressures of As and Ga [92]. No Ga is supplied to the system in this phase. Annealing at temperatures above 400 °C produces liquid Au particles [93]. Under these conditions the droplet exchanges material with the substrate and forms an Au-Ga

eutectic. It is assumed that during annealing As, and in general the group-V element, is not incorporated into the droplet. For temperatures below 600 °C no stable phase for Au-As or Au-Ga-As alloys exist [1].
In figure 1.3 the calculated phase diagram of the Au-Ga alloy is shown.
A binary phase diagram depicts the stable condensed phases formed by a two component system as a function of temperature and overall composition. The temperature composition relationships appear in the phase diagram as lines and curves called phase boundaries. The phase boundary separating the solid phases from the liquid phase is called liquidus. The system moves along the liquidus when the temperature is changed.
The Ga-Au eutectic has a liquid phase at temperatures about 350 °C only if the gallium molar fraction in the droplet is more than 30%. At typical growth temperatures of about 600 °C the solubility is continuous because of the liquid phase of the binary system.
An eutectic mixture is characterized by at least one local minimum of the liquidus line. The Au-Ga phase diagram shows two main eutectic points (see figure 1.3). The eutectic points represent local minima of the Gibb´s free energy of the system and are the points to which the system tends to evolve when the growth temperature is lowered and material exchange between the Au-Ga droplet and the substrate or the vapor phase occurs.
When the temperature decreases below an eutectic point as e.g. that corresponding to about 440 °C with a Ga content of about 0.55 mole fraction, two distinct phases of the Au-Ga alloy form, AuGa and $AuGa_2$. This region of the phase diagram below the liquidus line is characterized by a solubility gap. The overall Ga mole fraction has to be 0.55.
A detailed description of the Au-Ga phase diagram and of its calculation can be found in [79].
The reported phase diagram is calculated for a Au-Ga solution at standard conditions in thermodynamical equilibrium. The results of investigations on the crystallized Au-Ga droplet

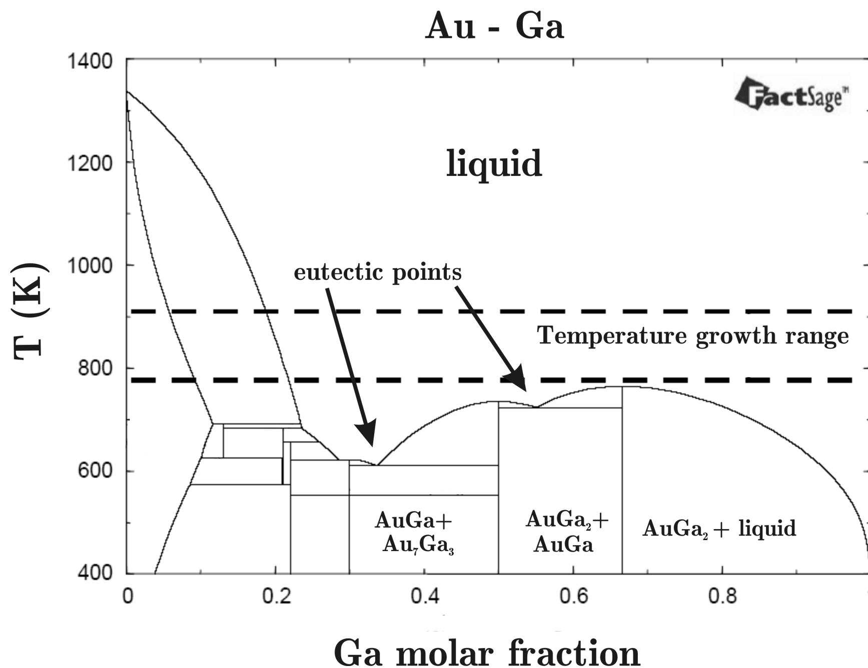

Figure 1.3: ***Au-Ga phase diagram*** *- Au-Ga binary phase diagram redrawn from [79]. The eutectic point at ca. 600 K implies a Ga molar fraction of about 0.30. At typical growth temperatures of about 600 °C any Ga content > 0.20 is allowed.*

can be interpreted using the properties of the phase diagram. During the NW growth however, thermodynamic equilibrium for the droplets cannot be assumed. The phase diagram should be therefore used as a general description of the Au-Ga alloy, indicating its possible solid phases. Particular evolutions of the state of a single droplet cannot be deduced.
During growth different NWs will be characterized by similar values of their thermodynamical parameters, but identical growth conditions for each NW cannot be realized as long as a precise control over their initial Au droplet dimension and over their equilibrium droplet composition cannot be achieved. To use the thermodynamical state of the droplet during growth in order to predict the NW morphology and the NW crystal structure presumes that the Ga content in the droplet is known. A method for its derivation is presented in chapter 6.

In the *initiation* phase two main processes occur:

- desorption of oxides present at the substrate/Au film interface
- material exchange and accumulation in order to define thermodynamical and mechanical equilibrium.

The state of the particle is liquid, but its composition remains unknown, also during growth. The Ga content is assumed to be in the range 0.3-0.5 [34].

Steady state

The steady state regime corresponds to obtaining and maintaining the growth conditions in the MBE chamber, determined by the growth temperature and the fluxes of the group V and III elements.
The steady state assumption implies that the chemical potential and the size of the droplet are constant during growth, giving rise to a constant NW diameter [85].
This picture of the growth is an approximation used for developing theoretical models describing the growth rate dL/dt of the NWs, where L is the NW length [34, 35, 36, 37, 38]. It is useful for understanding the limiting processes of the growth and to link those to physical quantities and growth parameters.
Depending on the features of the NWs one is interested in, the steady state approximation can be considered or not. Tapering of NWs, for example, cannot be described if the steady state assumption is made.
The major contribution to the development of a model of MBE growth of GaAs NWs is given by Dubrovskii et al. [34, 36, 39, 40, 41, 42]. The theory is based on the solution of diffusion equation for the stationary adatoms concentration on the substrate surface and on the sidewalls of NWs.
NW growth takes place simultaneously to two dimensional (2D) growth on the substrate. Efficient growth conditions allow a much higher growth rate for NWs than for the substrate. Both growth processes compete for the material, so mass transport has to occur.
The kinetic processes considered in the model are

- substrate and sidewall adatom diffusion
- the direct impinging of part of the molecular beam on the droplet surface
- desorption from the crystal and droplet surfaces (see figure 1.4, center).

The diffusion equation are solved imposing boundary conditions considering the continuity of chemical potential and adatom flux at the interfaces, at the bottom and the top of the

NW. Stationary concentration of adatoms on the substrate surface away from the NW is a further boundary condition. The model does not consider any interaction between NWs.

The growth rate depends on the length L of the NWs in a non linear way. The evaluation of the analytic solutions of the differential equations of the model attests the major role in the growth dynamic of the adatom diffusion length, λ_f, on the NW sidewalls. In figure 1.4, left, NW length, diffusion lengths, incident and contact angle are sketched.
NWs axial growth consist of at least two phases. For L $>>\lambda_f$, in figure 1.4, right, the fluxes of adatoms from the substrate and sidewalls to the particle can be negative, indicating a mass transport towards the substrate. The material accommodated into the droplet arises from direct impinging and diffusion of sidewall adatoms within a diffusion length. The difference in supersaturation $\triangle\mu_{substrate} = \mu_{supply} - \mu_{crystal}$ and $\triangle\mu_{sidewalls} = \mu_{supply} - \mu_{sidewalls}$ determine if the material collected on the lower part of the sidewalls and on the substrate contribute either to substrate or to radial growth.
For L $<\lambda_f$ all three factors, direct impinging, diffusion from sidewalls and substrate contribute to the axial growth (see figure 1.4, center). Qualitatively the growth rate is a function with one maximum. It increases in the first part of the growth because of the increasing collection area on the sidewalls. After reaching a maximum value, which depends not only on λ_f but also on the incident angle α and the NW density due to shadowing effects, not considered in the model, decreases to a constant value due to the vanishing contribution of the substrate adatoms.
The analytical model considers the nucleation rate at the TPB as a function of the Ga supersaturation of the droplet. The higher the Ga flux toward the droplet, the higher the nucleation rate.
The majority of the NWs investigated in this work are supposed to belong to the case L $<\lambda_f$. Only the highest NWs, those higher than 3 μm, could belong to the case L$\backsimeq \lambda_f$ in which the adatoms on the substrate have a lower probability to reach the droplet and could nucleate on the substrate or on the sidewalls [95]. In all other cases the growth situation corresponds to that illustrated in figure 1.4 center, where the adatoms collected on the entire NW surface diffuse to the droplet and contribute to axial growth. The Ga adatoms flux toward the droplet increases with the increasing height of NWs because of the increased collection area within one diffusion length.

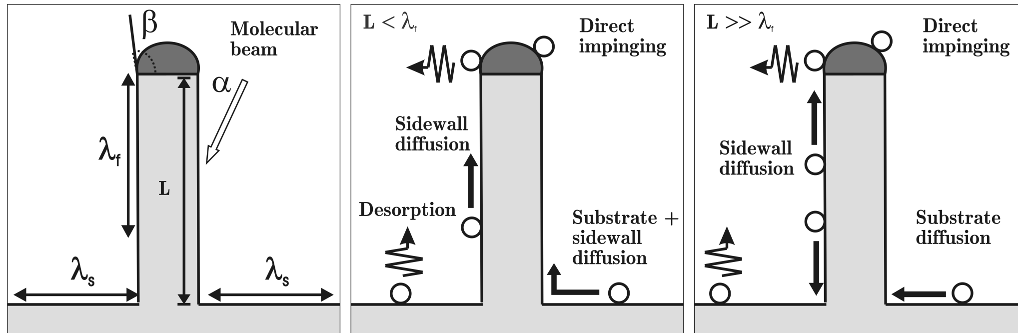

Figure 1.4: ***NW growth model*** - *The presented model is developed by Dubrovskii et al. [93, 34, 43, 94] Left, NW and diffusion length are sketched. The ratio between these quantities determines the growth regime. Center, the case L$<\lambda_f$ is represented. Adatoms diffuse toward the particle and contribute to the axial growth. Right, the case L$>>\lambda_f$ is depicted. Only direct impinged atoms and adatoms one diffusion length apart from the TPB contribute to the axial growth. Within a diffusion length apart from the substrate, adatoms diffuse toward the substrate.*

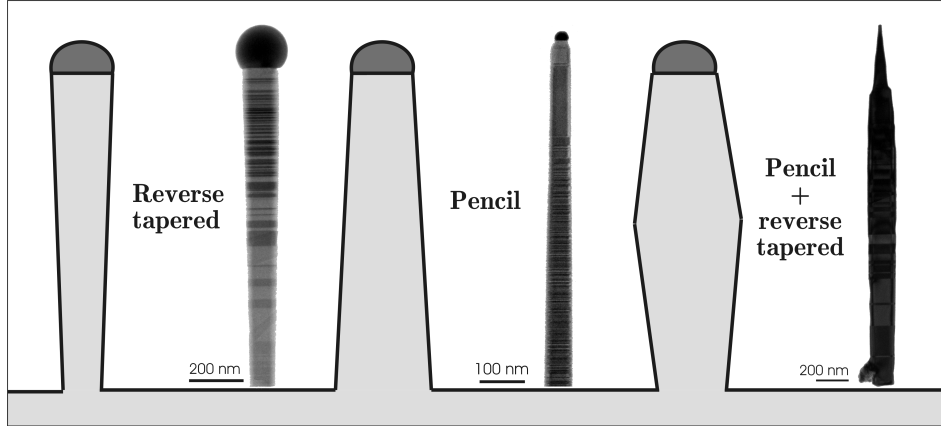

Figure 1.5: ***Tapering effects*** *- Left, the reverse tapered profile of a NW is either due to an increasing droplet dimension during growth, or due to shadow effects enhanced by low temperature growth. The latter is related to the growth of shell and is due to a high NW density. Center, the pencil shape is the result of an increased nucleation probability on the facets of the lower part of the NW or of the decrease of the droplet volume. Right, both pencil and reversed tapered shapes appear if the growth conditions change during growth so that the adatom flux toward the droplet first increases and than decreases. [96].*

It is generally agreed, that the MBE growth rate of III-V NWs is limited by diffusion processes [1, 36, 38]. The Dubrovskii model can reproduce experimental time dependencies of NWs height within the uncertainty given by the parameters not known experimentally (e.g. droplet composition during growth, surface energies, adatoms lifetime).

For theories modeling quantities of NW growth other than the growth rate dL/dt, many authors abandon the steady state approximation and allow the liquid droplet to change its chemical potential and/or its volume. This is assumed to occur not as consequence of a change of temperature or partial pressures, but of a variation of material collection rate.
This aspect will be considered in chapter 6 in order to develop a model that explains the change of the observed crystal structure with an increasing Ga content in the droplet.
An increasing or decreasing volume of the droplet during growth has been considered by Schwarz et al. in developing a dynamical model of NW growth in order to predict their final shape [96]. As input for the simulation the authors use a non stationary flux of atoms entering the droplet. The predicted profiles show the typical pencil and reverse tapered shapes observed experimentally (see figure 1.5) [96].

The steady state regime is the part of the growth corresponding to the formation of the NW body. In an ideal case the NWs are perfect cylinders, and their axial growth is described by the evolution of the growth rate dL/dt as proposed by Dubrovskii et al.
In reality deviation from the steady state conditions occur and the time dependent droplet state influences not only the morphology but also the adopted crystal structure, as will be explained in subsection 1.2.

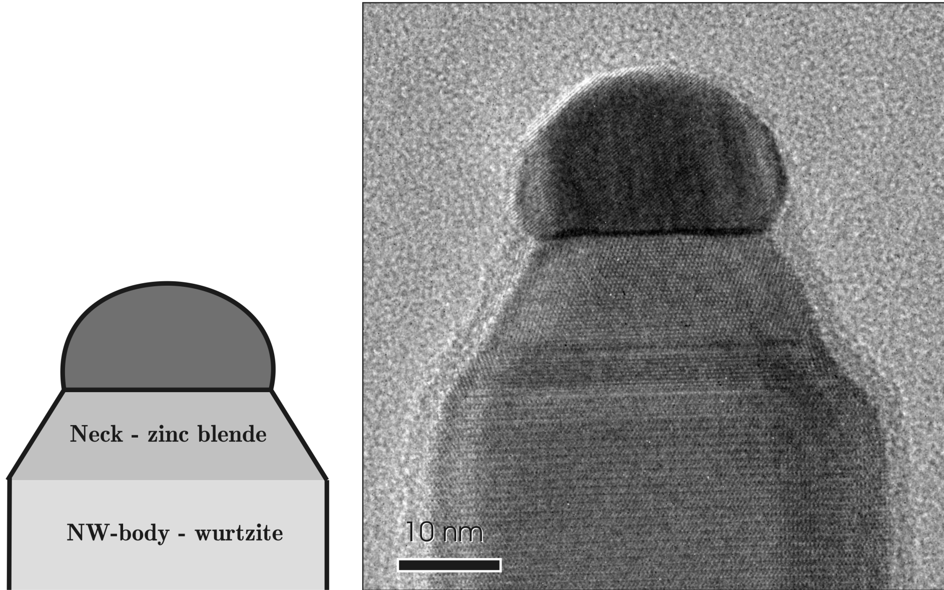

Figure 1.6: ***Neck associated with the termination regime** - Left, model of a cooling neck. The last few monolayers of the NW growth are associated with a strong tapering effect. The neck has a zinc blende crystal structure. Right, a High Resolution Transmission Electron Microscopy (HRTEM) image of a neck.*

Termination

The termination regime corresponds to the last phase of the growth. Transient conditions before growth stop produces characteristic NWs features.
The shape and the crystal structure of the part of the NWs direct below the droplet is influenced by the sequence how the NW growth is terminated. Typically the Ga cell is closed simultaneously with decreasing the substrate heating, whereas As is still supplied until the substrate temperature reaches 400 °C.
As long as the temperature is higher than 400 °C, although Ga is no more supplied, new material will be deposited into the wire. The Ga in the droplet can interact with the As vapor that is still supplied to the system. Closing the Ga and As cells simultaneously, however, impedes any further axial growth [44].
Depending on the initial conditions and the sequence of effusion cells closure and heating interruption, the droplet eventually consumes Ga changing its chemical potential and its volume. NWs can show tapering to smaller diameter and a change in the crystal structure like the NW in figure 1.6 [44, 45, 97]. The HRTEM micrograph shows a tapering effect and the occurred change in the crystal structure.

1.2 Properties of III-V semiconductor nanowires

1.2.1 Crystal structure

In GaAs the metal atoms (Ga) form ionic/covalent bonds with As. Each atom is bonded by four sp^3 hybridized atomic orbitals, leading to a tetrahedral coordination geometry (see figure 1.7, left).

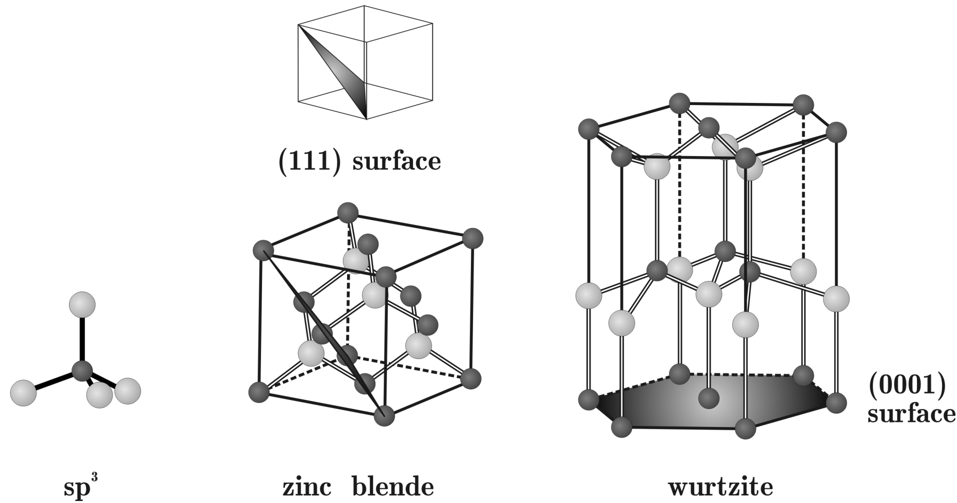

Figure 1.7: ***Tetrahedral coordination, zinc blende, wurtzite*** *- Left, the sp^3 hybridization lead to a tetrahedral geometry. Center, the zinc blende crystal presents two interpenetrated cubic lattices. The {111} surfaces are closed packed surfaces. Right, the wurtzite crystal presents two interpenetrated hexagonal lattices. The {0001} surfaces are closed packed surfaces.*

The most stable crystal structure of bulk GaAs is cubic sphalerite (or zinc blende, ZB) [98]. When forming NWs GaAs mostly adopts the hexagonal wurtzite (WZ) structure.
Both structures consist of two equivalent interpenetrating lattices, one containing gallium atoms and the other As atoms. ZB is composed of two face centered cubic (fcc) lattices, WZ of two hexagonal lattices. Each lattice contains either Ga or As atoms (see figure 1.7). The planes {111} for ZB and {0001} for WZ are closed packed planes. Since the particle-assisted growth of NWs belongs to the self assembling methods, NWs growth most often occurs along the <111> ZB or <0001> WZ crystallographic directions, independently of the substrate surface orientation [46]. The formation energy can be minimized arranging atoms in close packed planes. In order to obtain vertical free standing NWs, GaAs (111)B substrates are used. If one considers respectively the {111} ZB or {0001} WZ planes, all Ga atoms are coplanar and all As atoms are coplanar. In the cubic notation the (111)A plane is Ga terminated and the (111)B plane is As terminated.

Since NW growth is a layer by layer growth, crystallization in ZB or WZ structure depends on the relative position of the new nucleated monolayer (ML) to the previous one. A ML is made of two planes of atoms, Ga below and As above (see figure 1.8). In the <111> crystal direction the ZB crystal phase exhibits a repeated stacking sequence of three distinct MLs. The WZ crystal phase is on the other hand described by a stacking sequence of two distinct MLs. The two stacking modes are usually referred to as ABCABC... (ZB) and ABABAB... (WZ).
In both structures any gallium atom sits directly above the As atom of the underlying ML and the A, B or C character of each ML is entirely determined by the lateral position of its As atoms. The energetic difference between ZB and WZ crystals arises from the difference in the third nearest neighbor atom spacing [1].
If one considers respectively the ZB or WZ crystal structures projected along the $<1\bar{1}0>$ ZB or $<11\bar{2}0>$ WZ direction, the new stacked ML is in ZB position if it maintains the same

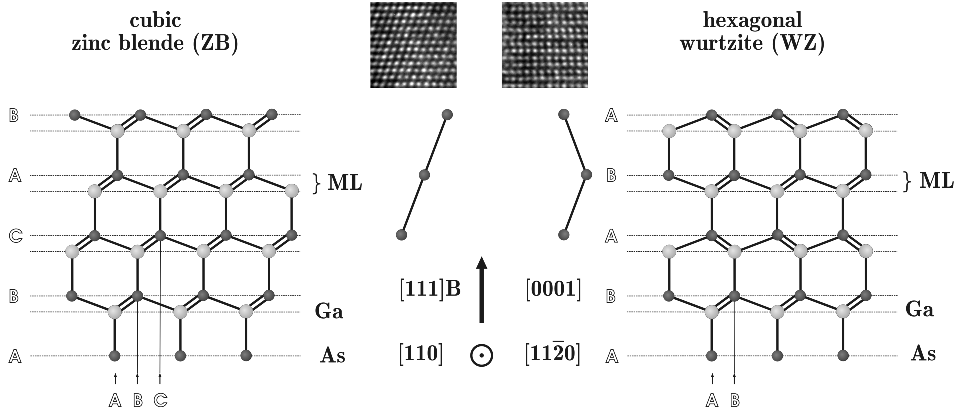

Figure 1.8: ***Stacking sequence of zinc blende and wurtzite*** *- Left, zinc blende stacking sequence. The ABCABC stacking sequence is characterized by the same orientation of the tetrahedron in each monolayer (ML). Two As or Ga atoms are stacked both at an A, B or C position after three ML. The stacking sequence is ABCABC. The upper HRTEM picture on the left shows an example of the ZB stacking sequence observed in the* [1$\bar{1}$0] *projection. Each point represents a ML. Its schematic representation is drawn below the micrograph. Right, wurtzite stacking sequence. The tetrahedron is rotated by a multiple of* $\pi/3$ *every ML. In the* [11$\bar{2}$0] *projection this effect appears like a reflection of the atomic bonds. In this way only two positions, A and B, are allowed. After two MLs two As or Ga atoms sits at the same position. The stacking sequence is ABAB. The upper HRTEM picture on the right shows an example of the WZ stacking sequence observed in the* [11$\bar{2}$0] *projection. Its schematic representation is drawn below the micrograph.*

projected orientation of the As bonds of the previous ML and is only translated in order to positioning the Ga atoms over the As atoms of the previous ML. It is in WZ position if beside the translation also an orientation of the bonds specular to the <0001> direction occurs (see figure1.8).

Since the energy difference between the two type of nuclei is small[2], small changes in the growth conditions e.g. concentration of the atomic species in the droplet, surface reconstruction, temperature and pressure, can induce a change in the nucleation position (ZB or WZ) [46]. Since any sequence of monolayers is admissible, WZ NWs showing twin boundaries and stacking faults (SF), ZB NWs with twin boundaries and SFs, or a random sequence of ZB and WZ MLs can be observed (see figure 1.9).
The control over the process governing the emerging of SF and twin boundaries is a crucial task for developing defect free nanostructures for e.g. optoelectronics [47].

1.2.2 Nucleation theory

The creation of a SF requires a relative low energy and differently from the bulk material, in a NW the presence of a SF does not imply the formation of a dislocation inside the crystal [99].
Since ZB is the most stable structure in bulk GaAs, one can think of the WZ structure to be a ZB crystal with an infinite sequence of twin boundaries [98]. The WZ structure is the mainly observed structure in MBE grown GaAs NWs.

[2]the difference in cohesive energy between ZB and WZ bulk GaAs is about 24 meV per III-V pair [98]

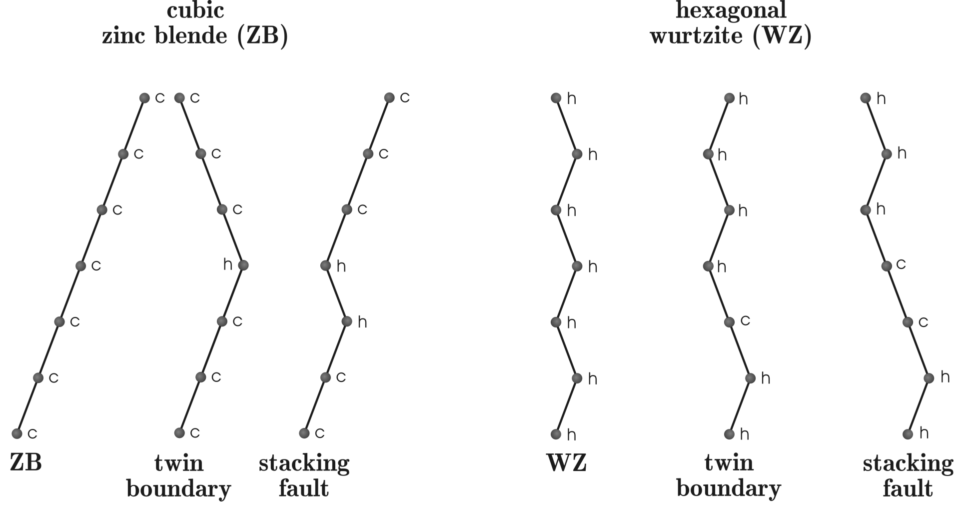

Figure 1.9: ***Principal stacking faults in zinc blende and wurtzite crystals*** *- Left, comparison of faulty stacking sequences with the ZB structure. Right, comparison of faulty stacking sequences with the WZ structure. The hexagonal (h) or cubic (c) character of the ML, represented in the figure as a dot, depends on the previous one (see figure 1.8). Any sequence of combinations of h and c MLs is admissible.*

The formation of WZ crystals could arise from the contribution of the lateral facets or edges energy to the total energy [100, 101]. Provided those specific energies are less for WZ than for ZB a critical radius for the occurrence of the ZB crystal structure can be calculated. For NWs with diameters less than 10 nm WZ is predicted to be the energetically favorable structure due to the high surface to volume ratio. The theory developed by Akiyama et al. however does not provide an explanation for the occurrence of WZ in NWs with diameter of the order of 100 nm [33, 46, 101].

Using classical nucleation theory, Glas et al. suggest, that, if the nucleation occurs at the TPB, WZ nuclei in GaAs NWs are energetically more favorable than ZB nuclei [33]. They demonstrate that the TPB is the point of the collector-crystal interface where the nucleation energy is minimized due to the substitution of part of the liquid-supply interface with the nucleus-supply interface, which has a greater chemical potential difference.
The considered parameter are the surface energies γ_i, the contact angle β, and the supersaturation $\triangle\mu$. The analysis is based on an estimation of this quantities during growth. The author impose also a *"high supersaturation"* regime as necessary condition for the nucleation of a new ML in WZ position. The supersaturation has to be larger than a critical value to overcome the created stacking fault.
It is generally agreed, that for the MBE Au-assisted growth method of GaAs NWs the formation of ZB is favored by *"low supersaturation"* conditions and the formation of WZ is favored by *"high supersaturation"* conditions, low and high meaning low and high molar fraction of atomic species in the liquid particle.
The condition for nucleation at the TPB to occur is given by

$$\Delta\gamma = \gamma_{WV} - \gamma_{SL} - \gamma_{LV} sin\beta < 0 \tag{1.1}$$

where γ_{WV} is the WZ sidewall surface energy (wire-vapor), γ_{SL} the nucleus surface energy

(solid-liquid), γ_{LV} the droplet surface energy (liquid-vapor) and β the contact angle of the droplet. $\Delta\gamma = \gamma_{TPB} - \gamma_C$ is the difference in surface energy for nuclei at the two considered position: at the TPB and at the center of the droplet. Since the nucleation at the TPB favors the formation of a WZ nucleus and the nucleation at the center favors the formation of a ZB nucleus [33, 102], a positive value of $\Delta\gamma$ will favor the nucleation at the center of the droplet and therefore a ZB nucleus.
Typically *"low supersaturation"* conditions are those during transient phases at the beginning and at the end of the growth, when the gallium content in the droplet is less compared to that present in the steady state regime, when *"high supersaturation"* conditions prevail [33, 45].
High and low supersaturation conditions are general description of the thermodynamical state of the particle. Since the content of gallium in the droplet during growth is unknown, there is a lack of definition of when NW growth occurs under high or low supersaturation regimes.
MBE grown GaAs NWs crystallize mainly in the WZ structure. No general relation between the final observed crystal structure and growth parameters can be deduced from the publications on Au-assisted GaAs NWs.
For Ga-assisted grown NWs, however Spirkoska et al. and Cirlin et al. assert that a major role in determining the crystal structure and the growth rate of the NWs is played by the As flux in the chamber [47, 102]. ZB crystal structure is favored with a high As flux and WZ crystal structure is favored with a low As flux.

The described theories, which attend to explain the formation of WZ or ZB NWs will be used for the explanation of the results of the investigations on the NWs crystal structure.

1.2.3 Shape and morphology

In an ideal case all grown NWs are rods with sidewalls parallel to the growth direction. In the most cases, however, tapering occurs (see figure 1.5). If tapered, a NW can assume a pencil shape, a reversed tapered shape or both at once. Growth temperature, material flux and ratio of group V and group III elements influences the morphology of NWs.
A relative low growth temperature (400-500 °C) favors the radial growth on the sidewalls of the NWs. Since the axial growth is still permitted in this temperature range, NWs assume a pencil shape [29, 30].
The reversed taper morphology arises if shadowing effects occur. Due to the high NWs density and the tilted incoming molecular beam the lower part of a NW cannot collect as much material as the upper part [44]. Also the increase in droplet volume during growth is considered as reason for an increasing NW diameter [28].
Depending on the evolution of the growth conditions a NW can exhibit also both pencil shape and reversed tapered morphology [44].

III-V zinc blende NWs with twin boundaries show a particular morphology. The lateral facets of a NW segment between two twin boundaries belong to the $\{\bar{1}\bar{1}1\}$ family. These are not parallel to the growth direction and develop in the side view a zig zag profile (see figure 1.10) [46, 103].
The zig zag profile is therefore associated to the presence of a high density of SFs. Since not every faulty ZB NW shows a zig-zag profile, their origin is not well understood.

GaAs NWs show predominantly a hexagonal cross section, even if also triangular or circular

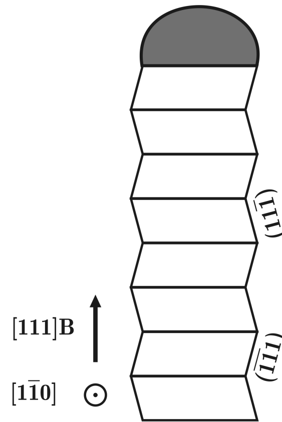

Figure 1.10: ***Zig zag profile of a ZB NW*** *- The characteristic profile of a ZB NW decorated with twin boundaries can be used for the identification of ZB segments with a high density of stacking faults. The lateral facets are not parallel to the growth direction and produces the zig zag contour.*

sections can be found [29, 31, 104].
In the case of hexagonal NWs the most observed lateral facets belong to the $\{11\bar{2}\}$ ZB planes family, corresponding to the $\{10\bar{1}0\}$ WZ planes.
$\{110\}$ ZB are not commonly developed lateral surfaces, even if one would expect it. The $\{110\}$ surfaces are neutral, they possess the same number of Ga and As atoms. Therefore they should be more stable.
The surface reconstruction during growth remains unknown [46]. Dick et al. note that it is not obvious that lateral facets with the lowest surface energy will form during growth, because NWs grow layer by layer [46].

2 Low temperature growth of (Ga,Mn)As layers

(Ga,Mn)As is a dilute ferromagnetic semiconductor. The RKKY interaction governs the ferromagnetism in (Ga,Mn)As were distant magnetic impurities interact indirectly via spin-coupling to the carriers. Since manganese act as an acceptor in the GaAs crystal, (Ga,Mn)As shows a holes mediated ferromagnetism [56, 57, 59].
(Ga,Mn)As crystallizes in the ZB structure. In the ideal case Mn atoms substitute Ga atoms creating a tetrahedral bonding with four As atoms. At 600 °C, which represents the optimal growth temperature for MBE grown GaAs, Mn posses low solubility in GaAs (10^{18} cm^{-3}) leading to a Mn content $x_{Mn} = 10^{-5}$ [105]. At this concentration no ferromagnetism is observed. At 600 °C the increase of the Mn concentration results in the formation of MnAs clusters embedded in the GaAs matrix. This energetically favorable phase possesses a hexagonal crystal structure.
Homogeneous (Ga,Mn)As films can be grown by MBE at lower temperatures. In the temperature range of 210-260 °C Mn concentrations up to 10% can be achieved, while obtaining single crystal layers [106]. The Low Temperature (LT) growth of (Ga,Mn)As and generally of GaAs under non equilibrium conditions has as drawback the formation of point defects. The successful fabrication of single crystalline ferromagnetic (Ga,Mn)As layers depends not only on the growth temperature but also on the growth rate and group V to group III element ratio. Normally (Ga,Mn)As is grown under As rich conditions. The As partial pressure during growth influences the incorporation of point defects. These act as double donors and compensate the holes leading to an effective lower doping of the material [106]. The three major point defects are As antisites, Mn interstitials and MnAs clusters. A detailed discussion on the growth of (Ga,Mn)As layers can be found in [107, 108].

As antisites
An As antisite (As_{Ga}) defect is counted when As atom replaces a Ga atom in the crystal. At low temperatures the mobility of As molecules on the surface and the desorption rate of As atoms is reduced, leading to a non stoichiometric growth of the crystal. In this process the formation of As_{Ga} is the major effect [109, 110].
In (Ga,Mn)As As antisites are double donors and can therefore compensate two holes arising from two substitutional Mn atoms [111]. Since ferromagnetism in (Ga,Mn)As is mediated by the holes, the concentration of As_{Ga} defects strongly influences the magnetic and electronic properties of (Ga,Mn)As.
Other As based defects like As interstitials and As vacancies are negligible compared to As_{Ga} defects [110].
The concentration of As antisites is influenced mainly by the growth temperature and the As partial pressure.

Mn interstitials

In the (Ga,Mn)As crystal Mn atoms occupy not only the ideal position Ga site (Mn_{Ga}) but also unwanted interstitial positions (Mn_I) [112]. These point defects act as double donors like As_{Ga}, and each of them compensates two Mn_{Ga}, lowering the carrier concentration [113, 114]. The stable position in which double ionized Mn_I atoms can be positioned is in the center of a tetrahedron composed of four anionic Ga atoms (see figure 2.1).

Although allocating Mn atoms in substitutional positions is energetically favorable, Mn interstitials can be formed at the surface under non equilibrium conditions [114].

After a subsequent As deposition, however, the Mn interstitials near the surface are accounted to migrate to a Ga position, provided that the temperature is high enough to overcome the related energy barrier [114]. It is therefore expected, that Mn_I concentration decreases with an increasing growth temperature.

Mn interstitial defects have two negative effects on the magnetic properties of (Ga,Mn)As. They not only reduce the carrier concentration, which results in a reduced coupling between Mn spins and therefore in a reduced Curie temperature (T_c) of the material, but they are also antiferromagnetically coupled to the substitutional Mn atoms and lower therefore the saturation magnetization [115].

MnAs cluster

MnAs clusters form at the surface of the growing (Ga,Mn)As layer, in the case that the substrate temperature exceeds that of Mn segregation. The metallic clusters show a hexagonal symmetry and are randomly distributed in the crystal. Also post growth annealing at high temperatures (600-625 °C) can lead to a phase separation [116].

The presence of MnAs clusters in the (Ga,Mn)As layer has as a consequence the reduction of Mn_{Ga} and the creation of a carrier depletion zone around the particle due to the arising of a Schottky barrier [117]. To avoid the formation of MnAs clusters the growth temperature has to be maintained accordingly low.

Post growth annealing

As already known for GaAs a post growth annealing improves the crystal quality of the material. As a consequence the conductance and the Curie temperature increase [118].

Mn_I defects diffuse toward the surface due to the provided thermal energy [119]. Purging

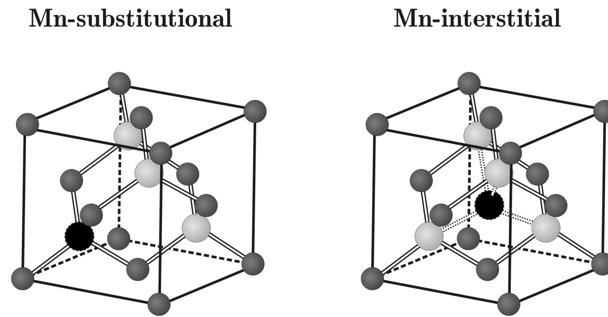

Figure 2.1: ***Substitutional and interstitial positions of Mn in ZB GaAs*** *- Left, the Mn atom substitutes a Ga atom. At this lattice position Mn acts as double acceptor and increases the hole concentration, and therefore the ferromagnetic order in the material. Right, the Mn atom sits at an interstitial position. A tetrahedral coordination with Ga atoms occurs. At this position Mn acts as double donor and compensates two holes. Mn interstitials also couples antiferromagnetically to substitutional Mn ions.*

the material from compensating defects allows the enhancement of the carrier concentration and hence the ferromagnetic interaction [118, 120, 121, 122, 123].
For being successful the post growth annealing has to be carried out in an ambient which provides the electrical passivation of the out diffused Mn_I atoms e.g. via oxidation, nitration or formation of MnAs, otherwise a charge accumulation at the surface will form and impede a further diffusion of Mn_I defects.

3 Molecular Beam Epitaxy

Molecular beam epitaxy is a technique which allows the epitaxial growth of high quality crystals with atomic precision in Ultra High Vacuum (UHV) conditions.
A wide range of materials can be grown by MBE techniques ranging from metal to semiconductors and insulators [124].
The fundamental process leading to crystal growth is the reaction of atoms or molecules rich in energy with the heated surface of the monocrystalline substrate. The deposited material adopt in this way the lattice arrangement of the substrate. UHV conditions lead to a mean free path of the molecules in the molecular beam larger than the chamber diameter and also prevent contamination of the growing material. The high purity material in the beam reaches the substrate surface unmodified and an atomic control of layer thickness, interface roughness, doping concentration and epitaxial heterostructures can be realized [108].

The knowledge of basic phenomena of the MBE growth are mandatory for the interpretation of the results of TEM investigations and for developing growth models. The comprehension of the effect of relevant parameters like As and Ga fluxes or growth temperature on NWs growth facilitate the interpretation of NWs morphological and structural properties.

3.1 Basic phenomena of MBE growth

A series of surface processes are involved in the MBE growth. The most important are:

- adsorption of the constituent atoms or molecules impinging on the substrate surface,
- surface migration and dissociation of the adsorbed molecules,
- incorporation of the constituent atoms into the crystal lattice of the substrate or the epilayer already grown,
- thermal desorption of the species not incorporated into the crystal lattice.

A schematic illustration of the most important processes is given in figure 3.1 [124].

The processes occurring on the substrate surface are characterized and controlled by kinetic parameters that describe them quantitatively.
The number of atoms impinging on the unit area of the surface per second is the *flux* of the arriving species and describes the arrival rate. The flux determines the supersaturation

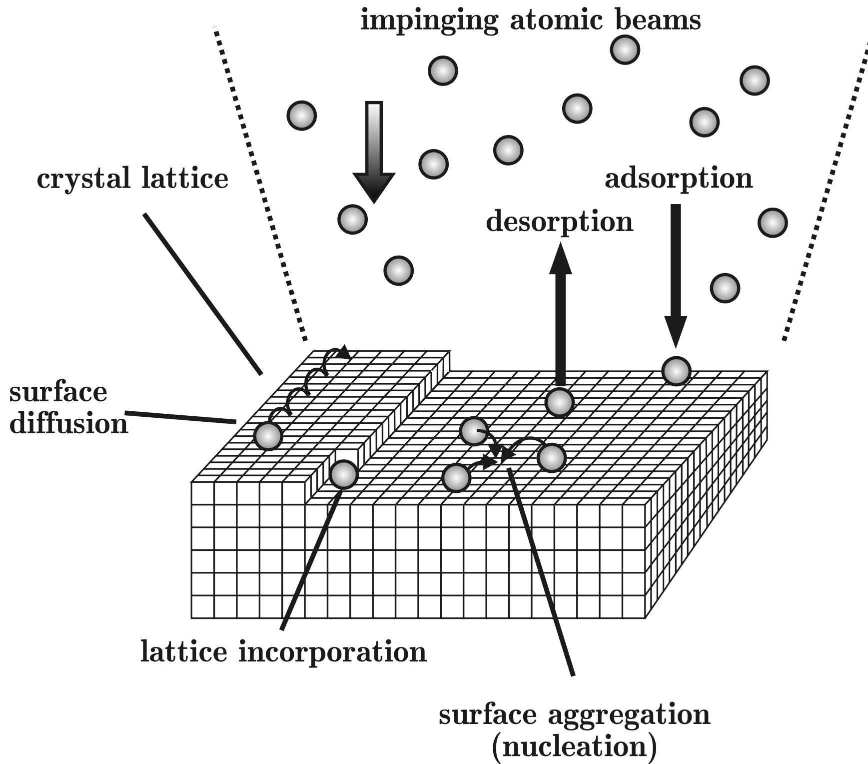

Figure 3.1: ***Surface processes*** *- MBE growth involves a series of surface processes. The balance of those processes determines the growth mode and the crystal quality. The most important processes are surface aggregation, which implies the nucleation of a new monolayer, surface diffusion, which is responsible for material transport, lattice incorporation of single adsorbed atoms, and absorption-desorption processes. These determines the supersaturation of the growing layer, which is the driving force of epitaxy. After [124].*

value, which is the driving force of epitaxy. The *accommodation coefficient* is a measure of the probability of the arriving atoms to reach thermal equilibrium with the substrate. The *sticking coefficient* is the ratio of number of atoms adhering to the substrate surface compared to the number of atoms arriving there. Physical adsorption, *physisorption*, and chemical adsorption, *chemisorption*, refers to two different types of adsorption. Physisorption occurs if the attractive forces are of van der Waals type, chemisorption when an electron transfer takes place between adsorbate and adsorbent.
Different sticking coefficients, one for the physisorption and one for the chemisorption, can be defined. The first does not show a dependency on the surface site arrangement, the second is dependent on the local environment and on the orientation and coverage of the substrate surface.
The condensation process is then a two step process. The physisorbed state, also called precursor state, implies a higher distance of the adsorbate from the substrate surface compared to the chemisorbed state, so that precursor molecules can diffuse over the surface with a constant rate until a free chemisorbed state is found. Condensation takes place. From the physisorbed state the molecule can also *desorb* back in the gas state.

A balance between these processes has to be set in order for MBE growth to occur. The substrate temperature, together with the fluxes of the growth species, are the parameters

that can be adjusted in order to realize the desired growth conditions. Below some limiting temperature T_L the deposited film will no longer be crystalline. MBE occurs near T_L when the surface migration exceeds the deposition rate. A high temperature limit T_H is defined by the balance between adsorption and desorption processes. For each material and each crystallographic orientation of the substrate different temperature ranges and molecular fluxes have to be chosen in order to obtain epitaxial growth.

The radial epitaxial growth on GaAs NWs sidewalls is accounted to be a 2D growth [125]. The parameters for 2D growth to occur are chosen in a first attempt accordingly to those used for 2D growth on a flat substrate with the same crystal orientation shown by the sidewalls. The low extension, about 40 nm, of the sidewalls and the presence of corners have as consequence a need of optimization of the growth parameters due to the presence of different surface energies. TEM analysis is used to optimize the growth.

3.2 Kossel´s model of crystallization

The Kossel model of crystallization is based on an atomistic approach considering two crystals, the substrate and the growing layer. Only first neighbor interactions are considered. Furthermore a simple cubic crystal for both crystals is assumed.
Different crystal sites gives rise to different surface processes because of their different chemical activity. A site may be created by a dangling bond, vacancy, step edge, etc. (see figure 3.2) [87].
The relevant atomic sites for MBE are *adatom*, *step*, *kink* and *cluster*.
Adatoms are adsorbed atoms making only a few bonds with the underlying atoms and can therefore migrate on the surface. They may come in contact with an uprising step that provides some additional bonds. The maximal possible number of neighbors is reached only at kink sites, therefore the adatoms can slide along the step edge by diffusion. At the kink site the adatom becomes incorporated into the substrate crystal. The kink site never disappears, it only slides along the step.
At every step edge a potential barrier called Ehrlich Schwoebel barrier is present. The effect

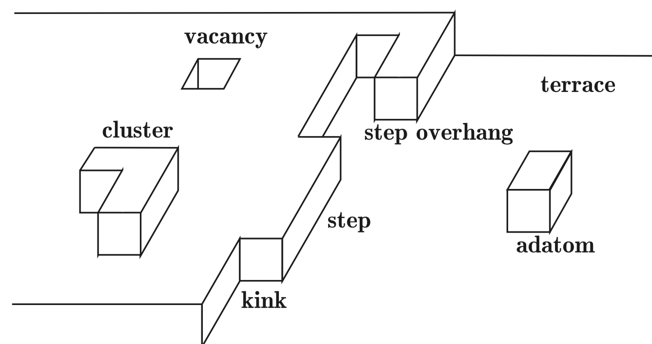

Figure 3.2: ***Atomic sites*** *- In the Kossel´s model of crystallization, depending on the interatomic interaction between substrate and incoming atoms, different atomic sites can be distinguished. Adatoms and kink sites are the two principal actors of a growing monolayer. The first diffuses toward a site with a higher number of neighbors, e.g. a step, and can be incorporated in the crystal only at kink sites. A cluster has a high probability to nucleate a new monolayer. Vacancies and step overhang are neglected in the discussion of the model. After [124].*

of this barrier is to reduce the probability for an adatom to move across the step. The effect on the morphology of the growing crystal are evident at low growth temperatures, where multilayer growth and stabilization of vicinal surfaces occurs [87].
On a flat surface without initial kink sites, a new monolayer can start to grow after a nucleation event. A cluster has to reach a critical size in order to initiate the monolayer growth [87, 124].

Experimental techniques

4 MBE chamber and sample growth

In this chapter the experimental techniques and equipment used for the realization of the investigated NWs will be shortly presented.
Molecular Beam Epitaxy (MBE) is the technique used for growing the investigated NWs. All the samples were realized by A. Rudolph at the chair of Prof. Bougeard.
In the following the different steps of NWs growth will be discussed. A detailed description of the MBE chamber can be found in [107, 108].

4.1 MBE chamber

The MBE chamber is a modified Gen-II-System (Veeco) suited for the utilization of 2 inch wafers. Its schematic representation is shown in figure. 4.1.
The residual gas pressure in the chamber is $< 10^{-11}\ mbar$. In order to prevent atmospheric gases to reach the growth chamber, the system is equipped with an entry lock, a transfer canal and a pre-chamber. The entry lock is used to insert and extract the samples mounted on an appropriate holder, the transfer canal gives the possibility to store up to 6 holders in an already high vacuum environment ensured by cryopumps. In the transfer canal a heating stage and a dedicated cryopump are mounted. Before entering the main chamber the substrates are exposed to a thermal treatment in order to eliminate possible contaminants present on the surface.
The chamber allows the deposition of Al, Ga, In and As. Si, Mn and C are also available and are used as doping elements. The material is provided in its atomic or molecular form by the employment of Knudsen effusion cells or by direct sublimation of pure material filaments.

The principal components of the MBE chamber are listed and described below.

Pumping system
UHV conditions are obtainable only if oil free pumps are used. The pre-vacuum is realized by sorption pumps which are cooled by liquid nitrogen. The transfer canal and the growth chamber use cryopumps to obtain a stable UHV.
Furthermore the growth chamber is equipped with large surface shrouds that are cooled down to liquid nitrogen temperature. Those are positioned near the effusion cells shutters and near the manipulator, in order to assure the best vacuum at the substrate surface and

to efficiently pump atoms and molecules originating from the effusion cells. Also a titanium sublimation pump is installed.

Effusion cells

Knudson-cells are used for the effusion of group-III elements. Al, Ga, and In evaporate from a Pyrolytic Boron Nitride (PBN) crucible heated during growth at the required temperature by a tungsten filament.

Doping cells

For the doping elements Si, C and Mn different effusion cells are adopted. For Mn a normal Knudson cell is used and, since its position on the chamber is downward looking, a tantalum grid prevent the loss of material from the crucible.

Si and C sublimate directly from a filament. The high temperature needed for sublimation to occur could damage the PBN crucible. A high current through the filament heats the material and so, since high thermal capacities are avoided, a fast regulation of the molecular flux of the dopant can be achieved.

Arsenic source

A valved cracker cell is used for the effusion of As. Two independent heating stages control the temperature of the As crucible and of the cracking zone. A needle valve regulates the As_4 molecular flux. Depending on the temperature of the cracking zone As_4 can be converted into As_2. Depending on the growth conditions using As_2 molecules for the growth can improve the growth kinetic [107].

Temperature determination

The substrate surface temperature is measured by a pyrometer which detect the intensity of the radiation emitted by the GaAs surface. A thin liquid metal layer between substrate and holder assures a good thermal coupling.

Manipulator

The manipulator has two rotation axes, so that during growth the substrate can be rotated

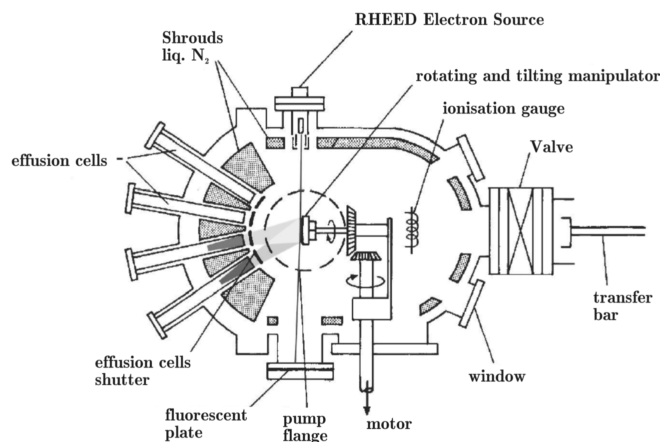

Figure 4.1: ***Cross section of the utilized MBE chamber*** - *After [108].*

and tilted. The heating stage provides a homogeneous temperature on the substrate surface. An ionization gauge behind the manipulator is used to determine the pressure in the chamber. It is also utilized to measure the partial pressure of the As as well as the Ga and Mn molecular beam.

Reflection High Energy Electron Diffraction (RHEED)
The RHEED equipment is composed of a high energy electron source and a fluorescent plate. This surface sensitive diagnostic method provides information on the crystal structure of the substrate surface and its reconstruction, on the surface roughness, and also on the growth modi. High energy electrons hit the surface at a grazing angle so that only the first few monolayers (MLs) contribute to the diffraction pattern. The electron source and a fluorescent plate have to be mounted in mirrored positions referred to the center of the chamber. RHEED is also used for the calibration of the growth rate. Due to the high sensitivity to surface morphology and topology, the intensity of the spots of the diffraction pattern oscillates with a period equal to the time needed for the formation of a new ML. This oscillation is used to determine the flux of Ga. As long as an As-excess is present in the MBE chamber the period of the oscillations is limited by the Ga flux.

4.2 NWs growth

In the following the applied NW growth procedure will be described.
General aspects will be presented, considered that the investigated NWs differ only in the values of the growth parameters and not in their growth procedure. This consists of four steps:

Au deposition
The Au films are deposited on (111)B GaAs epi-ready substrates. The deposition occurs for all the samples with the exception of the first one in a metal MBE chamber equipped with Knudson effusion cells at the chair of Prof. Back.
The first Au/GaAs wafers were provided by Dr. T. Wojtowicz of the Polish Solid State Physics Laboratory in Warsaw. Also in this case a metal MBE chamber was used for the deposition of Au.
The deposited thickness can vary between a fraction of a nanometer and 10 nm and is monitored during growth by a quartz crystal operated microbalance.

Oxide desorption and droplet formation
The Au film is grown on the native GaAs oxide, due to an inevitable air exposition. The substrates are heated to 580-610 °C for a time varying between 30 and 60 min under As_4 flux. The successful oxide desorption is monitored by RHEED. When oxide is desorbed the diffraction pattern of the GaAs substrate becomes visible. The As_4 flux prevents the dissolution of the GaAs substrate.
At this point also Au-Ga droplets are formed.

NW growth
The growth temperature is lower than the oxide desorption temperature and its standard value is 540 °C. The As_4 and Ga fluxes are regulated in order to achieve the desired ratio. The opening of the Ga shutter determines the growth start. The typical growth duration is about 2.5 h. The NW growth is monitored by RHEED.

Termination

The closure of the Ga shutter initiates the growth termination. At the same time the heating stage is turned off. After 3 to 5 minutes when the substrate has cooled down to 400 °C, also the As shutter is closed. The As shutter is closed after the temperature is below 400°C for preventing a substrate dissolution.

5 Transmission Electron Microscopy

Transmission Electron Microscopy (TEM) makes use of the wave nature of high energy electrons for imaging material specific information of a thin specimen. The electron specimen interaction, described by elastic and inelastic scattering, is the origin of the information carried by the transmitted electrons. Elastic scattering at the Coulomb potential of a nucleus is a highly localized process that contributes to the image contrast. On inelastic scattering are based the analytical functions of a TEM due to the related material specific energy losses.
TEM represents the primary tool for the microstructural characterization of materials. The achievable resolution is limited by the lens aberrations and is in the order of $0.1 - 0.3\,nm$ for uncorrected lenses.
A TEM can combine high spatial resolution with analytical techniques and scanning capabilities. These resources gives access to detailed information of the investigated material.
In the case of semiconductor heterostructured nanostructures, it represents a unique way to have access simultaneously to information on the crystal structure and on the composition.

5.1 The microscope

The used microscope is a FEI Tecnai F30. The principal components of the microscope are listed and described below.

Field Emission Gun (FEG)
The electron source of the FEI Tecnai F30 is a thermally enhanced field emitter (Schottky emitter).
The emitter consists of a tungsten single crystal in <100> orientation covered with a thin layer of zirconia (zirconium oxide). The ZrO layer serves to lower the work function of tungsten from $\phi_W = 4.5\,eV$ to $2.7\,eV$.
The main component of the gun unit are the field emitter, an extraction anode and an electrostatic gun lens.
The electrostatic gun lens focuses the emitted electrons into a cross over of about 15 nm in diameter. The electrons are then accelerated to the desired operating voltage in the range 80-300 kV.

The brightness $\left(A/\left(cm^2 \cdot srad\right)\right)$ and the energy spread (eV) of the electron beam are the two main factors characterizing the performance of an electron gun. They are of interest in all work that needs high coherence: the energy spread for the temporal coherence in high

resolution imaging, holography and for high energy resolution energy loss spectroscopy, the brightness for the spatial coherence in high resolution imaging, holography and for small probes with high currents. The brightness is defined as the current density per solid angle. A high value of the brightness allows the utilization of a small aperture when forming the beam. The plane wave character of the beam is enhanced and so the spatial coherence.
Typical values for the brightness and for the energy spread for a thermionic source and a Schottky emitter are respectively 10^6 vs 10^8 $A/\left(cm^2 \cdot srad\right)$, and 0.5-2.0 vs 0.3-1.0 eV.

Illumination system
The illumination system controls the intensity and the angular convergence of the electron beam on the specimen. The electron beam is formed by a two stage condenser lens system which permits variation of the illumination aperture and of the illuminated area of the specimen.
The lenses of an electron microscope are electromagnetic lenses. These are affected by aberrations which arise from instabilities or lack of symmetry in the generated magnetic field due to e.g. thermal fluctuations and spurious charged particles.

Objective lens
The objective lens has the purpose of a first magnification of the specimen.
The TWIN lens design of the objective lens refers to a symmetrical condenser objective lens with a minicondenser lens inserted into the upper pole piece. This three lens system allows either a parallel illumination of the specimen (microprobe mode) or the focusing of the beam in a sub nanometer sized probe (nanoprobe mode). The specimen is placed in the back focal plane of the condenser lens, which corresponds to the front focal plane of the objective lens.

Imaging lenses and viewing screen
After the interaction with the specimen, the electron intensity distribution is magnified with a three stage lens system and imaged onto a fluorescent screen. Both the real and conjugate plane of the objective lens can be imaged by varying the focal length of the lens system, providing either a magnified image of the specimen or of its diffraction pattern (DP).
The image can also be recorded digitally with a Gatan 1k Slow Scan Charge Coupled Device (CCD) camera mounted below the viewing screen. Alternatively the 2k CCD of the Gatan Imaging Filter (GIF) can be used for the image digitalization.

Analytical TEM
The used microscope has analytical capabilities due to the presence of an X-ray spectrometer for Energy Dispersive Spectroscopy (EDS) and of a spectrometer for Electron Energy Loss Spectrometry (EELS).
The first is mounted laterally above the specimen and collects and analyzes the back emitted X-rays generated by the electron matter interaction. The second is a post column spectrometer and collects and analyzes the inelastic transmitted electrons.
These two techniques are complementary because of a different range of elements which can be detected efficiently. EDS is better suited for heavier elements, EELS for lighter ones.
Both instruments reveal the composition of the investigated specimens. More details are given in subsection 5.4.

Scanning Transmission Electron Microscopy (STEM)
A scanning unit allows the scanning of the electron probe over the sample. The probe is formed in the nanoprobe mode by the objective lens and deflected by deflection coils. A

Bright Field (BF) detector collects the intensity of the central transmitted beam and thus generates an image of the specimen point by point.
The transmission $T = I/I_0$ recorded in absence of a specimen, being I_0 the intensity of the incident beam and I the intensity of the detected beam, is not unitary. It depends on the ratio of the probe incident angle and of the detector collection angle. For maximizing the transmission, and therefore the signal to noise ratio, a comparable value of those angles has to be chosen.
When the specimen is inserted in the beam path, the detected intensity diminishes due to electrons elastically scattered at an angle larger than the collection angle. Scanning over regions of the specimen with different composition or thickness produces a contrast in the image, because of different scattering angles and absorption coefficients.
STEM combined with analytic instruments allows the generation of element maps or element specific line scans suited for the determination of element distribution in the specimen. Also the elemental composition at interfaces or of embedded nanostructures can be obtained if a stationary electron probe is selected.
Due to the strong interaction of the electrons with atoms by elastic and inelastic scattering the specimen must be very thin, typically in the range $10 - 100\,nm$, in order to allow TEM investigations.

5.2 Sample preparation

Standard preparation techniques were applied to NW samples in order to verify their capability to produce specimens suitable for TEM investigations.
The adopted crystal structure, the density of SFs and the morphology of NWs in the axial direction can be investigated realizing specimens that offers a side view of the NWs. The shape of NWs and in core/shell NWs the properties of the shell can be observed in cross section specimens.
The achievement of the requirements on the thickness of the material is limited by the used technique, and in some cases by the physical dimensions of the NWs itself.

5.2.1 NW transfer on carbon film

The direct mechanical transfer of NWs on a copper grid coated with a holey amorphous carbon film is the preparation procedure which allows the lowest modification grade of the NWs. NW dimensions determine the effective thickness seen by the electrons.
The preparation technique consists in placing the grid on the substrate with the carbon film in contact with the wires. Since the wires grow vertically, a shear force is needed in order to break and transfer them to the grid. This is done by carefully press the rounded head of tweezers on the grid. The NWs then adhere to the carbon foil and can be directly inserted in a TEM holder for the investigations.
A drawback of this technique is the risk of obtaining a high density of NWs on the carbon film which impedes any useful investigation because of an overlapping of the NWs.
An alternative is represented by the use of a razor blade to remove the NWs from the substrate and then dispersing them in ethanol. Immersing the grid in the ethanol distributes the NWs present at the liquid surface homogeneously on the carbon film. Once the grid is extracted from the ethanol and the latter is evaporated the grid is ready for transmission electron microscopy.
In figure 5.1 the result of a NW transfer on a carbon film is shown. The left micrograph

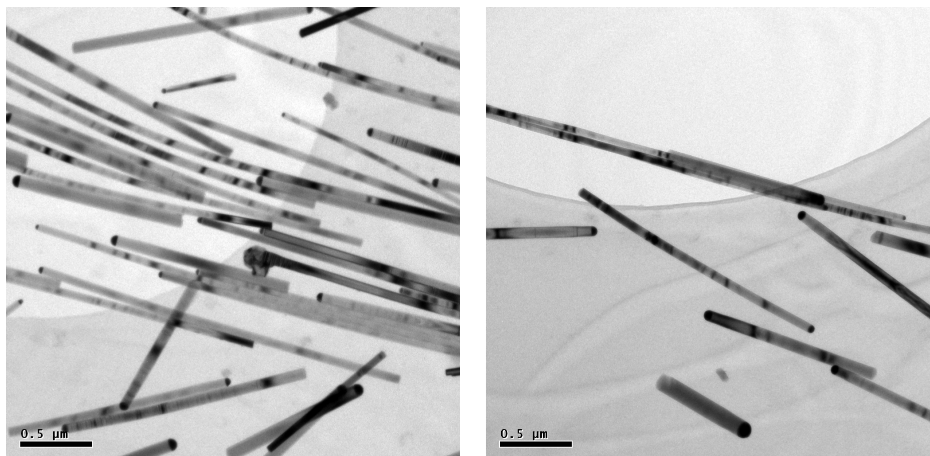

Figure 5.1: ***NWs transferred on a holey carbon film*** *- Left,region of a carbon film with a high density of transferred NWs. Right, region of a carbon film with a low density of transferred NWs. In both micrographs a hole in the carbon foil is recognizable. NWs hanging over a hole are more suited for HRTEM investigations due to the absence of an amorphous layer superimposed to the crystal.*

illustrates the case in which a NW cluster is formed. Only an overview of the aspect of the NWs can be obtained. The micrograph on the right represents a case of low NW density. In this case orienting single NWs along a zone axis allows the investigation of its crystal structure.
The lack of control over the lying orientation of the NWs and the need to select a proper crystallographic direction, makes TEM investigations of the crystal structure time consuming, so that a high statistic could not be achieved.

5.2.2 Standard TEM cross section preparation

In order to investigate the NW cross section, a modified standard TEM cross section preparation was implemented. The method was proposed by Spirkoska et al. [126].
NWs have to be removed mechanically from the growth substrate and have to be transferred on a Si substrate by rubbing the two pieces of material against each other. The intention is to obtain a Si surface covered by a high density of parallel oriented NWs.
Afterward a SiO_2 layer is deposited on top of the NWs by Plasma Enhanced Chemical Vapor Deposition (PECVD). The thickness of the deposited layer is at least 200 nm in order to completely cover the lying NWs. In order to obtain a cross section the NWs+SiO_2 layer is covered by a second Si piece forming a sandwich. Keeping track of the orientation of the NWs, traditional thin film cross section preparation is used with a final step comprising a focused ion beam etching technique.
A detailed description of the standard cross section preparation method can be found in [127].
The mechanical transfer of the NWs over the Si substrate was performed by E. Reiger at the chair Bougeard and the SiO_2 deposition by C. Linz at the chair Weiss.
In figure 5.2 a TEM bright field micrograph of the prepared cross section is shown. The dark circles or hexagons represent the projected cross section of the NWs. The deposited SiO_2 is recognizable as a discontinuous layer on the top of the NWs. The Si layer is visible at the bottom and the glue used for the sandwich at the top right corner of the image.

The SiO_2 layer does not form a flat surface, so that the minimum achievable distance between the two Si pieces is in the order of few μm, which is an order of magnitude higher than the optimum value. As a consequence of these aspects, the ion beam thins the specimens in an irregular way, forming thickness steps which arises from shadowing effects, as can be seen in figure 5.2.
A further drawback of this technique is the potential altering effect of the ion bombardment on the chemical and structural composition of (Ga,Mn)As. A non negligible heating process occurs during ion milling, so that local modifications of the material composition cannot be excluded [128].

5.2.3 Ultramicrotomy

A microtome is a sectioning instrument used for cutting extremely thin slices of material. The model used for the preparation of the NWs is an ULTRACUT E developed by the company Reichert-Jung Optische Werke AG. The diploma student J. Bill developed during his thesis the single steps of the preparation procedure applying them to the NWs. Details of the procedure can be found in [129]. Here the basic concepts of ultramicrotomy will be presented.

Obtaining a slice thickness in the range $50 - 100\,nm$ from a specimen mounted on a moving arm is possible using its precise linear mechanical movement. Very fine control over the cut dynamics can be provided with this method. As depicted schematically in figure 5.3 the

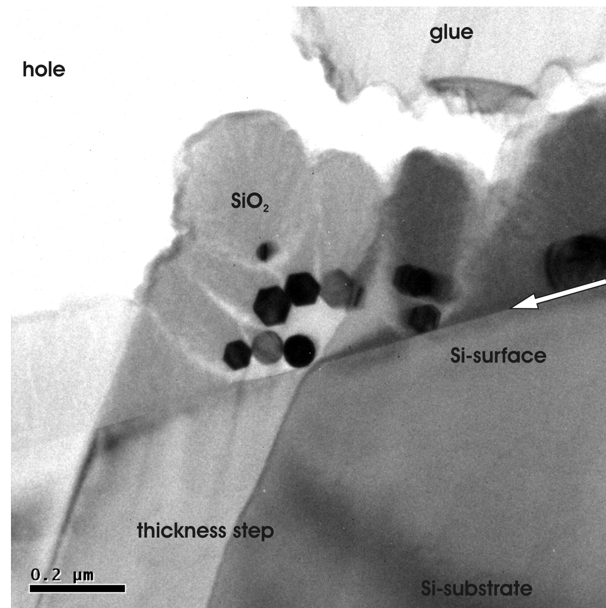

Figure 5.2: ***NWs cross section, standard TEM preparation*** - *Bright field micrograph showing from the bottom to the top the Si substrate, NWs covered with approx. 200 nm SiO_2 and glue used for the sandwich. The preparation is effective, in fact all NWs are parallel oriented showing their cross section. The irregular SiO_2 profile induces a relatively wide gap between the two Si pieces of the sandwich. These characteristics induce an irregular etching of the ion beams during milling. The thickness of the specimen varies abruptly due to shadow effects. This can be deduced from the contrast change between adjacent regions in the specimen.*

specimen is mounted on the arm which moves cyclically with a constant progression in direction of a diamond knife. The arm alternates horizontal and vertical movements in order to position the specimen above the knife and then cutting a slice. The tunable constant progression of the arm determines the thickness of the slice. The slice floats off onto an inert medium, usually distilled water, and can then be collected on a TEM grid.
In order to stabilize the NWs and to give to the sample a geometry suitable for being mounted on the arm, the NWs are first embedded in resin. The EMBed-812 Embedding Kit was used. The kit contains the resin, two anhydrides as curing agents and an accelerator. The hardness of the mixture and therefore the mechanical properties of the thin slices can be controlled by the percentage of anhydrides used and by their relative weight.
The obtained embedding medium is used to fill a mold containing a piece of NW substrate. The medium is cured in an oven at 60 °C for 24 hours. The formed blocks can be trimmed and sectioned, in order to obtain a small tip surface in the vicinity of the embedded sample. Depending on the relative orientation of the tip surface to the NW substrate, a cross section or a side view of the NWs can be obtained.
In figure 5.4 a bright field micrograph of NW cross sections is shown.
Since the slice cuts are a few degrees misaligned in respect to the NW substrate, different regions of the slice contain segments of NWs arising from different NW heights.
In this way statistic values concerning e.g. the density of NWs or the diameter distribution in dependency to the NW height can be easily obtained as shown in figure 5.4.
Furthermore the relative orientation and position of the NWs is maintained. This allows a direct comparison of facet orientations and also the analysis of local NW diameter distributions.
The relatively low temperature used for curing the embedding medium, compared to typical annealing temperatures of 180 °C, makes this preparation method suitable for the determination of the chemical composition of the (Ga,Mn)As shell.

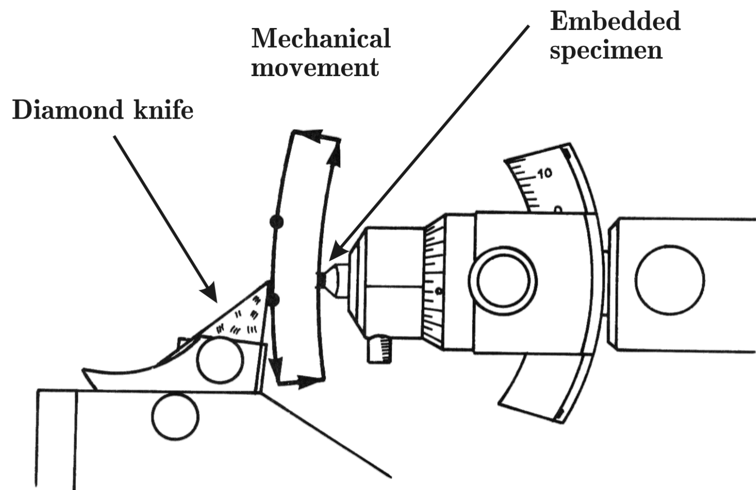

Figure 5.3: ***Ultramicrotomy*** *- Schematic representation of the cut dynamic of the microtome arm. The sample is embedded in epoxy and mounted on the arm. The latter moves cyclically on the diamond knife and produces thin slices of the compound. The thickness of the slice is determined by the tunable mechanical progression of the arm. Draft after [130].*

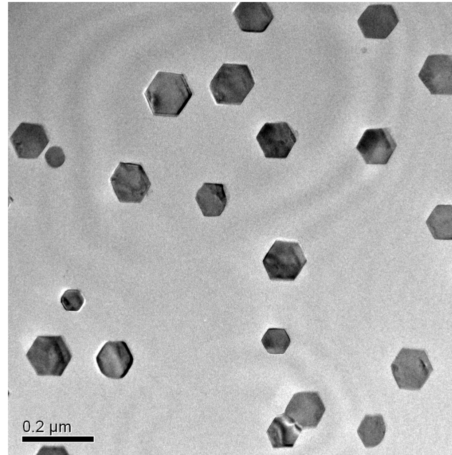

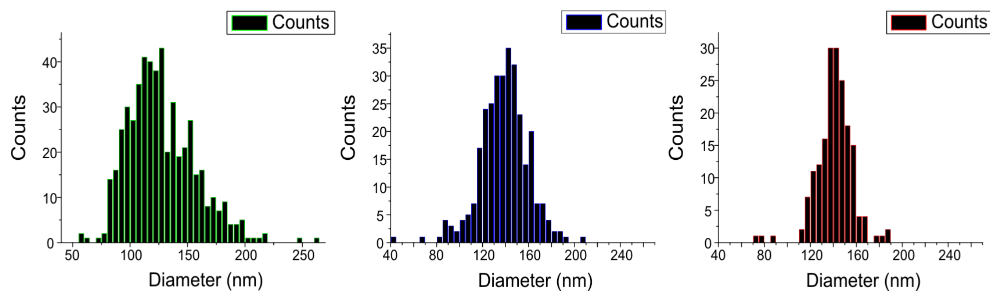

Figure 5.4: ***NW cut** - Top, bright field micrograph of a NW cut. In an ultramicrotome cut both the original NW distribution and their relative orientation is conserved. Compared to side view NWs transferred to a TEM grid, crystal structure analysis can be performed faster because the cross sections are oriented along the same crystallographic axis. Bottom, Statistic showing the distribution of the NW diameter in three different positions on the slice. Since the slice is misaligned in respect to the NW substrate, the three different positions correspond from left to right to the base, the middle part and to the top of the NWs. A tapering effect can be recognized.*

5.3 Conventional TEM techniques

The imaging theory in a TEM relies on a wave optical approach. The high temporal and spatial coherence of the electron beam allows its representation as an incident planar wave. As consequence of the interaction with a thin specimen, elastic scattering processes occur. The electron wave leaving the specimen, the object wave, is a superposition of an unscattered planar wave and scattered spherical waves. The outgoing wave is modulated in amplitude and phase with respect to the incident wave.

5.3.1 High Resolution TEM imaging

In a TEM the objective and several projector lenses create from the object wave a highly magnified image wave. The symmetric aberrations of the imaging system are incorporated in the image formation as a convolution of the object wave with the Point Spread Function (PSF) which is characteristic to the microscope. The PSF represents the error disc that corresponds to the image of a point like object. It originates from a finite dimension of the objective aperture, from lens aberrations and from defocus.

The contrast of a High Resolution TEM (HRTEM) image is a phase contrast. The complex interaction process between the incident planar wave and the specimen, described by the dynamical scattering theory, produces a phase shift of $\pi/2$ between the unscattered and the elastically scattered wave (see figure 5.5a)).
If ψ_i is the amplitude of the unscattered wave in the final image $\left(I_0 = \psi_i \psi_i^* = |\psi_i|^2\right)$ and ψ_{sc} that of the scattered wave, the resulting amplitude can be written as $\psi_i + i\psi_{sc}$ if the Contrast Transfer Function (CTF) is neglected.
The CTF relates the amplitude and phase of the image wave with the intensity of the beam on the viewing screen. The CTF is defined in the reciprocal space and is a function of the spatial frequency q, the defocus $\triangle z$ and of the spherical aberration C_s.
As shown in figure 5.5 a) for $\psi_{sc} \ll \psi_i$ the intensity $I = |\psi_i + i\psi_{sc}|^2$ does not differ significantly from $I_0 = |\psi_i|^2$, so that the object is invisible for a pure phase object. Our specimen can be considered to be phase objects if prepared by the standard cross section techniques because of their thickness below ca. 50 nm. The specimen thickness has to be lower than the mean free path of the accelerated electrons in the material. NWs transferred on a carbon film can be considered to be phase objects only at their lateral edges. In all other cases also an amplitude modulation of the outgoing object wave has to be considered.
When introducing an additional phase shift of $\pi/2$ a positive phase contrast can be achieved since $I = |\psi_i - \psi_{sc}|^2 < I_0$ (see figure 5.5 b)). A total phase shift of $-\pi/2$ is called negative phase contrast (see figure 5.5c)). The additional phase shift is obtained modifying the CTF. This description of the emerging contrast is valid for thin specimens for which absorption can be neglected and the object wave has only a phase component described by its linear approximation.

Due to the dependency of the CTF from the spatial frequency q, and therefore from the scattering angle, a constant phase shift cannot be realized simultaneously for all spatial frequencies. Since C_s depends on the characteristics of the objective lens the microscopist can control the range of spatial frequencies which experience an approximately constant phase shift only by changing the defocus $\triangle z$. The higher the upper boundary of the spatial

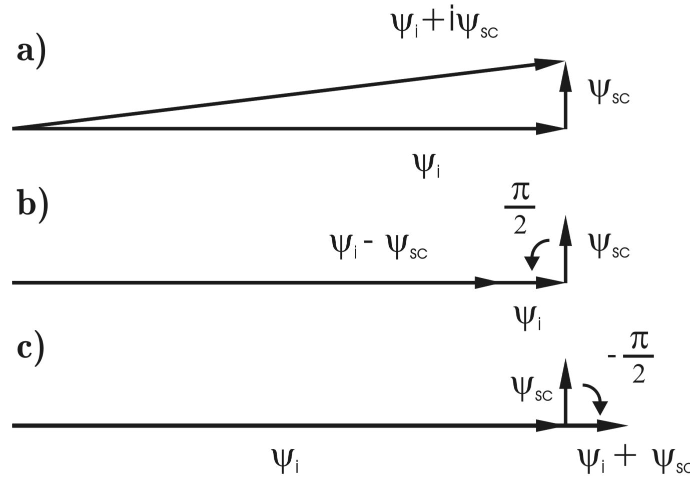

Figure 5.5: ***Principle of the phase contrast*** *- a) the $\frac{\pi}{2}$ phase difference between scattered and unscattered wave results in a negligible contrast, the amplitude difference of the image wave with or without inserted specimen is negligible, b) a further phase shift of $\frac{\pi}{2}$ realizes a positive contrast c) a $-\frac{\pi}{2}$ phase shift a negative phase contrast. Image after [131].*

frequency range is set the lower the periodic spacing in the specimen that can be resolved. The optimum value for $\triangle z$ is called Scherzer defocus and represents the maximum range of spatial frequencies transferred correctly.
Due to the oscillating character of the CTF at some spatial frequencies, corresponding to its zero crossing points, no specimen information reaches the image. Furthermore other higher frequencies intervals are imaged with a negative phase contrast.
Therefore when changing the defocus a same spatial frequency is imaged subsequently with a varying phase contrast. The contrast oscillates between positive and negative.
For this reasons HRTEM images of unknown specimens have to be compared with a simulated phase image of the supposed structure.

With an aberration constant C_s of $2\,mm$ the FEI Tecnai F30 has a point resolution at Scherzer defocus of $0.19\,nm$.

The diffractogram, a Fast Fourier Transform (FFT) of the intensity distribution of a phase image, allows the determination of the periodicity present in the micrograph. It shows the modulus of the CTF in the reciprocal space if every periodic spacing is contained in the specimen (amorphous specimen). When a crystal structure is imaged, the FFT shows intensity maxima at spatial frequencies arising from the periodic spacing realized by the two dimensional unit cell. The determination of the crystal structure can therefore be performed by analyzing the FFT of a HRTEM image (see figure 5.6). for this purpose the starting HRTEM image has to reproduce the crystal periodicity correctly. If the CTF has a zero at the frequency that should be imaged the FFT analysis will develop erroneous results. In our case the analyzed crystal structures are well known so that the correctness of the represented periodicity is ensured.
The commercial software used for acquiring HRTEM images and calculating FFTs is the Gatan Digital Microgaph software.

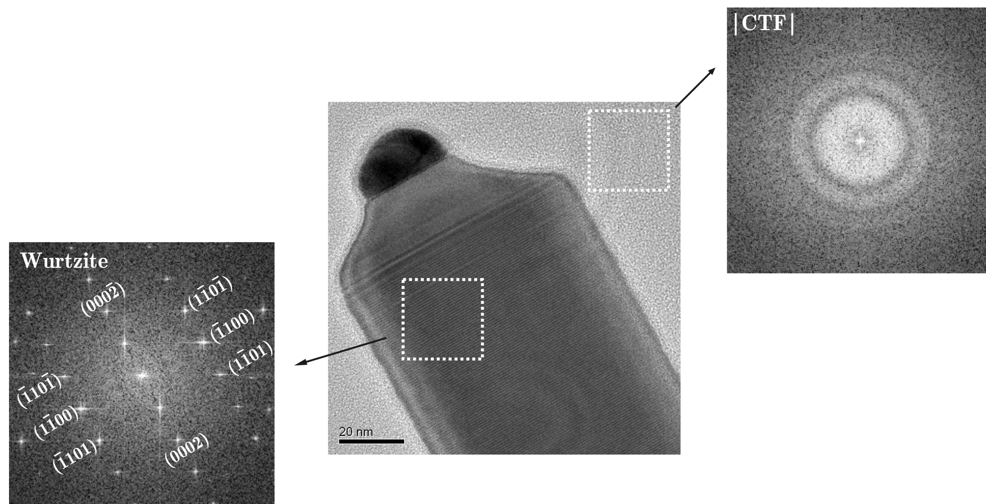

Figure 5.6: ***FFT of a HRTEM image*** - *Center, Side view HRTEM image of a NW on a carbon foil. Right, FFT of an amorphous region showing the modulus of the CTF. The oscillating character of the CTF is visible. Left, FFT of the periodic spacing representing the two dimensional lattice of the WZ structure oriented in a* <*11$\bar{2}$0*> *direction.*

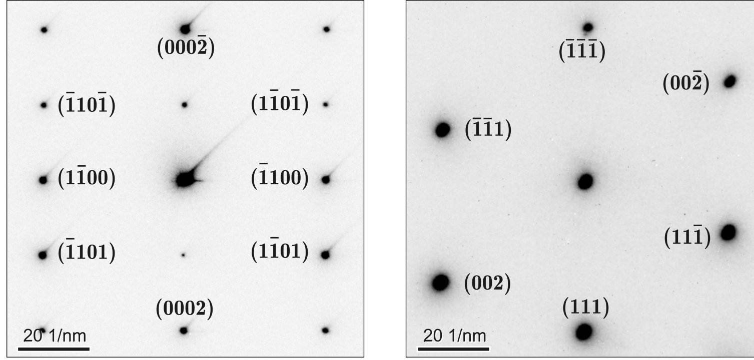

Figure 5.7: ***Diffraction patterns of the WZ and ZB structure** - Left) DP of the WZ crystal structure along the* $[11\bar{2}0]$ *zone axis Right) DP of the ZB crystal structure along the* $[1\bar{1}0]$ *zone axis.*

5.3.2 Diffraction patterns

When a plane electron wave interacts with the specimen the Diffraction Pattern (DP) is observed at infinite distance. In a TEM the objective lens focuses the scattered parallel beams in its back focal plane and the diffraction pattern of the specimen can be imaged on the viewing screen.

In the case of a crystalline specimen the position of the intensity maxima in the DP are determined by the intersection of the Ewald sphere with the Zero Order Laue Zone (ZOLZ) of the reciprocal lattice.

DPs are employed in this work for the identification of the crystal structure of NWs. Since it is known that the only two possible structures assumed by the NWs are wurtzite or zinc blende, NWs were oriented in a crystallographic direction suited for the distinction of the two arising DPs. This direction is the $<1\bar{1}0>$ and accordingly $<11\bar{2}0>$ for a cubic or hexagonal lattice. The diffraction patterns of WZ and ZB are shown in figure 5.7. In a NW showing both crystal structures, the $<1\bar{1}0>$ and $<11\bar{2}0>$ directions are crystallographic equivalent, so that a reorientation of the NW is not necessary if the crystal structure changes. Only side view specimen gives simple access to the mentioned orientations.

In figure 5.8 a top view of the atomic arrangement in the $(\bar{1}\bar{1}\bar{1})$ and $(000\bar{1})$ planes and the corresponding kinematically calculated DPs are shown. The different arrangement of the atoms gives rise to different structure factors. The latter determine at which scattering angle constructive interference of the scattered waves occurs, and also the intensity distribution between the different spots.

The lattice constants however is the same for the $(\bar{1}\bar{1}\bar{1})$ and $(000\bar{1})$ planes. This implies that when the two DPs are superimposed, those are not distinguishable because the position of the diffracted spots by the ZB crystal is identical with the position of some spots diffracted by the WZ crystal.

The determination of the crystal structure from a NW cross section is theoretically possible but the presence of SFs makes the two DPs indistinguishable.

As shown in figure 5.8 c) neither the arrangement of the ZB DP nor the intensity distribution of the WZ DP can be recognized. A SF in a given crystal structure represents a nanometer sized segment of the other crystal structure resulting in a superposition of the two DPs due to multiple diffraction.

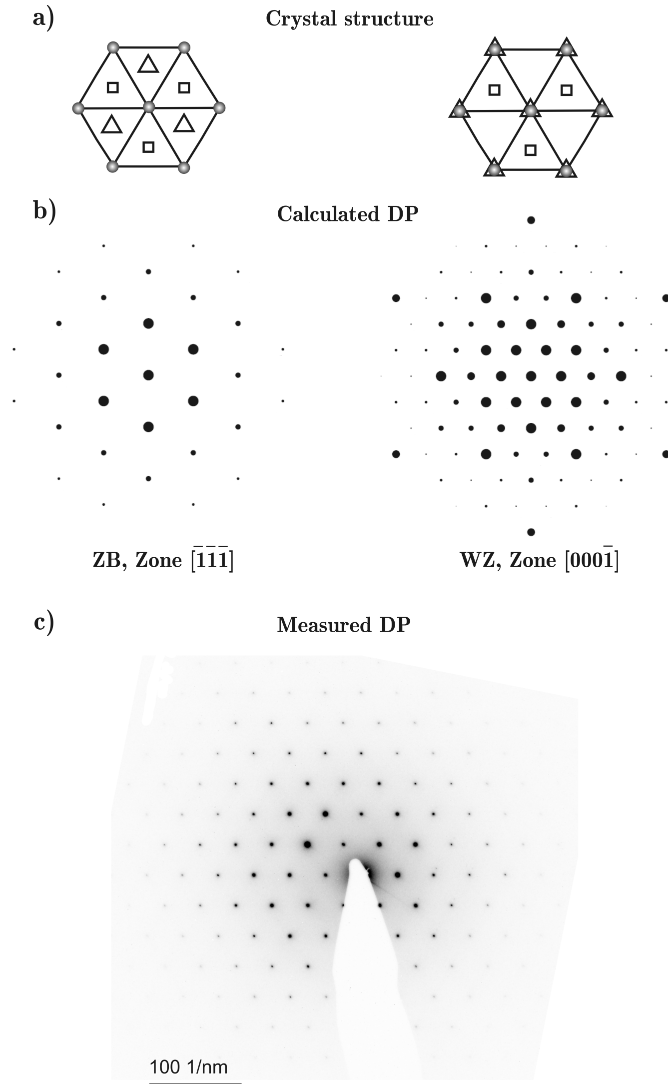

Figure 5.8: [$\bar{1}\bar{1}\bar{1}$] ***and*** [000$\bar{1}$] ***zone axis DPs*** *- a) arrangement of the atomic layers in the* [$\bar{1}\bar{1}\bar{1}$] *and* [000$\bar{1}$] *projection. For ZB on the left each atomic layer, respectively triangles, squares and dots, occupies a different position accordingly to the ABCABC... stacking sequence. For WZ on the right the first, triangles, and the last, dots, atomic layer occupies the same position accordingly to the stacking sequence ABAB.... The lattice constants in the ZB*($\bar{1}\bar{1}\bar{1}$) *and WZ*(000$\bar{1}$)*are identical. b) kinematically calculated DPs for the ZB structure on the left and for the WZ structure on the right. Different structure factors result in different arising reflections and also different distribution of the intensity between the reflections. Calculations performed using a freeware software on the web. c) the acquired DP of a cross section NW does not allow the identification of the crystal structure due to the presence of SFs.*

5.3.3 Determination of the NWs crystal structure

The procedure for the identification of the crystal structure of a NW in the TEM consists in identifying the DP and looking at its changes when moving the beam along the NW axis. Keeping the NW orientation constant, three different DPs are commonly observed (see fig-

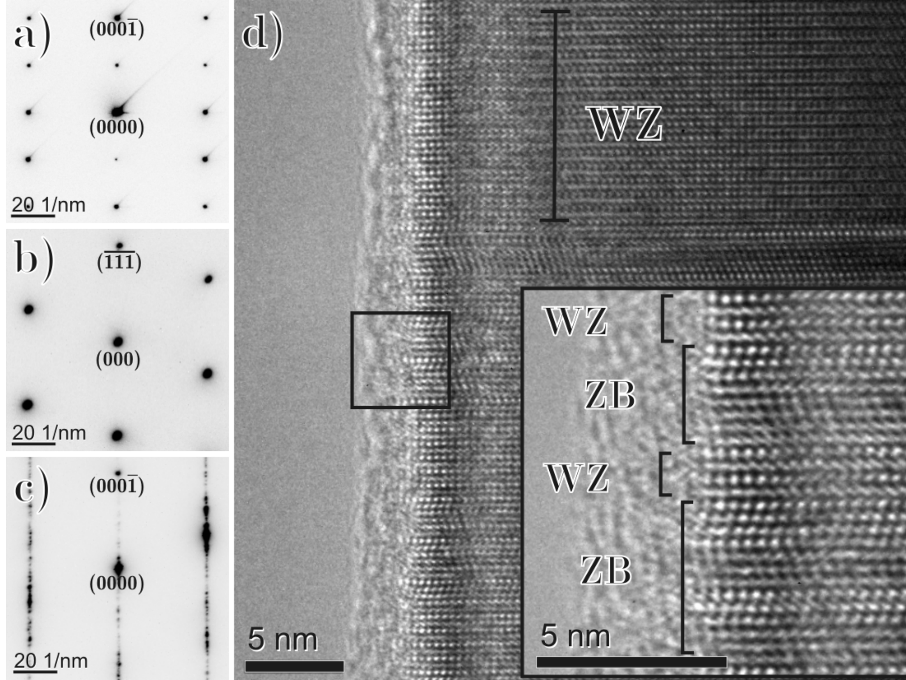

Figure 5.9: ***Diffraction patterns and HRTEM micrograph of a NW region with a mixed crystal structure*** *- a): WZ* $(11\bar{2}0)$ *zone axis, b) ZB* $(1\bar{1}0)$ *zone axis. These two directions are equivalent orientations of the two crystals. c) diffraction pattern of a NW region with a high density of stacking faults, d) HRTEM micrograph of a NW regions with WZ crystal structure and ZB segments embedded in the WZ matrix. If the investigated NW has a low density of stacking faults the WZ and the ZB DP can be distinguished as in a) and b). Otherwise HRTEM images should be analyzed in order to clarify if ZB segments are present in the structure.*

ure 5.9, a), b), c)) .
The $(11\bar{2}0)$ WZ and $(1\bar{1}0)$ ZB zone axis, which are equivalent crystal directions, are distinguishable from the different patterns of the diffracted spots. NWs with a high density of stacking faults in contrast need an additional analysis. As showed in figure 5.9 c) the DP of a faulty region does not allow the determination of the presence of the ZB crystal because of the absence of a recognizable pattern. In such cases HRTEM pictures of the NWs were analyzed. Figure 5.9 d) shows an example of ZB segments embedded in a WZ matrix.
A stacking sequences ABCABC... of at least $2\,nm$ is considered a ZB segment.
Since in Au-assisted MBE grown NWs the common observed crystal structure is WZ, the analysis has the main purpose to verify the presence of ZB segments in the structure. A statistic description of the proportion between WZ and ZB segments in single NWs is not the aim of this work. This kind of analysis is meaningful if a detailed thermodynamical model is available for the data interpretation. Furthermore the presence of SF segments, in some cases μm long, suggest that droplet state instabilities plays a fundamental role in the determination of the quality of the crystal structure (see chapter 6).

5.4 Analytical techniques

An inelastic collision of an electron with an atom conserves the total energy and the momentum converting a part of the kinetic energy in an electron excitation. Three main

mechanisms involved in the electron energy loss can be distinguished:

- phonon excitation with an energy loss in the order of $20\,meV - 1\,eV$,
- intra and interband excitation of the outer atomic electrons, plasmon excitations of valence and conduction electrons in the energy loss range of $1 - 50\,eV$,
- ionizations of core electrons in inner atomic shells above $50\,eV$.

Since the energy spread of the electron beam is in the order of $1\,eV$, energy losses of the order of meV can only be detected if the beam is monochromated.
The second type of inelastic scattering is influenced by the density of valence and conduction electrons, chemical bonds and band structure.
The third type of inelastic scattering is at the base of the analytical techniques used in this work.
Atomic electrons can be excited from an inner shell to an unoccupied energy state above the Fermi level. The scattering angle is determined by the ratio of the ionization energy of the atomic shell and the kinetic energy of the electrons in the beam. The higher the ionization energy the higher the scattering angle. Electron Energy Loss Spectroscopy is therefore the best method for analyzing elements of low atomic number, since there the collection semi angle is typically $< 10\,mrad$.
When an electron from an outer shell fills the gap in the inner shell, the material specific excess energy is emitted as an X-ray quantum or transferred to an Auger electron. With an energy dispersive spectrometer the emitted X-ray can be recorded and the composition of the specimen can be determined. EDS is suited for heavier elements because of their higher fluorescence yield.

5.4.1 Electron Energy Loss Spectroscopy

A schematic representation of the post column Gatan Imaging Filter (GIF) is shown in figure 5.10. It has both spectroscopic and imaging capabilities.
The inelastically scattered electrons are collected by the entrance aperture and focused by the magnetic sector on the dispersion plane, where a slit is positioned.
The magnetic sector fulfills three tasks. It focuses the incoming electrons due to a lens effect of its edge profile, it deflects the electrons and creates a dispersion plane due to a constant applied magnetic field in a normal direction to the electron wave vector. The bending effect occurs due to the Lorentz force, the dispersion effect depends on the kinetic energies exhibited by the inelastically scattered electrons. Electrons with different kinetic energies have different paths in the spectrometer and are focused in a different position on the dispersion plane.
Here an adjustable slit can select the energy range that contributes to the formation either of the image or of the spectrum. Quadrupoles and sextupoles do not only correct aberrations of the magnetic prism but serve also to switch between the spectrometer and the imaging mode. The electrons are then detected by a YAG scintillator fiber optically coupled to a cooled 2k CCD camera.

In figure 5.11 EELS spectra of the low loss region and of ionization edges are shown. These represent the scattered intensity as a function of the decrease in kinetic energy.
The low loss region, $0 - 50\,eV$, contains the zero loss peak, which represents electrons which are transmitted without losing energy. The energy resolution is about $1\,eV$ and energy losses below this value cannot be detected. Electrons inelastically scattered from conduction

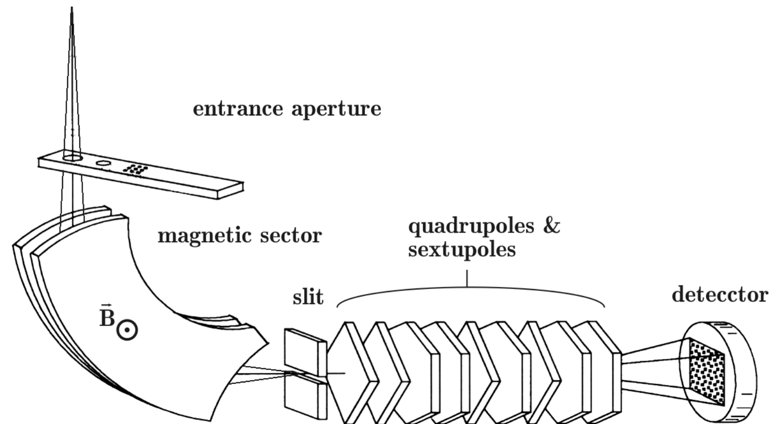

Figure 5.10: ***Schematic representation of the Gatan Imaging Filter*** *- The post column spectrometer collects the transmitted electrons through the entrance aperture and focuses them on the dispersion plane. Here an adjustable slit selects the energy range of the electrons which contributes to the image or spectrum formation. The dispersion action of incoming electrons with different energies is due to an applied constant magnetic field perpendicular to the electron wave vector. After aberration corrections and magnifications the electrons are detected by a YAG scintillator coupled to a 2k CCD camera. After [131]*

electrons are visible as a broad peak (plasmon peak).
For energies above 50 eV intensity variation due to inner shell ionization processes can be identified.
Above the low loss region the intensity falls monotonically, and can be described by the superposition of a background intensity and ionization edge intensity. The background

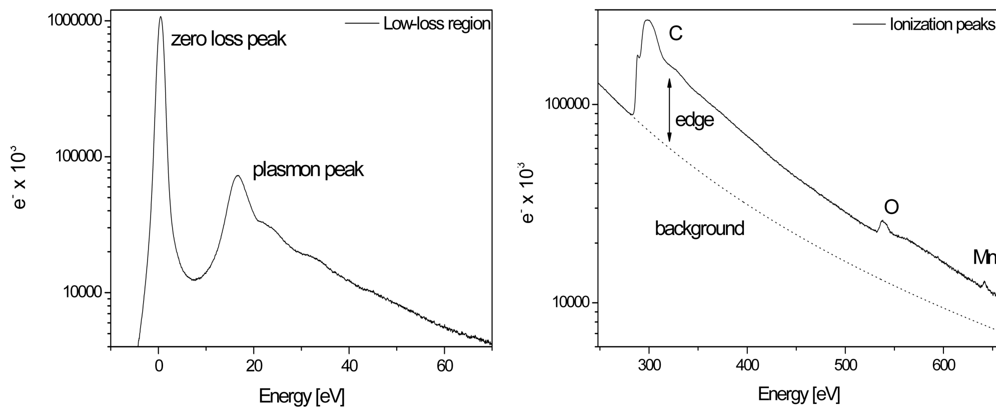

Figure 5.11: ***EELS spectra*** *- Left, the low energy loss arises from the interaction of the high energy electrons with the weak bound atomic electrons. Right, edge peaks correspond to electrons which lose energy due to an ionization process. These peaks reveal the composition of the specimen. For quantitative measurements the background has to be subtracted from the spectrum in order to calculate the total ionization cross section of the elements.*

originates from the excitation of atomic electrons of lower binding energy and has to be subtracted from the spectrum in order to perform a quantitative analysis.
Qualitative analysis, like carried out in this work, relies on the identification of the ionization edges in order to verify the presence of an element in the specimen [132].

5.4.2 Energy Dispersive Spectroscopy

Detector
A Bruker AXS XFlash 530 spectrometer was used for EDS analytical investigations. This spectrometer uses the Silicon Drift Detector (SDD) technology to obtain a high count rate and a low dead time during acquisition.
Due to photo absorption an incoming X-ray quantum generates an electron-hole pair. This can be separated due to the electric field of the formed depletion region in a pn junction.
The charge pulse proportional to the quantum energy is collected by an integrated Field Effect Transistor (FET) in the center of the detector, which acts as first amplification device. The presence of an integrated circuit allows a short connection between the electron collecting anode and the gate of the transistor so that parasitic capacitance can be reduced.
The name Silicon Drift Detector derives from the presence of a voltage gradient along the pn junction which promotes a drift of the generated carriers toward the FET. The output signal of the FET consists of a voltage step proportional to the quantum energy.
The subsequent main amplifier not only amplifies but also shapes the pulses. The improved frequency response of the FET due to reduced parasitic capacitance allows a shorter shaping and registration time. This effect reduces the dead time of the detector during measurements and enhances the count rate.
The shaped pulses are collected, sorted and displayed by a 4096 x 32 bit multichannel analyzer.
A single stage Peltier element reduces the electronic noise. Reduced leakage currents make the use of liquid nitrogen unnecessary.
Finally, in order to perform line scans and scanning maps, an I/O adapter with a scan system is coupled to the microscope and allows the control of the position of the focused beam and its synchronization with the spectrometer.

X-ray emission and specimen holder
An X-ray spectrum is the superposition of the X-ray continuum and characteristic X-ray lines (see figure 5.12).
The first is the result of the acceleration of electrons in the Coulomb field of the nucleus. This radiation is forward directed. The second is related to ionization processes and has an isotropic distribution. However, not every ionization process results in the emission of an X-ray quantum. The X-ray fluorescence yield ω describes the probability that the excess energy of the excited system is released by the emission of a photon and is an increasing function of the atomic number Z, so that the detection of light elements by EDS is inefficient.
In order to maximize the solid angle of X-ray collection, and therefore the count rates, the spectrometer is mounted laterally on the microscope column directly above the specimen with an inclination of 15°.
Analytical double tilt holders with a cut out in the specimen tip allow a higher take off angle of the X-ray, prevent shadowing and allow the orientation of the specimen in its crystallographic direction. The nitrogen cooled version of the analytical holder improves the acquisition conditions due to a lower carbon contamination of the investigated region.

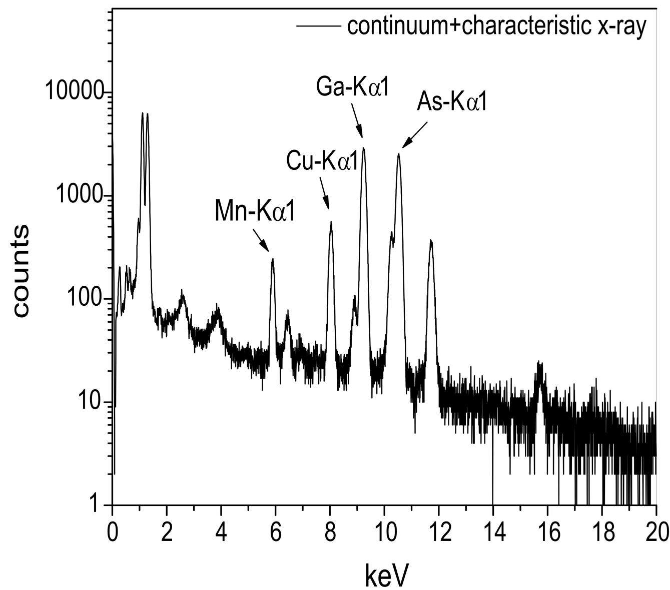

Figure 5.12: ***EDS spectrum*** - *The EDS spectrum shows the superposition of the continuum and the element peaks. The principal Kα-lines of the present elements are shown. The specimen consists of an ultramicrotomy cut of a GaAs/(Ga,Mn)As core/shell NW sample, deposited on a Cu grid. Even if the position of the electron beam is a few micrometers away from the Cu grid, the Cu peak is visible due to fluorescence effects.*

Absorption and fluorescence
The emitted X-rays interact with the specimen and with the solids surrounding the specimen. The main processes occurring are scattering, absorption and photo ionization.
These processes produce an unwanted contribution to the detected spectrum from continuous and characteristic quanta generated not in the irradiated area of the specimen but anywhere in the specimen, in the holder tip and in the column of the microscope.
In order to reduce these contributions to the spectrum, the analytical holder has a beryllium tip. This light element has a very low X-ray absorption coefficient so that it can be considered transparent for X-ray. Furthermore the fluorescent emitted Be X-rays are not efficiently detected and a consistent fluorescent X-ray contribution is suppressed.
Spurious spectral lines cannot be completely avoided. Using a copper grid as support for the ultramicrotomy cuts generates e.g. detectable Cu peaks as can be seen in figure 5.12.

For thick specimens the counts of characteristic X-ray lines does not represent the concentration of elements because of absorption and fluorescence of the radiation in its path between the emission point and the escape point on the specimen surface. In this case the atomic number Z - Absorption - Fluorescence (ZAF) correction should be applied.
In the following the thin specimen approximation is verified for the Au-Ga droplet system. The validity of the approximation ensures the correctness of the association of the measured peak intensity to the elemental concentration in the specimen.

Cliff-Lorimer factors
If the ratio of the concentration of two elements c_a/c_b is of interest, the ratio of the counts of the peaks N_a/N_b of the two elements has to be evaluated. This ratio method is independent

of the local mass thickness x of the specimen if the absorption correction can be neglected. Otherwise different absorption coefficient for the two characteristic X-rays may alter the ratio.
The Cliff-Lorimer factors are the proportionality constants between the count and the concentration ratio and depend not only on material specific parameters like the ionization cross section and the fluorescent yield, but also on microscope-detector specific parameters like the collection efficiency.
The Cliff-Lorimer factors are therefore determined experimentally by measuring the count rate of pure element films, and are specific for the used microscope-detector configuration and acquisition conditions.
Since the spectrometer was installed during the last phase of the PhD period the Cliff-Lorimer factors are not available and only qualitative conclusions can be drawn from the measurements.

Spatial resolution
Other than by bulk specimen analyzed in a SEM where the spatial resolution is limited to $0.1 - 1\,\mu m$ by the diameter of the electron diffusion cloud, in a TEM the high energy of the incoming electrons and the thin specimen does not produce beam broadening due to the high mean free path of the electrons and consequently leads to a low multiple scattering probability.

EDS measurements and ZAF correction applied to Au-Ga droplets
The variation of the ratio of the $Ga_{K_{\alpha_1}}$ and $Au_{L_{\alpha_1}}$ peak heights in the different crystallized Au-Ga droplets will be used as an indication of the differences of the Ga concentration in the droplets.
As explained below, the ZAF correction of the spectra is not necessary because of the validity of the thin film approximation which ensures a negligible value of the mass attenuation coefficient. The count ratio is therefore proportional to the relative concentration of Au and Ga in the droplet.

X-ray absorption can affect the experimental spectra and alter the effective Ga/Au ratio. In order to apply the thin film approximation the condition

$$\chi \cdot x = \frac{\mu}{\rho} \cdot cosec(\psi) \cdot \rho \cdot t \ll 1 \tag{5.2}$$

should be satisfied. $\chi \cdot x$ describes the probability that a photon is absorbed on its path way towards the detector and is characterized by the mass attenuation coefficient μ/ρ, the density of the material ρ, the take off angle ψ and the sample thickness t. A worst case analysis will be performed.
From figure 5.13 the values of the mass attenuation coefficients μ/ρ of gold and gallium at the $Ga_{K_{\alpha_1}}$ and $Au_{L_{\alpha_1}}$ peak energies can be obtained. Only the Au values of μ/ρ will be considered, since gold is the prevalent element of the droplet and possesses the higher mass attenuation coefficient at the considered energies.
The take off angle ψ is assumed to be 27.7°. This is the sum of the minimum tilt angle used for the investigations and the angle at which the detector is mounted in respect to the microscope axis (see figure 5.14).
With these parameters and considering the density of the droplet as the density of gold $\rho = 19.3\,g/cm^3$ and the specimen thickness as the highest diameter value of the investigated

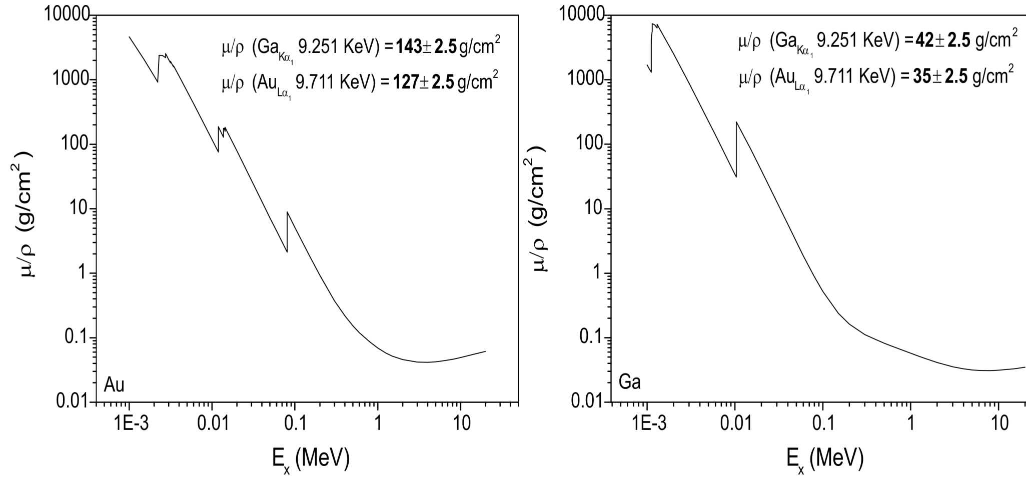

Figure 5.13: ***Mass attenuation coefficient*** *- Left: gold mass attenuation coefficient. Right: gallium mass attenuation coefficient. The values for the $Ga_{K\alpha_1}$ and $Au_{L\alpha_1}$ spectral lines are indicated.*
Data from [http://physics.nist.gov/PhysRefData/XrayMassCoef/ElemTab/z79.html]
[http://physics.nist.gov/PhysRefData/XrayMassCoef/ElemTab/z31.html].

droplets, $136 \pm 1.3\,nm$, the obtained values for $\chi \cdot x$ are:

$$\chi \cdot x_{(Ga_{K_{\alpha_1}})} = 0.072 \pm 0.002 \tag{5.3}$$

$$\chi \cdot x_{(Au_{L_{\alpha_1}})} = 0.081 \pm 0.003. \tag{5.4}$$

The fraction of photons leaving the specimen, considering the approximated expression

$$f(\chi) \backsimeq 1 - \frac{1}{2}\chi \cdot x \tag{5.5}$$

corresponds respectively to 0.964 ± 0.001 for the $Ga_{K_{\alpha_1}}$ peak and to 0.959 ± 0.001 for the $Au_{L_{\alpha_1}}$ peak [131]. Considering the worst case approach of the estimation and the qualitative character of the analysis the thin film approximation can be safely adopted, and the absorption correction should not be applied.
For thin films also the atomic number correction can be neglected. This is because the ionization cross section σ_a does not significantly increase due to a decrease of the mean electron energy in the specimen caused by energy losses.
Generally a peak ratio could be influenced by the secondary emission of X-rays. The possible contribution of fluorescent emission should be subtracted from the peak heights, in order to obtain a Ga/Au ratio representative for the concentration ratio in the droplet.
From the analysis of the edge energy differences between Au and Ga peaks it can be concluded that the only generated fluorescent radiation of interest is the $Ga_{K_{\alpha_1}}$ line, excited by the Au_{L_β} photons. The fluorescence emission produced by this combination of spectral lines is not significant, as reported by K. F. J. Heinrich, and therefore a fluorescence correction will not be considered in the data analysis [133].

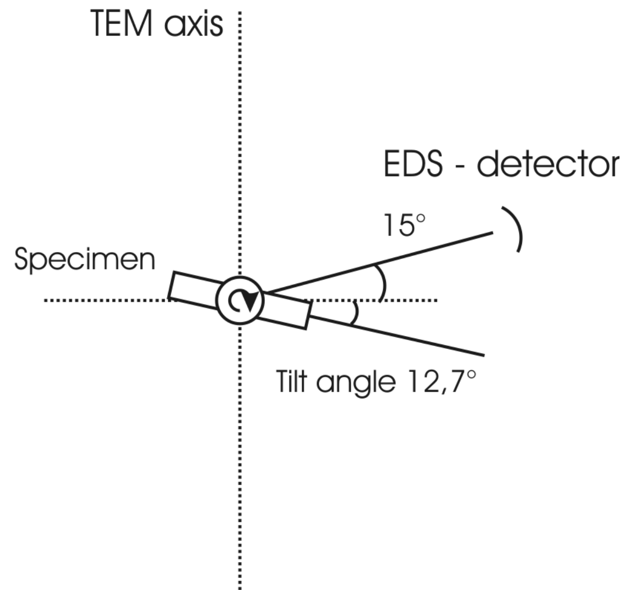

Figure 5.14: ***Spectrometer alignment*** *- The EDS detector forms an angle of 15° to the plane normal to the TEM axis. The specimen can be tilted in order to orient the crystal. The take off angle of the photons is the sum of the fixed angle of the detector and the variable angle of the specimen, both measured from the plane normal to the TEM axis.*

The evaluation of EDS spectra of Au-Ga particles considering the Ga/Au ratio as an indication of the Ga concentration is therefore a reliable method.
The peak heights of the edges are determined considering the height of a Gaussian fit of the spectral lines and subtracting the background value. The error is considered as the mean value of the residuals in the proximity of the peak.

Results and discussion

6 Growth parameters and crystal structure

In the Preferential Interface Nucleation (PIN) mechanism the correlation between growth parameters like arsenic and gallium fluxes and the crystal structure of the NWs is not completely understood and the publications on this topic show in many cases controversial results [62]. The ultimate purpose of the research in this field is the control of the crystal structure adopted by III-V semiconductor NWs.
The aim of this chapter is the comparison of the crystal structure of NWs grown under different conditions in order to determine a clear correlation between the used growth parameters and the resulting crystal phase. The latter depends on the Ga content in the droplet during growth which is determined by the growth parameters. EDS measurements reveal the Ga content of the crystallized droplets and are the starting point for identifying the Ga content in the droplet during growth.

6.1 Ga content of the crystallized droplets

The Ga concentration in the Au droplet influences the energetic balance of the growth process and together with the surface energies of the NW sidewalls determines the crystal structure of the Au-assisted grown NWs.

Four different samples were grown using different As_4/Ga flux ratios (see tab. 6.1). EDS measurements were carried on the crystallized particles of different NWs of samples A and C. These samples have extremal As_4/Ga flux ratios. The chosen particles have different dimensions, showing in the projection a diameter ranging from ca. $20\,nm$ to ca. $140\,nm$. As stated in chapter 5 the $Ga_{K\alpha1}/Au_{L\alpha1}$ peak ratio can be considered as a reliable parameter for investigating the Ga content in the crystallized particles because of the validity of the thin film approximation. The measurements were carried on the central part of the particles focusing the electron beam in a few nanometer large spot. Three NWs of sample A and five NWs of sample C were analyzed. The results are shown in figure 6.1.
The Ga/Au peak ratio increases when the droplet dimension increases. The investigated samples, A and C, were grown respectively with an As_4/Ga flux ratio of 3.90 and 1.70. Both show the same dependency of the Ga/Au peak ratio from the droplet diameter, suggesting that this behavior is general and is not related to growth parameters.
This result is somehow surprising because intuitively one would expect that when a high

Sample	As_4 flux [$10^{-6} mbar$ $(Torr)$]	Ga rate [nm/s]	As_4/Ga ratio	Temp. [°C]
(A) C081212B	1.70 (1.28)	0.038	3.90	534
(B) C090304A	2,76 (2.07)	0.113	2.20	540
(C) C090728B	1.63 (1.22)	0.085	1.70	534
(D) C100308A	1.61 (1.21)	0.080	1.77	539

Table 6.1: ***Growth parameters*** *- The four investigated samples were grown using different As_4/Ga flux ratios.*

Ga flux is chosen for the growth, both the Ga content during growth and the residual Ga content should be higher than that of droplets of comparable dimensions exposed to a lower Ga flux. Furthermore the presence of droplets with a vanishing Ga content could be interpreted as an evidence of a solid state of droplets during growth because of their nearly pure Au character.
Harmand et al. investigated the composition of crystallized droplets by EDS [134]. They report of an almost pure Au phase for droplets with diameter below 10 nm. Furthermore they detected the β' Au_7Ga_2 phase and the AuGa phase but no further diameter dependencies were reported in their work. Harmand et al. relate the occurrence of a nearly pure Au phase to Ga consumption during the termination regime. This means that during growth no pure Au droplet is expected, and the minimum Ga molar fraction is estimated to be 0.25, which

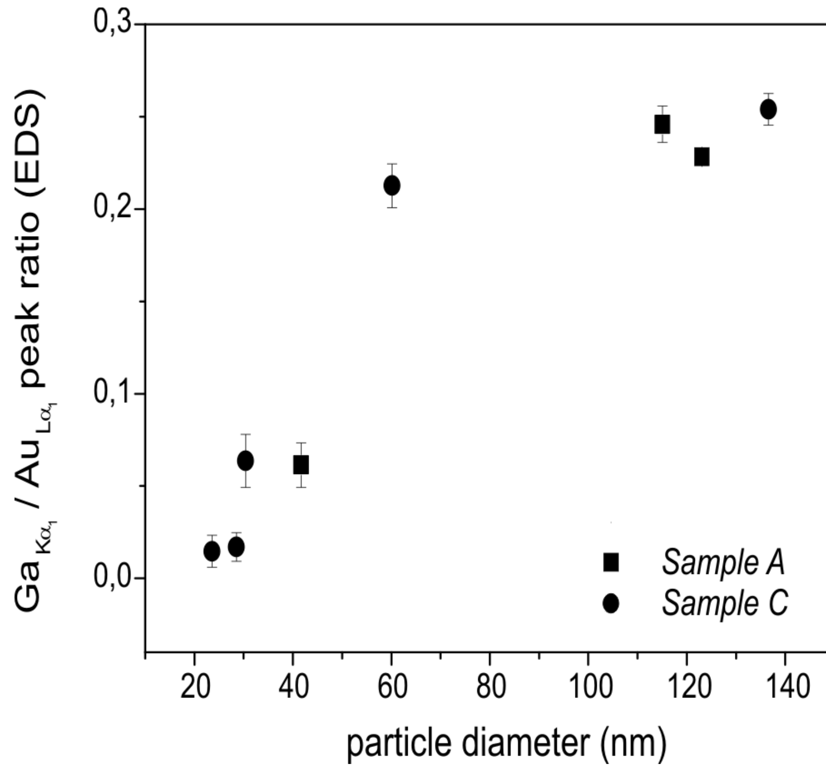

Figure 6.1: ***Diameter dependent Ga/Au peak ratio of crystallized particles*** *- The $Ga_{K\alpha1}/Au_{L\alpha1}$ peak ratio of the crystallized particles increases with their diameter. This behavior holds for both investigated samples, A and C, indicating a general validity of the result.*

is consistent with the liquid phase of the droplet (see phase diagram in figure 1.3) [134]. Even if Ga consumption occurs, the occurrence of the same dependency of the Ga/Au ratio from the droplet diameter in samples grown using different As_4/Ga flux ratios is a result that requires further investigations. It has to be verified if the detected relation between Ga/Au ratios of droplets with different dimensions is the same also during growth. For this purpose the NW crystal structure is analyzed as a function of the droplet diameter and the results are interpreted within the nucleation theory proposed by Glas et al. [33]. The adopted crystal structure gives an indication on the Ga content in the droplet during growth.

In figure 6.2 the occurrence of ZB segments in the NW crystal structure for the four investigated samples is depicted as a function of the droplet diameter. The investigations on the crystal structure were done by a combination of HRTEM techniques and DP analysis (see chapter 5). There is a strong evidence that ZB segments are more probable to appear when the crystallized droplet diameter is below 40 nm.
As a first interpretation of this result one can think that during growth the same relationship as measured ex situ between droplet diameter and Ga content holds. In fact the nucleation theory proposed by Glas et al. states that for low Ga content in the droplet, center nucleation occurs and the ZB structure is favored. However, if one considers the used As_4/Ga flux ratio (see figure 6.2), one observes that the samples grown in a Ga rich environment

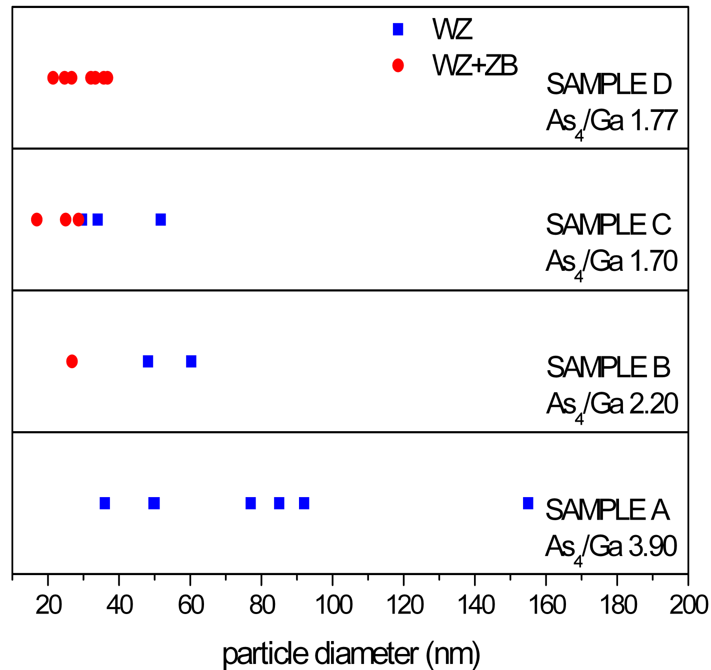

Figure 6.2: ***Diameter dependent crystal structure of crystallized particles*** *- Squares represent NWs with WZ crystal structure and SFs, dots represent NWs with WZ crystal structure, SF and ZB segments. The occurrence of ZB segments in the crystal structure of a NW is most probable when the droplet diameter is less than 40 nm and the As_4/Ga ratio is at least 2.20.*

have a higher probability to show ZB segments. Droplets with a diameter below 40 nm are very sensitive to enhanced values of the Ga flux because of their small volume. Since investigations on Ga assisted grown NWs show that a pure Ga droplet has a high probability to generate ZB segments, also the interpretation that droplets with a diameter below 40 nm have a extremely high Ga concentration during growth has to be considered.
For solving this question the droplet dimension before termination regime and the Ga consumption rate during the termination regime are the quantities that one has to know in order to estimate the Ga content of the droplets during growth.
Furthermore the adequacy of macroscopic parameter like the As_4/Ga flux ratio to describe the state of the particle during growth is questionable when a high variance of the droplet dimensions occurs. Local parameters should be used to indicate the state of the droplets and to compare the crystal structure of single NWs.

Considering NW specific parameters instead of beam fluxes

The kinetic model of NW growth proposed by Dubrovskii assumes that the axial growth via the PIN method is governed by the diffusion of Ga adatoms towards the droplet. The nucleation rate increases with an increasing Ga adatom diffusion flux due to the increased supersaturation in the droplet. The substrate and sidewall collection area, respectively $A_{Substrate}$ and $A_{Sidewall}$, determine for each NW the effective Ga flux and are influenced by:

- the droplet dimension and
- the local NW density.

$A_{Substrate}$ is determined by both the local NW density and the droplet diameter because during the initial phase of the growth the droplets compete for the material. The temporal evolution of $A_{Sidewall}$ depends on the droplet diameter. Smaller droplets show a higher growth rate leading to a faster increasing sidewall collection surface.
Both droplet dimensions and NW density vary over the substrate so that the effective Ga flux towards the droplet, and therefore its Ga concentration, depend on the particular configuration of these parameters. For these reasons general growth parameters do not describe the thermodynamical droplet state of single NWs during growth. The comparison of characteristics of single NWs, that relays on the assumption of identical droplet states, will lead to an incorrect interpretation of the results.

The gallium depletion rate of a droplet is limited mainly by the As concentration in the catalyst, because this represents the limiting factor of the nucleation rate. The spreading time needed to completely cover the NW surface i.e. to form one monolayer is considered much smaller than the time necessary to a nucleus for reaching its critical size, and is therefore neglected [135, 136]. Since it is assumed that As is provided to the droplet directly from the vapor phase, the As flux in the chamber correctly describes the As supply to the single droplet and there is no need to relate this parameter to local growth conditions.

Depending on kinetic processes, influenced by local conditions and catalyst dimensions, the droplet can accumulate gallium and consequently change its thermodynamical state. The growth conditions of the MBE system, determined at a given temperature by the arsenic and gallium fluxes, influences the mean value of the distribution of the droplet states. The local density of NWs and the initial Au droplet dimension determine if the growth of each

NW has a steady state character or not. A variation of the Ga concentration in the droplet during growth corresponds to a non steady-state regime.
The comparison of crystal structure characteristics of single NWs should be done classifying the NWs by the Ga concentration and the dimension of the catalyst during growth.
These parameters are not experimentally accessible, as these parameters change after the termination: i.e. the diameter of the droplet decreases as well as the Ga concentration, as the NWs continue to grow after the effusion cells are closed.
The Ga concentration of the catalysts after growth together with the growth history of the NWs should be considered to obtain information about the thermodynamical state of the liquid particle.

6.2 Droplet state during growth

An indication of the Ga concentration of the droplets during growth is given by the relation between crystallized droplet diameter and NW diameter. Since the PIN growth mechanism presumes that the droplet determines the diameter of the growing NW, during growth the top surface of the NWs is entirely covered by the droplet. When in HRTEM pictures the contact line between droplet and NW has the same extension as the NW diameter (see right NW of figure 6.3) one can assume that no significant volume reduction and therefore Ga consumption occurred during termination. If the contact line between droplet and NW is significantly different (see left NW of figure 6.3) it can be assumed that Ga was incorporated into the NW.
5 of 8 investigated NWs are shown at the bottom of figure 6.3. From left to right the diameter of the droplet increases. From EDS we know that the crystallized droplets on the left side have a lower Ga content than the droplets on the right side. It can be also seen that the difference between the NW diameter and the droplet diameter decreases from the left to the right, which means that the droplets on the left side have a higher Ga concentration during growth than after crystallization. For droplets on the right side the Ga concentration before and after crystallization can be assumed to be the same.
Qualitatively two types of droplets can be distinguished: type 1 and type 2 droplets are those at the extremes of figure 6.3 and correspond to low and high differences between NW and droplet diameter respectively. Accordingly to this categorization the graph showing the EDS Ga/Au peak ratio is redrawn and is shown at the top of figure 6.3. A quantitative definition of type 1 and type 2 droplets will be proposed later in the chapter. The following considerations can be done: droplets having a lower Ga content in their solid state as measured by EDS, are supposed to contain much more Ga during their liquid phase due to an evident difference of the NW and droplet diameter; droplets having a higher Ga content in their final solid state, are supposed to maintain the same Ga content as during growth because of the vanishing difference between the NW and droplet diameter.
Considerations on the nucleation rate support this interpretation of the results. Droplets with a high Ga concentration have a higher nucleation rate than droplets with a low Ga concentration. If one applies these considerations to the termination regime when the Ga cell is closed and the As cell is still open, it follows that droplets with a higher residual Ga concentration consume it faster than droplets with a lower residual Ga concentration.

This picture of the evolution of the droplet state during termination and the assumed relation between Ga concentration and diameter difference between crystallized droplet and NW body are confirmed by the micrographs shown in figure 6.4. The droplet at the left side is a type 1 droplet, the droplet at the center is an extreme case of a type 2 droplet. Only

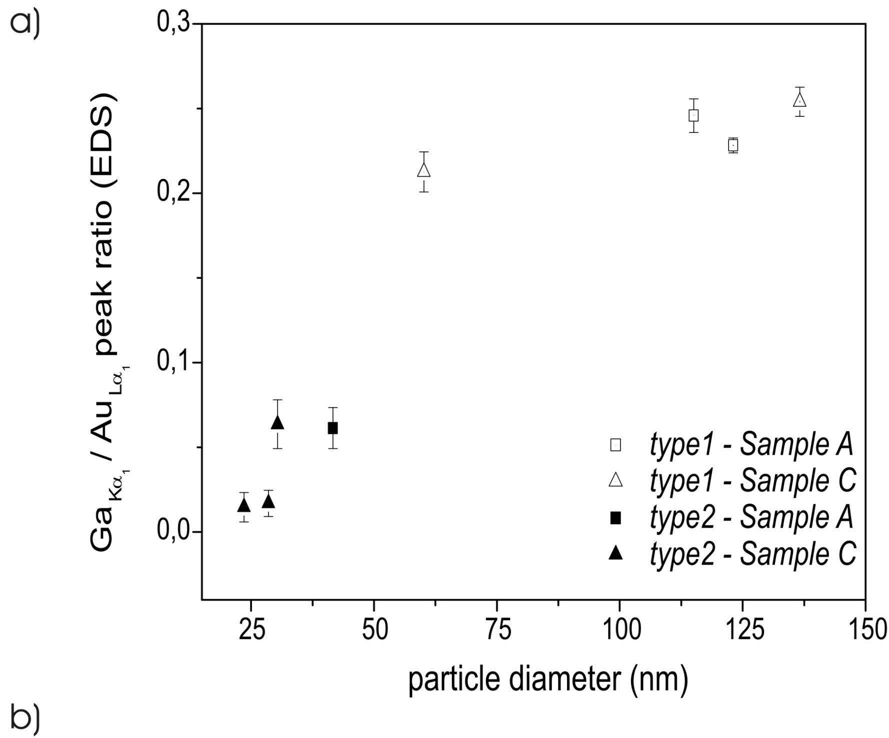

Figure 6.3: ***Diameter dependent Ga/Au peak ratio of crystallized particles*** - *a) EDS Ga/Au peak ratio of the crystallized particles as a function of their diameter. The graphic 6.1 is now redrawn considering the classification of NW in two classes as defined in figure 6.3 b). Here HRTEM micrographs of 5 of the 8 measured droplets are shown. The largest and smallest measured droplets are on the right and on the left respectively. The continuous white line indicates the droplet diameter and increases from left to right, the dotted white line indicates the NW diameter. The difference between these two quantities decreases from left to right. This properties will be used for the classification of the NWs.*

considering a higher volume of the droplet during growth the morphology of type 2 droplets can be explained.

On the right side the droplet of a NW grown with an As_4/Ga ratio of 0.7 is shown. A ratio of 0.7 is not representative of typical NW growth conditions and was used to investigate the effect of an excess Ga supply. The shown micrograph demonstrates that any Ga concentration in the droplet is allowed during growth. After termination a pure gallium particle forms (EDS measurements not shown). Inside the Ga volume a second droplet can be identified. This second particle contains gold. Since the Au-Ga alloy is an eutectic mixture the solid phase presents a solubility gap that gives rise to phase segregation. The Au-Ga phase diagram of figure 1.3 shows that in the Ga rich part when the melt cools down a pure Ga solid phase and a $AuGa_2$ phase forms.

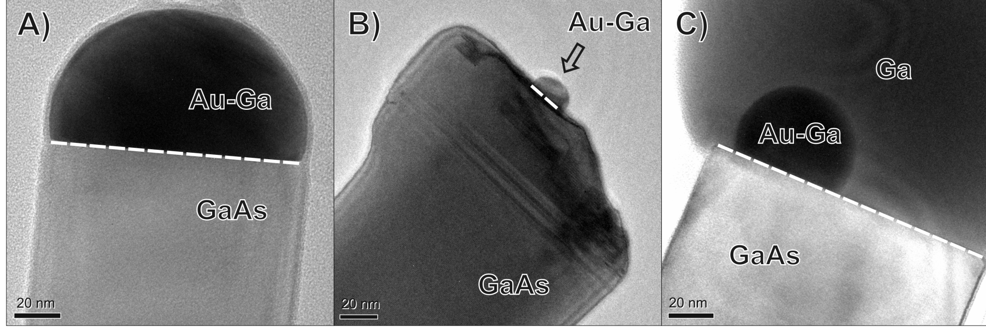

Figure 6.4: ***NW/droplet line of contact and Au segregation*** - *HRTEM images of the side view of NWs showing the line of contact between droplet and nanowire (white dashed line). A) example of a NW with the top surface entirely covered by the crystallized particle. B) example of a NW with the top surface partially covered by the crystallized particle. C) example of a NW showing an Au-Ga particle contained in a pure Ga droplet. This NW was grown under an extreme high Ga supply and does not belong to the four investigated samples listed in table 6.1.*

From this results it can be concluded that the catalyst dimension during growth can increase independently from the original Au volume developing a non steady state growth and therefore any Ga concentration in the droplet is allowed. Furthermore during termination incorporation of the residual gallium into the NWs occurs. The evolution of the state of the droplet during the termination is responsible for the discrepancy between measured and effective Ga content. The growth history and also the termination sequence influences the detected Ga concentration in the crystallized particle.

6.3 NWs crystal structure and droplet state

The diameter difference between the NW and its droplet (aspect ratio) will be used as a qualitative description of the Ga concentration in the liquid droplet:

$$aspect\,ratio = \frac{\varnothing_{NW} - \varnothing_{particle}}{\varnothing_{NW}}. \tag{6.6}$$

An aspect ratio of 0 characterizes a NW with a particle diameter equal to the NW diameter. An aspect ratio approaching 1 characterizes a NW with a particle diameter much smaller than the NW diameter. It is a normalized value and represents the variation of the droplet diameter relative to NW body diameter. This approach is valid for type 2 droplets. Type 1 droplets will be described by the equilibrium state calculated in [79] (see subsection 6.4).
The aspect ratio allows the comparison of NWs grown with different macroscopic parameters and also of NWs of the same sample with a different content of gold in the droplet. The advantage of considering the diameter difference and not the arsenic to gallium flux ratio as a description of the state of the droplet allows a NW specific analysis, which is representative of the non homogeneity of the local growth conditions on the substrate. The NW crystal structure of the four investigated samples will be analyzed in relation to the aspect ratio of the single NWs.
The results are summarized in figure 6.5 and represents the same data set shown in figure

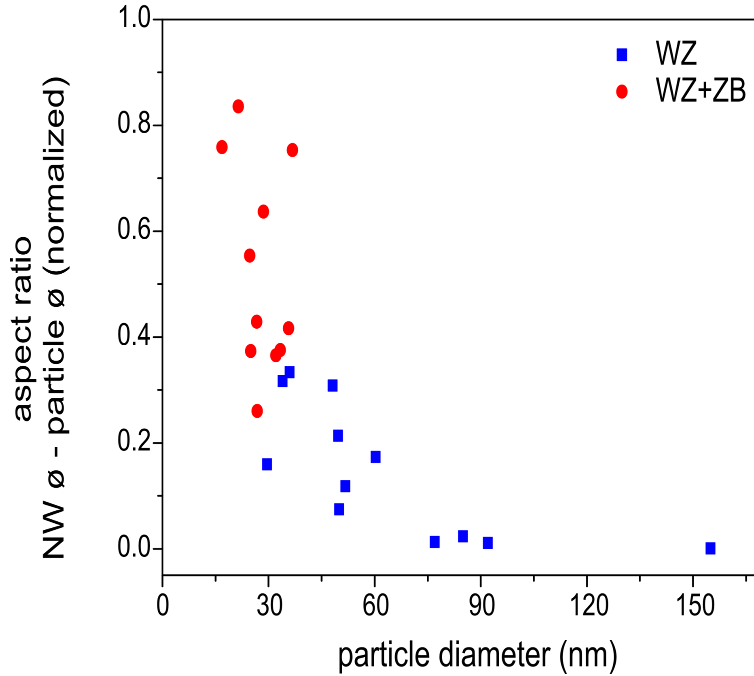

Figure 6.5: ***Crystal structure as a function of the particle diameter and aspect ratio*** - *Squares represent NWs with WZ crystal structure and SFs, dots represent NWs with WZ crystal structure, SF and ZB segments. The y-axis gives the aspect ratio of the NWs. The x-axis shows the diameter of the crystallized particles. ZB segments can be observed for NWs with a small particle < 40 nm and an aspect ratio > 0.3. The investigated NWs belong to four different samples as listed in table 6.1. The error bars are smaller than the plotted symbols.*

6.2.
NWs containing ZB segments have a particle diameter $< 40\,nm$ and an aspect ratio > 0.3 (type 2). It can be concluded that a higher Ga concentration during growth favors the nucleation of ZB segments.

The correlation between Ga concentration and crystal structure proposed in the nucleation theory described in chapter 1 for the Au assisted growth method states that the higher is the Ga content the higher is the probability to obtain WZ segments. The results presented in figure 6.5 show in contrast an increased probability to obtain ZB segments if the Ga concentration during growth increases.
The same nucleation theory predicts that for the Ga-assisted growth method the nucleation in ZB position is more probable than that in WZ position [102]. A possible interpretation is therefore that if the Au droplet accumulates gallium over a threshold value, the growth can be considered as being pseudo Ga-assisted (type 2 droplet) and no more Au-assisted (type 1 droplet).
In figure 6.6 the same data set is plotted separately for each investigated sample. As stated in paragraph 6.1 the global As_4/Ga flux ratio influences the mean value of the thermodynamical state of the droplets. Considering a distribution of the particle diameter ranging from tens to hundreds of nanometers, one would expect that the mean value of the calculated aspect ratio

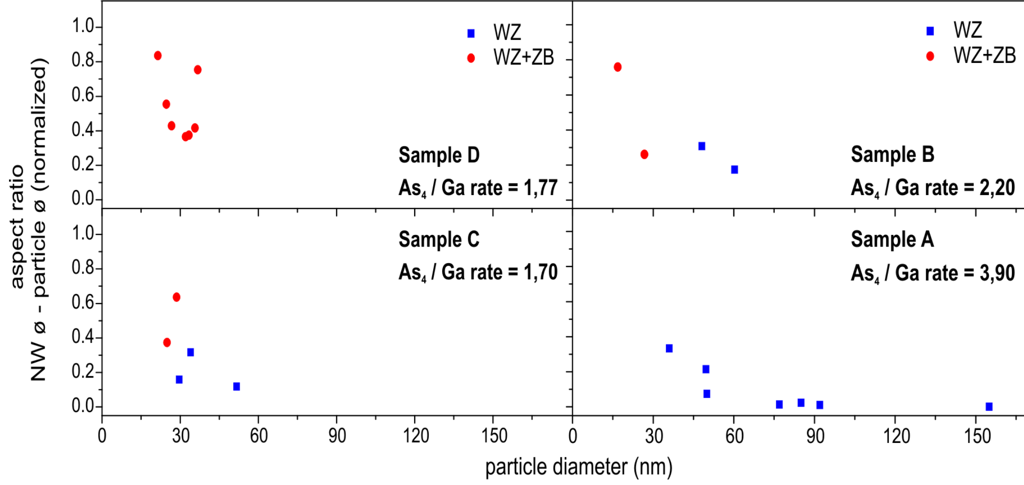

Figure 6.6: ***Crystal structure as a function of the particle diameter and aspect ratio*** *- the same data set as in figure 6.5 is plotted for each sample separately. The As_4/Ga ratio influences the probability to observe ZB segments. Samples A, B and C have had the same Au film thickness (0.1 nm) but different As_4/Ga ratios were used during growth. The higher the Ga supply the higher the probability to observe ZB segments in the crystal structures. Also for NWs of the same sample this trend is valid. The aspect ratio is the parameter used for comparing the Ga concentration of liquid droplets of different NWs. ZB segments appears for an aspect ratio $>$ 0.3. Sample D has had an Au film thickness of nominally 0.15 nm. The crystallized droplets have a diameter $<$ 36 nm and an aspect ratio $>$ 0.36. All the investigated NWs show ZB segments. The error bars are omitted. The extension of the dots and of the squares represents the uncertainty of the indicated quantities.*

will decrease with an increasing flux ratio because of the lower Ga flux during growth. In fact the mean value of the aspect ratio of the investigated NWs decreases with an increasing As_4/Ga flux ratio, confirming this statement (see table 6.2). Since the statistic over the diameter range is poor, this remains only a qualitative proof. Also the effect of the particle dimension is evident. At a given As_4/Ga flux ratio smaller particles have a higher aspect ratio and therefore a higher Ga concentration during growth.

6.4 Calculation of the Ga content during growth

The termination sequence was the same for all samples. The first step consists of closing the Ga cells shutter and switching off the heating stage. After the temperature reaches 400 °C also the shutter of the As cell is closed. The catalyst composition at the beginning of termination however is different from droplet to droplet as well as the nucleation rate. This

Sample	As_4/Ga ratio	aspect ratio mean value
(A) C081212B	3.90	0.09
(B) C090304A	2.20	0.32
(C) C090728B	1.70	0.37
(D) C100308A	1.77	0.53

Table 6.2: ***Mean value of As_4/Ga ratio for the investigated samples***

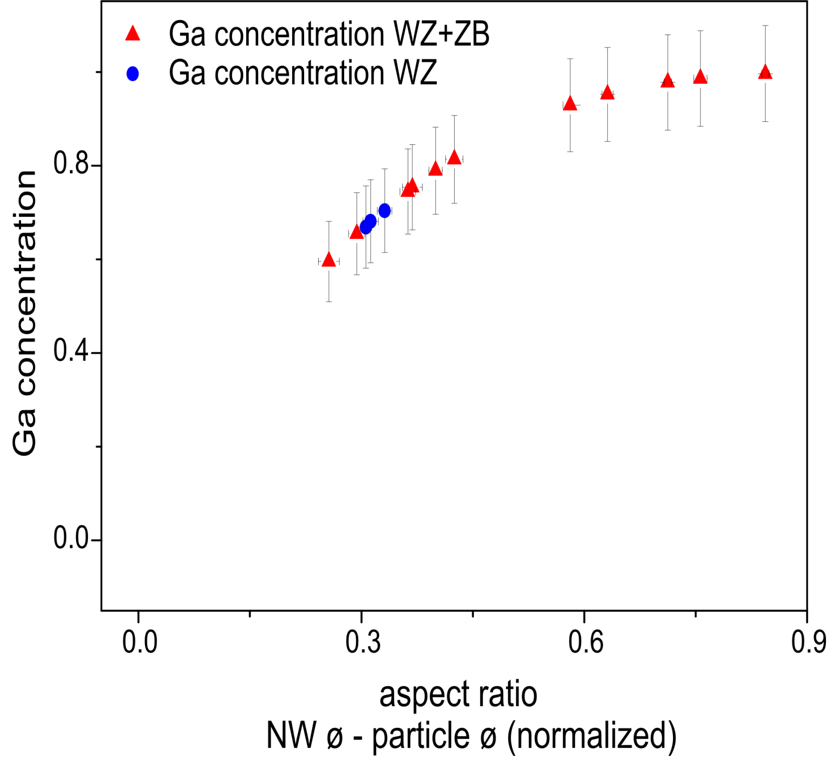

Figure 6.7: ***Ga concentration during growth*** - *The estimation of the Ga concentration during growth shows that type 2 droplets (aspect ratio > 0.3) should have a Ga content of at least 0.60.*

leads to different Ga consumption rates and solidification temperatures for the two types of droplets. The isothermal section of the Au-Ga-As ternary phase diagram calculated for MBE conditions shows that for low Au concentration the droplet behaves like an As-Ga binary alloy [79].
The two types of droplets can be described as follows: type 1 droplets are essentially Au-Ga droplets as calculated in [79] with $x_{Au} = 0.509$, $x_{Ga} = 0.49$ and $x_{As} = 0.001$, x being the molar fraction, with a solidification point as can be deduced from the Au-Ga phase diagram of about 340°C, also experimentally confirmed [93]. Type 2 droplets resemble the droplets of the Ga-assisted method and are better described during growth by the As-Ga phase diagram. The solidification point depends on the Ga consumption rate and can differ from 340 °C.
The threshold between the two states of the droplet is not defined, it should correspond at least to a Ga molar fraction of 0.49.
In order to estimate a threshold value of the Ga concentration, calculations of the volume of type 2 droplets are performed. A contact angle β of 90° is assumed. This value arises from TEM analysis of contact angles of NWs grown with the Ga-assisted method. 90° is not the common observed contact angle of Ga droplets after crystallization but represents the minimum detected angle. It should be noted that the common value of β utilized in the literature for surface energy calculations of Ga droplets is 120° [33]. Considering also that during the termination a part of the volume of the measured droplets is consumed, $\beta = 90°$ represents a lower boundary for the contact angle of type 2 droplets. Therefore the calculated value is the minimum volume of the droplet during growth.
The droplets are considered to be hemispheres. The Ga concentration is obtained by sub-

$\gamma_{WV-(WZ1\bar{1}00)}$ [J/m^2]	1.3
$\gamma_{WV-(WZ11\bar{2}0)}$ [J/m^2]	1.543
γ_{SL} [J/m^2]	0.59
$\gamma_{VL}(Au) - \gamma_{VL}(Ga)$ [J/m^2]	1.25 - 0.67

c_{Au} [J/($m^2 \times$ °C)]	7.0×10^{-5}
c_{Ga} [J/($m^2 \times$ °C)]	2.0×10^{-4}
T_{m-Au} [°C]	1065
T_{m-Ga} [°C]	30

Table 6.3: ***Parameters utilized for the calculation of the droplet surface energy*** *- also used for calculating which nucleation is favored [102, 137].*

tracting from the estimated volume the volume of the crystallized droplet assumed to be pure Au and then calculating the ratio.

The calculated minimum Ga concentration for a type 2 droplet during growth is approximately 0.6 (see figure 6.7). The range 0.25 - 0.35 of the aspect ratio represents a transition region. NWs showing both, only WZ and WZ+ZB segments, are present. Due to the large error in the calculation of the volumes, the determined minimum Ga concentration of type 2 droplets should be considered as a rough estimation. Nevertheless the validity of the obtained value should be confirmed by calculating the nucleation conditions, in order to see if the correct crystal phase is predicted. According to the nucleation theory, in order to obtain a ZB nucleus, the surface energies of the NW droplet system should favor the nucleation at the center of the catalyst and not at the triple phase boundary.

As stated in chapter 1 the condition for nucleation at the TPB to occur is given by

$$\Delta\gamma = \gamma_{WV} - \gamma_{SL} - \gamma_{LV} sin\beta < 0 \tag{6.7}$$

where γ_{WV} is the WZ sidewall surface energy, γ_{SL} the solid-liquid surface energy, γ_{LV} the droplet surface energy and β the contact angle of the droplet. Only if the inequality is satisfied the system can minimize the energy by nucleating at the TPB. $\Delta\gamma = \gamma_{TPB} - \gamma_C$ is the difference in surface energy for nuclei at the two considered position: at the TPB and at the center of the droplet. A positive value of the difference in $\Delta\gamma$ will favor the nucleation at the center of the droplet. In this case a ZB nucleus is favored.
The solid-liquid surface energy is constant for the ZB and WZ nuclei because of the close atomic environments on the surface around the two types of nuclei [33, 42, 102]. The droplet surface energies of pure gold and pure gallium are calculated for a growth temperature of 540 °C using the linear interpolation formula

$$\gamma_{LV}(T) = \gamma_{LV}(T_m) - c(T - T_m) \tag{6.8}$$

and then considering a linear decrease of γ_{LV} from the Au value to the Ga value as a function of the Ga concentration [102]. Here T_m is the melting temperature of the elements and c an element specific coefficient.
The sidewall surface energy depends on the shape of the cross section of the NWs. Hexagonal NWs with {11$\bar{2}$0} or {1$\bar{1}$00} facets are considered. The calculated surface energies consider the nearest and the next nearest neighbors for the determination of the dangling bonds [137]. The surface reconstruction of WZ GaAs surfaces is unknown. The utilized published values and constants are summarized in table 6.3 .

In figure 6.8 $\Delta\gamma$ is plotted as a function of the droplet surface energy and of the Ga molar fraction. The investigated NWs show predominantly a hexagonal cross section, with $\{11\bar{2}0\}$ sidewalls. The condition for nucleation at the TPB for a Ga molar fraction of 0.6 is not satisfied. This implies a higher probability to observe ZB segments in the crystal structure, in agreement with our results.
The upper plot indicates that for NWs showing $\{1\bar{1}00\}$ sidewalls the nucleation occurs at the TPB until the Ga molar fraction is in the range 0.75-0.95. $\{1\bar{1}00\}$ sidewall NWs are uncommon and the investigated NWs showing a polygonal cross section with $\{11\bar{2}0\}$ and $\{1\bar{1}00\}$ sidewalls have an aspect ratio < 0.1. The Ga molar fraction during growth for this kind of NWs and generally for hexagonal NWs with $\{11\bar{2}0\}$ sidewalls and an aspect ratio $<$ 0.3 can be assumed to be in the range 0.24-0.50. The lower boundary corresponds to the minimum value of the residual gallium of a Au-Ga phase as determined in [93] and the upper boundary is the equilibrium concentration calculated in [79]. The contact angle for droplets with a low Ga content is most likely near 90° because of the increased droplet surface energy. For this Ga molar fraction and for both orientations of the surface energies $\Delta\gamma < 0$ and the nucleation at the TPB is favored. As shown in figure 6.5 NWs with an aspect ratio < 0.3 show WZ crystal structure.

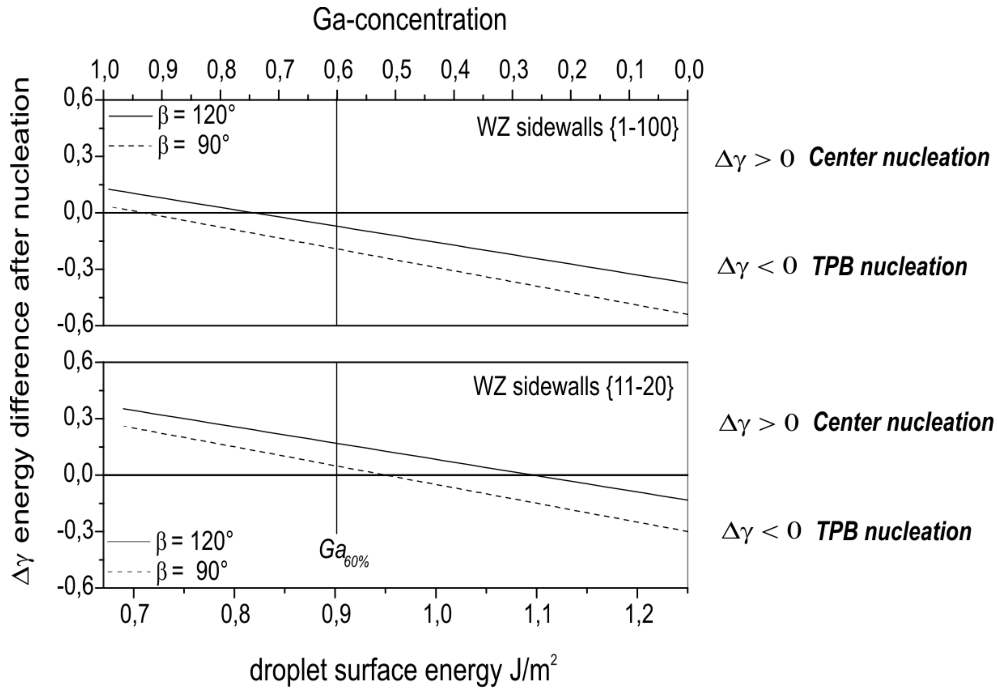

Figure 6.8: ***Condition for the TPB nucleation as function of the droplet surface energy*** *- The quantity $\Delta\gamma = \gamma_{WV} - \gamma_{SL} - \gamma_{LV} sin\beta$ is plotted as a function of the droplet surface energy (lower x-axis) and of the Ga molar fraction (upper x-axis). Two orientations of the WZ sidewalls were considered, the $\{1\bar{1}00\}$ (up) and the $\{11\bar{2}0\}$ (down). The curve calculated for $\beta = 90°$ is to consider as a lower boundary for catalysts with a high Ga molar fraction and as a plausible value for the droplets with a low Ga content. A contact angle of 120° is assumed for Ga rich catalysts. Except for NWs of sample A (type 1 droplet), all the investigated NWs have an hexagonal cross section with $\{11\bar{2}0\}$ facets. For NWs with $\{11\bar{2}0\}$ sidewalls the conditions for the TPB nucleation are not satisfied for a Ga molar fraction of 0.60.*

It can be concluded that the calculated minimum Ga molar fraction of the type 2 droplets is a reasonable value as threshold concentration. The nucleation regime changes and the nucleation of ZB nuclei is more probable.
In this analysis the effect of the As-pressure on the growth process was not considered. As stated in [47] for the Ga-assisted growth method, a value of the As pressure of $3.47 \cdot 10^{-7}\, mBar$ $\left(2.6 \cdot 10^{-7}\, Torr\right)$ favors the formation of WZ NWs, a value of $3.47 \cdot 10^{-6}\, mBar$ $\left(2.6 \cdot 10^{-6}\, Torr\right)$ favors the formation of ZB NWs. An influence of the As pressure on the surface reconstruction is the given explanation for this effect. The NWs investigated in this work were grown with an arsenic flux in the range $1.61-2.76 \cdot 10^{-6} mBar$ $\left(1.21 - 2.07 \cdot 10^{-6}\, Torr\right)$. Considering the results of [47], the expected crystal structure for NWs with a type 2 droplet is ZB.
Our results are therefore also in agreement with experimental observations of other groups on Ga-assisted NWs, reinforcing the conclusion that ZB segments appear if the growth is a pseudo Ga-assisted growth.
Since the WZ surface energies are not exactly known and the applied method for the determination of the Ga content in the liquid droplet imply a large uncertainty, the character of this analysis remains qualitative. Nevertheless the results presented in this work agree very well with the current accepted thermodynamical model and the experimental observations of other groups.

A further important aspect of the PIN mechanism is the stability of the thermodynamical state of the droplet. This parameter influences the SF density. The low cohesive energy difference, $\Delta_c = 24\, meV$ per III-V pair [98], between ZB and WZ structure is the reason indicated for the occurrence of stacking faults in the growth sequence.
In a non steady state growth condition, as it occurs for droplets with increasing or decreasing Ga concentration, the occurrence of high density SFs regions in NWs otherwise SF free or with a low SF density can be explained taking into account the changes of the droplet surface energy. If the surface energy of a droplet varies and is close to the value were $\Delta\gamma = 0$, indicating that a change of the nucleation conditions can occur, a discontinuity of the adatoms flux can cause a fluctuation of the thermodynamical state and a high density SFs region can be formed.

In order to quantitatively predict NW characteristics the influence of the supersaturation, and consequently of the gallium concentration on the NWs crystal properties has to be further investigated [138]. The presented results and the proposed investigation method are intended to be a first step in this direction, and can be used as a basis for following research which intend to understand NW specific details of the PIN growth mechanism.

6.5 Summary

In conclusion it was demonstrated that the understanding of the correlation between macroscopic growth parameters and the crystal structure adopted by the NWs is possible only considering the local NW specific growth conditions. The thermodynamical state of the catalyst, together with the surface reconstruction of the NW sidewalls, represent in the PIN growth method the parameters that mainly influence the crystal structure. The supersaturation and therefore the concentration of the elements in the droplet, is the parameter which should be tuned for controlling the nucleation process and the adopted crystal structure.
The TEM analysis of NWs was employed to obtain an estimation of the Ga concentration in the liquid droplets and to relate it to the adopted crystal structure. Thus it was possible to

distinguish between two different classes of droplets, type 1 and type 2 and to relate them to the presence of ZB segments in the NWs.
The two types of particles are representative of two different growth methods: an Au-assisted and a pseudo Ga-assisted growth method.

7 Core/shell heterostructures: crystal structure and morphology

As a core/shell approach is chosen for the realization of ferromagnetic NW heterostructures, the results of the previous chapter are also relevant for the analysis of the (Ga,Mn)As shell properties.
(Ga,Mn)As is usually deposited as a layer on GaAs (001) substrates and the realization of a (Ga,Mn)As shell on a 1D nanostructure is realized for the first time. The structural and compositional characterization of the core/shell NWs plays therefore a major role in the final optimization of the growth process.
Analytical and standard HRTEM techniques are used for the investigations.
The chapter starts answering the question if the low temperature radial growth of (Ga,Mn)As is epitaxial and continues analyzing details of the NW morphology. In order to describe the observed NW morphology thermodynamical and kinetic aspects of the low temperature radial growth are discussed.
Closely related to the radial growth is the presence of regions with different Mn concentrations in the shell which were analyzed by EDS measurements.

7.1 Epitaxial growth and crystal structure

In table 7.1 the growth parameter of the investigated samples are listed.
Sample A is the reference sample for the core NW growth and coincides with sample A of the previous chapter. For sample B optimized shell growth conditions are used. The optimization of the MBE growth parameters was done by A. Rudolph verifying the shell homogeneity by SEM analysis. Sample B NWs are the reference NWs for the (Ga,Mn)As shell growth.
The shell of sample C is realized at a higher temperature if compared to sample B. As known for the MBE growth of (Ga,Mn)As layers, a change in the growth temperature requires the adjustment of the As_4 flux in order to prevent the formation of Mn agglomerates and to obtain comparable uniformity of the layers. For this reason for sample C an enhanced As_4 flux is used for the radial growth of (Ga,Mn)As.
In figure 7.1 side view SEM micrographs of sample B are shown. Two main observations can be made: a) the NWs possess an inversely tapered shape as can be seen in the right micrograph b) NWs which are higher than approximately $4\,\mu m$ often show an irregular morphology in their upper part as indicated by arrows.
The occurrence of the inversely tapered shape can be explained in terms of a low growth

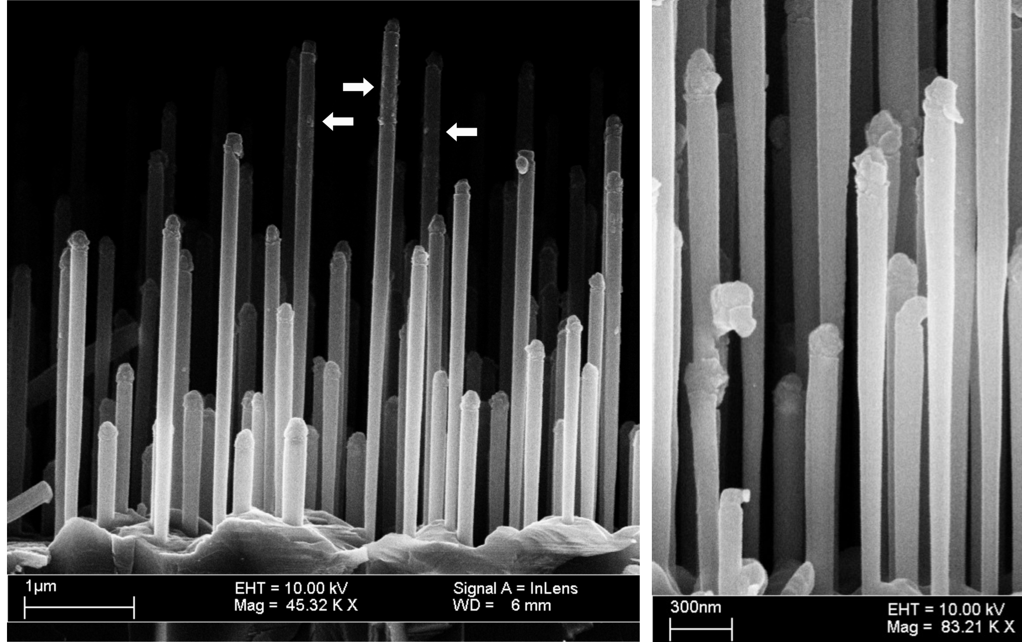

Figure 7.1: ***SEM pictures** - Left, overview of GaAs/(Ga,Mn)As core/shell NWs of sample B. The shell morphology is smooth for the majority of NWs. The arrows indicate the position on the higher NWs were an irregular morphology can be found. Right, the profile of the shell is inversely tapered due to the low temperature growth which reduces the adatom diffusion. A shadow effect due to a 30° inclination of the incoming molecular beam is observed. It can be seen that the part of the NWs near the droplet is larger than the part near the substrate. The SEM analysis is performed by A. Rudolph.*

temperature, 205 $°C$, which reduces the adatom diffusion length, and of a shadow effect. The latter occurs due to the high density of NWs and to the inclination of 30° degree of the molecular beam in respect to the NW axis.
TEM investigations should characterize the existing relation between the crystal structures of core and shell and clarify the reason of the observed shell inhomogeneities.

Cross sections of sample B NWs allow the investigation of the core/shell interface. The epitaxial relationship of the two crystals is revealed by a HRTEM micrograph in figure 7.2.

Sample	As_4 flux $[10^{-6} mbar]$ $(Torr)$	Ga rate [nm/s]	Temp. [°C]	As_4 flux $[10^{-6} mbar]$ $(Torr)$	Ga rate [nm/s]	Temp. [°C]
	Core			**Shell Mn content 5% (nominal)**		
(A) C081212B	1.71 (1.28)	0.038	534			
(B) C081204B	1.69 (1.27)	0.039	533	0.80 (0.60)	0.039	205
(C) C081120A	1.61 (1.21)	0.038	537	1.61 (1.21)	0.038	239

*Table 7.1: **Growth parameters** - Sample (A) is the reference for core axial growth, sample (B) is the reference for the growth of a smooth shell, sample (C) was realized using a higher growth temperature for the shell deposition if compared to the reference.*

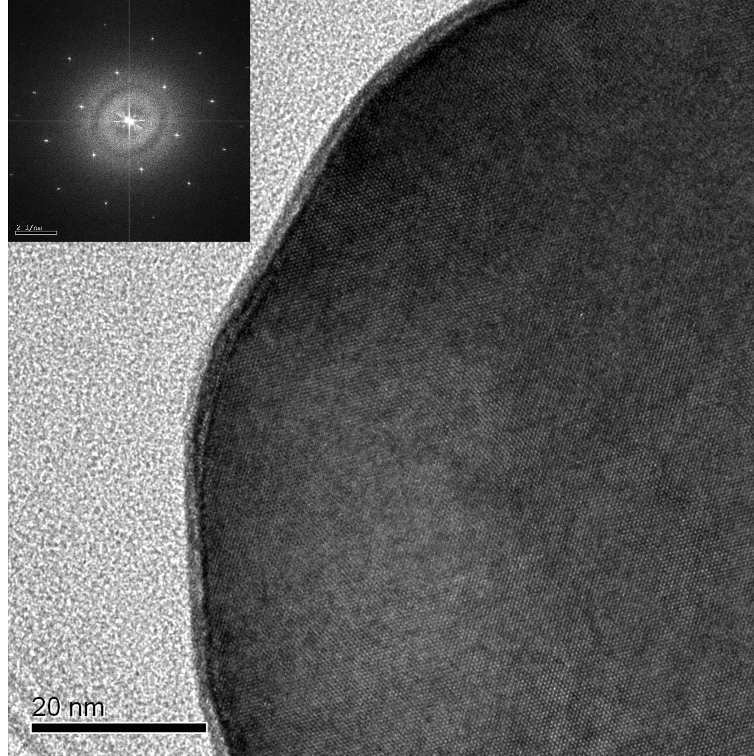

Figure 7.2: ***Epitaxial relationship*** - *HRTEM micrograph of core/shell GaAs/(Ga,Mn)As NW cross section. No interface can be recognized between the core and shell suggesting that the adopted crystal structure is the same for both. Inset, FFT of the left HRTEM micrograph. The periodic arrangement of the crystal does not change between core and shell. In a plane perpendicular to the NW axis the atomic arrangement does not change.*

No interface is recognizable between the GaAs core and the (Ga,Mn)As shell and therefore can be concluded that the radial growth gives rise to single crystal NWs. Only one pattern is recognizable in the FFT shown in the inset, confirming the absence of a change in the atomic arrangement in the plane perpendicular to the growth direction.
The adopted crystal structure is wurtzite (WZ) for both the core and the shell. This is demonstrated in figure 7.3 by a side view bright field micrograph and by the related diffraction pattern. The first shows the absence of scattering contrast at the supposed core/shell interface confirming the epitaxial growth of the shell, the second shows the WZ $(11\bar{2}0)$ diffraction pattern as taken by illuminating contemporary the core and the shell.
This result agree with the investigations on sample A, shown in chapter 6. Only the WZ crystal structure was detected.
Low temperature radial growth develops therefore shells which reproduce the atomic arrangement of the core. This holds also for Stacking Faults (SFs). The scattering contrast of a SF is marked in figure 7.3 by an arrow. The contrast does not stop at the supposed core/shell interface but propagates to the shell. Not only the crystal structure but also the changes in the stacking sequence of the core are reproduced by the shell.
It can be concluded that the radial low temperature growth is an epitaxial growth and that the quality of the shell crystal is determined by the quality of the core crystal.
The parameter characterizing the quality of a NW crystal is the SF density. In general this is not constant along the core NW axis because of its dependence on the variation of the

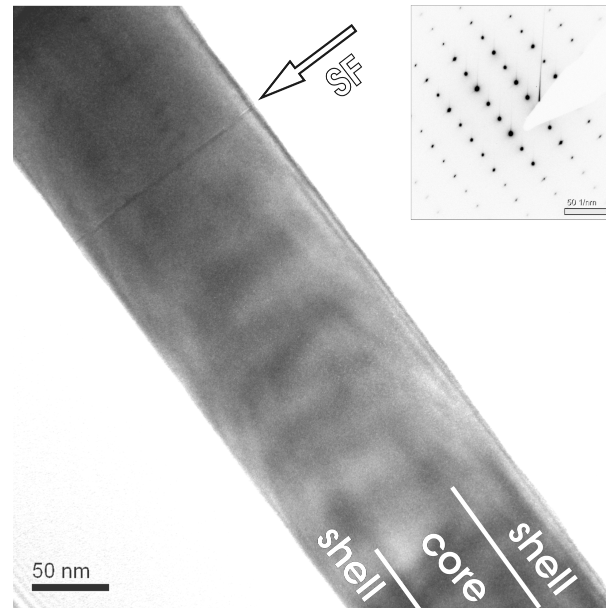

Figure 7.3: ***Wurtzite crystal structure*** - *Bright field side view micrograph of a core/shell GaAs/(Ga,Mn)As NW. No scattering contrast is observed at the supposed core/shell interface, confirming the epitaxial growth of the shell. Inset, diffraction pattern of the NW showing a* $(11\bar{2}0)$ *oriented wurtzite crystal. The arrow indicates the scattering contrast of a SF propagating from the core to the shell.*

Ga concentration in the droplet during the axial growth. For the characterization of NWs according to their SF density, the entire growth history of single NWs should be considered. This method is applied for the analysis of the irregular morphology of NW segments shown in figure 7.1.

The bright field micrograph in figure 7.4 shows that the irregular morphology is associated with the presence of a high SF density in the crystal. The lines oriented perpendicular to the NW axis are equally distributed along the entire segment. It is also evident that the shell is no longer smooth but becomes irregular and clusters appears.
This features correlate to the properties of the underlying core NW. This is revealed by the analysis carried on 7 core NWs of reference sample A and 10 core/shell NWs of sample B. The crystal quality of the investigated NW segments can be divided in two types:

- NW segments with a low density of SFs
- NW segments with a high density of SFs (see figure 7.5).

The definition of high density is empirical: a NW segment is considered to have a high density of SFs when the diffraction pattern of the segment cannot be ascribed to one of the two adopted crystal structures, as shown in figure 5.9 c).
The occurrence of a high density SF segment in a NW is generally not predictable. The investigations however showed that for sample A and B core NWs a reoccurring pattern can be identified: NWs with a diameter smaller than ca. $80\,nm$ show high density SF segments in their upper part below the droplet in an otherwise nearly perfect wurtzite crystal; NWs with a diameter larger than ca. $80\,nm$ show a nearly perfect wurtzite crystal.
The parameters used for growing the core NWs of samples A and B produce a stable droplet state, which results in a high quality crystal structure for all NWs. This can be deduced

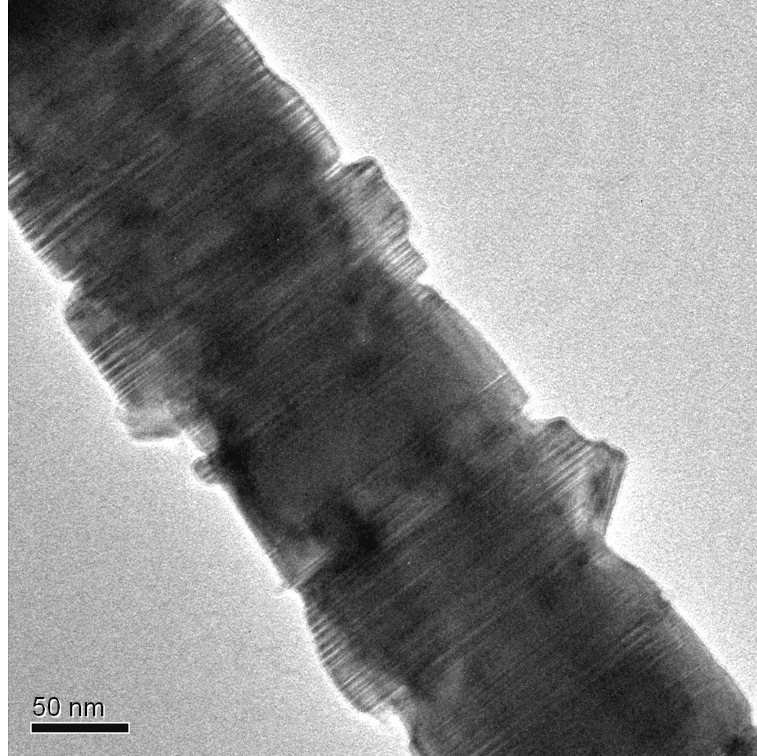

Figure 7.4: ***Stacking faults and radial growth*** - *Bright field TEM micrograph of a NW segment similar to the NW segments indicated in figure 7.1 by arrows. The clusters that gives rise to the irregular shell morphology are characterized by a high density of SFs, identified by the lines perpendicular to the NW axis.*

from the analysis presented in chapter 6 and is due to the low probability to have oscillations in the droplet composition during growth for NWs with an aspect ratio tending to zero.
As can be seen in figure 6.6, only core NWs showing a diameter smaller than $70-80\,nm$ have an aspect ratio greater than zero. Due to the $1/d^2$ proportionality between NW height and NW diameter d, these represent the highest grown NWs.
At the top of figure 7.5 an example of this type of NW is shown. At the bottom of figure 7.5 a NW with an aspect ratio tending to zero is shown.
For core NWs with a diameter smaller than $70-80\,nm$, the explanation of the occurrence of the high SF density segments only in the final part of the growth lies in the fact that once a NW emerges over the NWs ensemble, it can collect more gallium on its sidewalls due to a higher direct impinging rate. This causes a higher Ga flux towards the droplet and induces a thermodynamical state that favors center nucleation. This process develops a faulty segment.
The presence of clusters in the (Ga,Mn)As shell of the highest NWs can be therefore associated to the presence of a high SF density segment in the core NWs

In conclusion, the low temperature radial growth of (Ga,Mn)As shells is epitaxial and the occurrence of poor shell crystal quality can be explained in terms of poor crystal quality of the core.

Figure 7.5: ***Stacking fault density*** *- Top, bright field micrograph of a NW with an aspect ratio > 0.3 and a high SF density in the last grown µm. This features are typical for NWs higher than ca. 4 µm and with a diameter < 80 nm. A stable droplet state during growth is most probable for larger NWs and induces a low SF density in the NW crystal. Bottom, bright field TEM micrograph of a NW with an aspect ratio of 0 and a low SF density. This features are typical for NWs lower than 1 µm and with a diameter > 80 nm.*

Radial growth on faulty sidewalls

In order to investigate the mechanism inducing the cluster formation in the shell, a sample with a growth temperature of the shell of 239 °C is investigated (sample C). The intention is

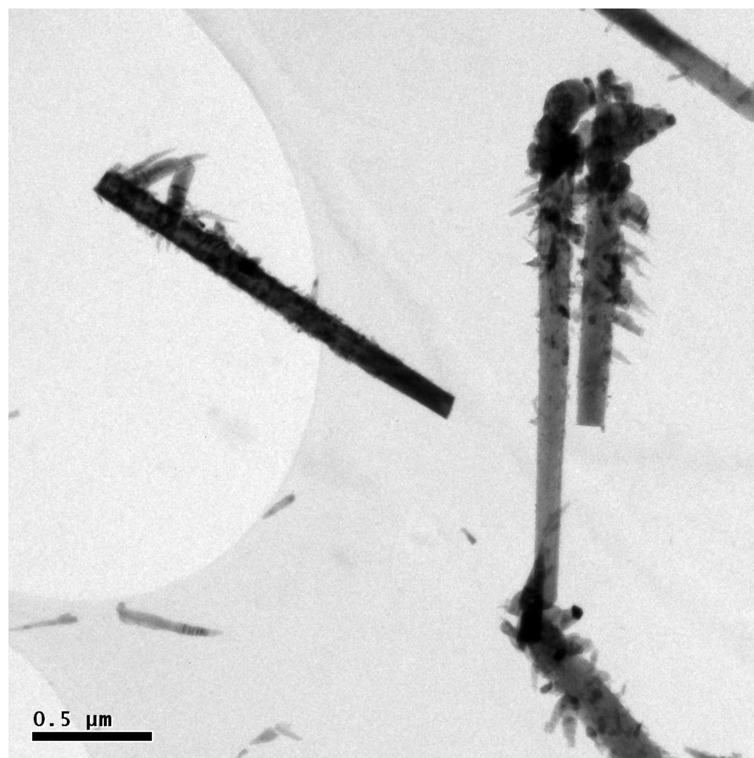

Figure 7.6: ***Induced cluster formation*** *- Bright field micrograph showing a side view of sample C NWs. The clusters extends laterally for hundreds of nanometer appearing as ramifications. The density of the laterally grown material is increased compared to that of clusters of sample B NWs.*

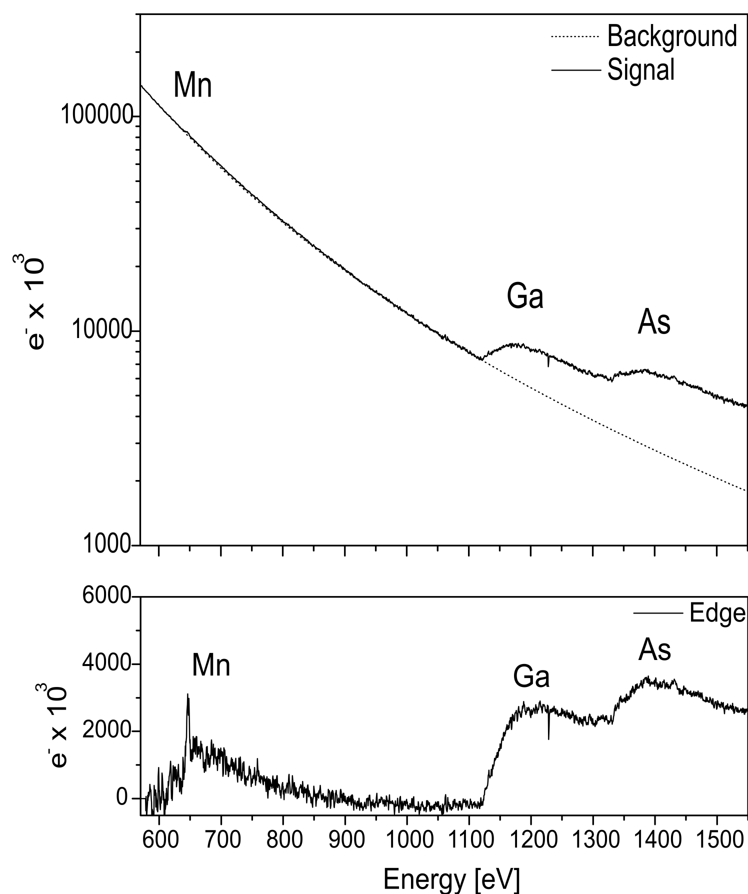

Figure 7.7: ***EELS spectrum of a laterally grown cluster*** *- Top, EELS spectrum acquired on a laterally grown cluster showing the presence of a Ga and an As peak (logarithmic scale). Bottom, Only after the background subtraction the Mn peak is also recognizable (linear scale).*

to verify if the formation of clusters is a temperature driven effect and if a phase segregation process occurs. In (Ga,Mn)As layers the latter induces the formation of MnAs clusters [116]. The bright field micrograph in figure 7.6 shows that the lateral extension and the density of the clusters increases with an increasing growth temperature. The EELS elemental analysis of the radial extensions, having the aspect of ramifications, shows the presence of all three elements Ga, Mn and As and is shown in figure 7.7.
It can be therefore excluded that the ramifications are the result of MnAs segregation even if these are induced by a higher temperature growth. Since no gold was found at the tip of the clusters or of the ramifications, also a Au catalyzed lateral growth due to the PIN mechanism can be excluded.
An EDS analysis of a cross section of a sample B NW shows that the laterally grown material composes of Ga, Mn and As. The element maps in figure 7.8 show no difference in the shape of the shell for all three elements. The Mn map demonstrate the presence of Mn in the laterally grown cluster and the absence of Mn in the core. As expected, also for the low temperature shell growth the cluster formation is not associated to phase segregation.

Since a change in the growth temperature influences the adatom diffusion on the core surface

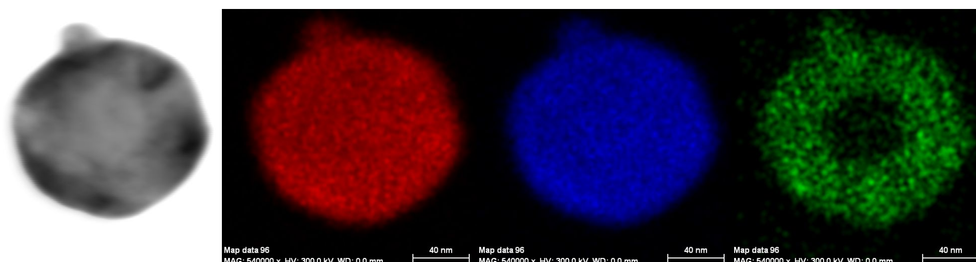

Figure 7.8: ***EDS map of a NW cross section*** *- From left to right: STEM micrograph, EDS As map, EDS Ga map, EDS Mn map of a sample B NW cross section. The element analysis shows that Ga, Mn and As are all present in the laterally grown cluster. Also the core is recognizable in the Mn map. The detected Mn signal in the core represents the noise level of the measure.*

and therefore the growth kinetics, a mechanism relying on an enhanced role of the sticking coefficient of rough surfaces is discussed as a possible cause of cluster formation for sample B NWs and of the arising of ramifications for sample C NWs.
The analysis on the relation between the crystal quality of core and of the shell revealed that the cluster formation is related to a high SF density segment of the underlying core crystal. The HRTEM micrograph in figure 7.9 shows the edge of an hexagonal core NW decorated by SFs. A nanometer sized zig-zag profile can be observed. The zig-zag profile is associated to a local ZB stacking sequence in axial direction. The NW facets of a high SF density region can be therefore regarded to be rough surfaces. Rough surfaces and edges are considered to be preferential positions in the adlayer for the incorporation of adatoms in the crystal because of their higher sticking coefficient in respect to flat surfaces [87]. Considering this and the fact that rough surfaces does not show a defined atomic arrangement, the following observation can be made.
The high temperature radial growth on a high SF density region may occur strongly in the

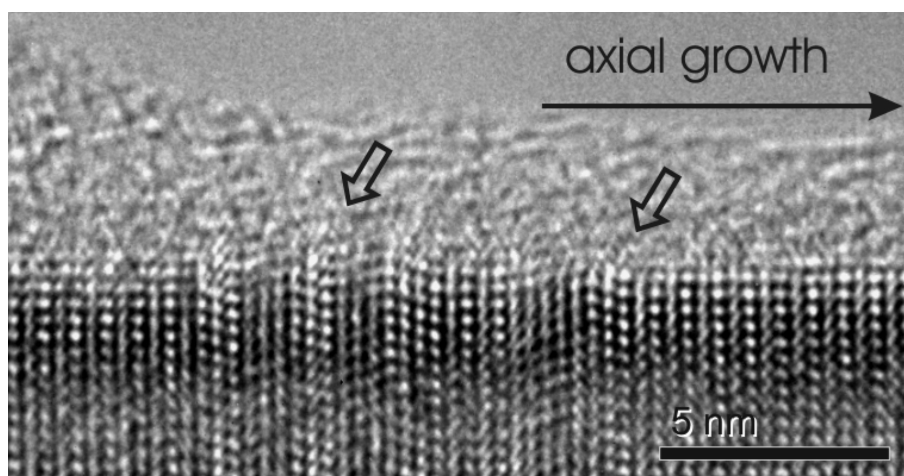

Figure 7.9: ***Rough sidewall surface*** *- HRTEM micrograph of a NW edge. Stacking faults induce a rough profile of the NW edge indicated in the micrograph by arrows. In this case ZB segments are associated to the SFs. The presence of this segments has as a consequence a higher amplitude of the edge roughness. Since a SF extends over the entire NW cross section also the sidewalls can be considered rough. Edges and rough surfaces are considered to be preferential nucleation points due to their higher sticking coefficient.*

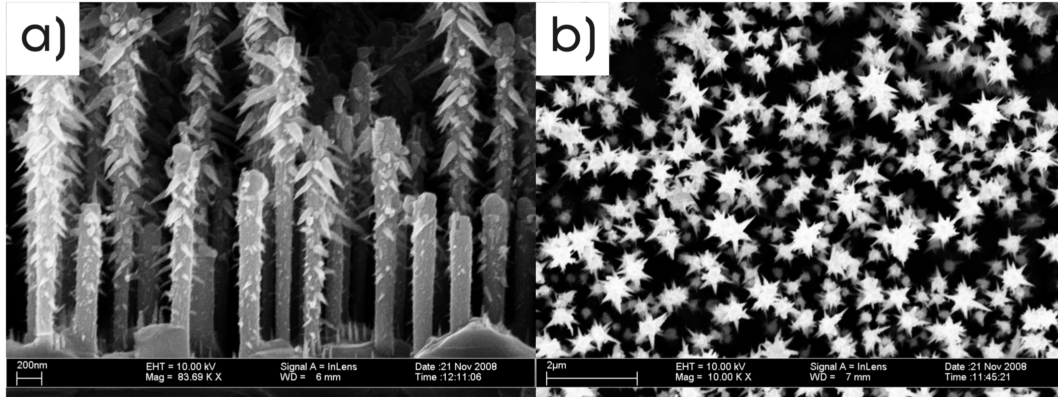

Figure 7.10: ***Induced cluster formation - SEM micrographs*** *- a) side view SEM micrograph of sample C. The growth direction of the ramifications is ordered and suggests a dependence on the crystallographic direction of the NWs crystal b) top view micrograph of sample C. The sixfold symmetry of the crystal in the (111)B plane is recognizable. The SEM analysis was performed by A. Rudolph.*

crystal direction which realizes an arrangement of atoms that minimizes the Gibb´s free energy irrespective of the original WZ crystal structure. It can be regarded as a growth due to a self assembling mechanism without catalytic particle.
Side and top view SEM micrographs of sample C, shown in figure 7.10 a) and b) respectively, supports the proposed mechanism of formation of the radial extensions. A relation of the growth direction of the ramifications to the NW crystal can be deduced. In the side view the ramifications are oriented downwards with the same angle to the NW axis. In the top view a sixfold symmetry reproducing the sixfold symmetry of the crystal is recognizable.
In the temperature range $200 - 240\,^{\circ}C$ the growth on rough surfaces may happen in the crystal direction normal to a closed packed surface. Zinc blende is the considered crystal structure because of the disordered atomic arrangement of rough surfaces and because the zinc blende crystal is energetically favored compared to the wurtzite crystal [98].
For ZB the closed packed directions are the [111]. In particular the set of closed packed planes showing a sixfold symmetry in the (111)B projection is the $\{\bar{1}\bar{1}1\}$. Of those only three planes are oriented congruently to the direction of the ramifications.
The SEM top view micrograph in figure 7.10 b) should therefore show a threefold symmetry of the ramifications. The sixfold symmetry can be explained if one considers that a high SF density region in the core contain twinned ZB segments which have as a consequence the rotation of 60° in the (111)B plane of the miller indices. The presence of twinned segments in the core also explains the downward orientation of the ramifications in respect to the NW axis as shown in the side view micrograph of figure 7.10 a).
The growth of the induced clusters at $239\,^{\circ}C$ can be explained considering a self assembling mechanism driven by the reduction of the work of formation of 2D nuclei on the $\{\bar{1}\bar{1}1\}$ surfaces.
The presented results suggest that the formation of laterally growing clusters in the low temperature radial growth of sample B NWs may rely on the same mechanism and could be ascribed to the presence of high SF segments in the core NWs.

The one presented here is a first phenomenological description of the mechanism of cluster formation and has to be verified and extended by further investigations. It has to be clarified e.g. why in figure 7.10 a) the appearance of the ramifications are equally distributed along the NWs axis, or why the substrate and NWs lower than ca. $1\,\mu m$, which are considered

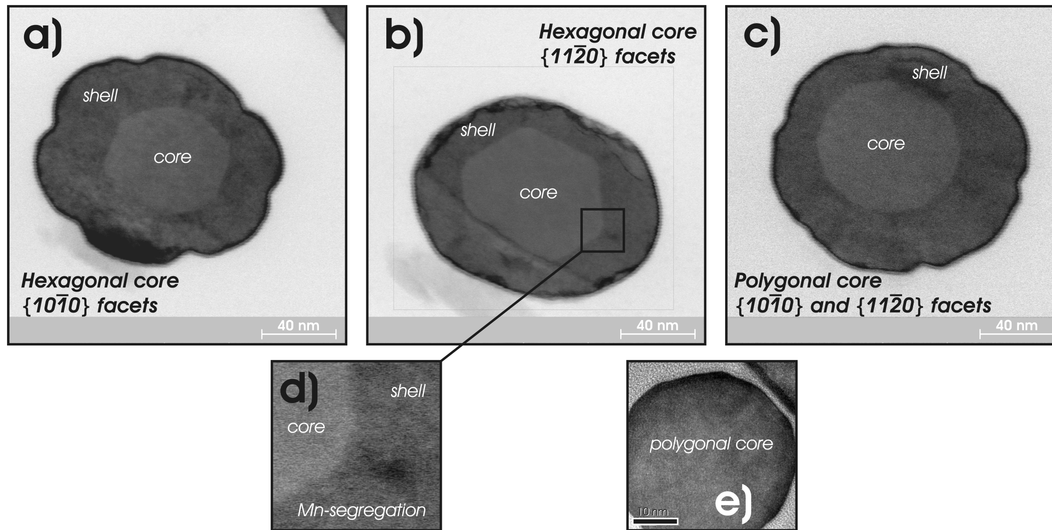

Figure 7.11: ***The three observed shell morphologies*** - *The micrographs on the top of the figure are STEM micrographs showing three GaAs/(Ga,Mn)As core/shell cross sections representative of the three observed shell morphologies of sample B NWs. Due to Mn interstitials the shell appears darker than the core. a) core NWs with* {10$\bar{1}$0} *sidewalls have an anisotropic shell morphology. The sixfold symmetry of the WZ crystal in the* (000$\bar{1}$) *plane is reproduced by the shell shape. b) core NWs with* {11$\bar{2}$0} *sidewalls have a rounded shell without any recognizable crystal symmetry. In correspondence of all corners darker regions can be recognized. One of them is enlarged in the left micrograph at the bottom. As will be demonstrated in subsection 7.3 this contrast arises from Mn segregation. c) core NWs with six* {10$\bar{1}$0} *and six* {11$\bar{2}$0} *sidewalls have a rounded shell showing a sixfold symmetry. e) HRTEM micrograph of a polygonal core NW shows the faceted profile.*

to be nearly SF free, show also ramifications. Furthermore the influence of strain on the nucleation mechanism has to be introduced in order to take into account the difference in lattice constants between the GaAs and the (Ga,Mn)As crystals.

In conclusion the control over the crystal quality of the core NWs, and therefore over the stability of the droplet composition during growth plays a fundamental role in the control of the crystal quality of the shell. High SF density segments in the core NWs limits the temperature range that can be used for growing the (Ga,Mn)As shell because of the appearance of inhomogeneities and lateral growing clusters. A low growth temperature causes the incorporation of a lower amount of Mn ions in the GaAs matrix, reducing the ferromagnetic order in the material and should be avoided [106].
At the present crystal purity is one of the main goals of NW research.

7.2 Cross section morphology

The analysis on cross sections of core/shell NWs segments shows that the shape of the NWs changes after the shell deposition.

In figure 7.11 the three observed types of shell contour are shown. The NWs belongs to the same specimen, prepared by ultramicrotomy. Furthermore the used magnification is the

same for all three micrographs so that rotations due to different values of the TEM lens-current can be excluded. The relative orientation between the depicted NWs corresponds therefore to their relative orientation during growth and the crystallographic directions can be compared.
The two hexagonal core shapes, appearing brighter in the STEM micrographs a) and b), show $\{10\bar{1}0\}$ or $\{11\bar{2}0\}$ lateral facets, as determined by HRTEM measurements. The polygonal shape of the core NW in micrograph c) has six $\{10\bar{1}0\}$ and six $\{11\bar{2}0\}$ oriented sidewalls. The HRTEM micrograph e) show a polygonal core NW were the different sidewall orientations can be recognized.
The appearance of different sidewall orientations and of different crystal shapes in core NWs is not well understood [125]. A qualitative investigation of both samples, A and B, reveals that the polygonal and the $\{11\bar{2}0\}$ hexagonal represents the majority of the core NWs cross sections. The first one is related to NWs with a diameter approximately $> 80\,nm$ and the second one to NWs showing a diameter approximately $< 80nm$. The $\{10\bar{1}0\}$ hexagonal cross sections are only a few percent and are related to NWs with a diameter of about $60\,nm$.
During axial growth the specific surface energy of the facets enters the energetic balance at the triple phase boundary [33]. The thermodynamical state of the liquid droplet and its dimensions determine, for given growth conditions, the energetically favored surfaces and therefore the shape of the core NWs. The high variability of the state of the liquid droplet together with the possibility to generate ZB or WZ crystals makes the prediction of the NW shape difficult.

In figure 7.11 the shell appears darker if compared to the core due to the presence of Mn interstitials. Sitting in the crystal at a position in between lattice points, Mn interstitials produce a diffuse background in the diffraction pattern superimposed to the bright spots of the reciprocal lattice. Each pixel of the STEM images of figure 7.11 shows a brightness proportional to the current generated in the STEM detector by the electrons contained in the (000) spot. The electrons responsible for the diffuse background are automatically filtered out because of their larger scattering angle. The (Ga,Mn)As shell appears therefore dark. This mechanism is also enhanced by the relative large thickness, ca. $200\,nm$, of the NW cut, due to multiple scattering events.
The dark stripes, which extend radially from the edges of the core $\{11\bar{2}0\}$ NW of figure 7.11, enlarged in micrograph d), are supposed to be caused by Mn segregation. EDS measurements on different positions of the shell will be presented in subsection 7.3.

From micrographs a) and c) in figure 7.11 two components of the shell thickness anisotropy can be deduced. The first one is the fast changing shell thickness reproducing the sixfold symmetry of the wurtzite crystal structure in the $(000\bar{1})$ plane, the second one creates a low changing modulation of the shell thickness and is related to the shadow effect produced by adjacent NWs. The following discussion will focus on the first type of shell irregularities.

Thermodynamical and kinetic considerations

To the knowledge of the author there is no published model that describes the morphological evolution of shell growth analyzing its dependence on the shape of the core and on the temperature. The following considerations are based on results and concepts expressed in different publications and in the theory of crystal growth and have the intention to deduce characteristics of the investigated NWs which may play an important role in the

morphological evolution of the shell [87, 124, 139-147].

The relevant characteristics of the shell morphologies can be summarized as follows:

- core NWs with $\{10\bar{1}0\}$ sidewalls shows a large radial growth rate difference between the $<10\bar{1}0>$ and $<11\bar{2}0>$ directions. If present, segregation effects are not clearly detectable,
- core NWs with $\{11\bar{2}0\}$ sidewalls develop a rounded shell and show segregation effects appearing as stripes,
- core NWs with six $\{10\bar{1}0\}$ and six $\{11\bar{2}0\}$ sidewalls develop a more complex profile also characterized by different growth rates in the $<10\bar{1}0>$ and $<11\bar{2}0>$ directions. If present, segregation effects are not clearly detectable.

The shell morphologies that can be found in the literature in contrast are hexagonal, with facets having the lowest surface energy, irrespective of the original shape or facet orientation of the core. As an example AlInP shells grown on GaAs core NWs show $\{1\bar{1}0\}$ oriented zinc blende facets even if the core facets belong to the $\{11\bar{2}\}$ family. The occurrence of a rotation of the sidewalls orientation is not material specific [143, 144].
Beyond the material used, the main difference between the radial growth of the (Ga,Mn)As shells investigated in this work and the shells investigated by other groups consists in a different growth temperature. The shells that can be found in the literature were grown in the temperature range $400 - 500\,^{\circ}C$ [143, 144]. Differently from the NWs investigated in this work, tapering in axial direction induced by radial growth is not observed in [144]. From this follows that a radial growth temperature of $205\,^{\circ}C$ reduces the diffusion constants inducing a lowered efficiency of material transport that affects the shell morphology.
Furthermore if high temperatures are used for the radial growth, NWs with an equilibrium crystal shape are developed [143, 144]. The latter is defined as *...the shape at which the crystal has a minimal surface energy at a given constant volume* [87]. Due to the 1D character of NWs, the equilibrium crystal shape which is meant here is the profile of the cross section normal to the $<000\bar{1}>$ wurtzite direction of the 3D equilibrium shape. The specific surface energies of the (Ga,Mn)As wurtzite crystal are unknown and therefore the equilibrium crystal shape cannot be calculated. However the observed shell morphologies in figure 7.11 a) and c) does not realize an equilibrium crystal shape because of the presence of concave regions, which are not allowed in an equilibrium shape [87]. It can be therefore concluded that a global minimization of the surface energy does not take place during low temperature radial growth and that kinetic hindrances, like e.g. potential barrier present at atomic steps, may play a major role in the determination of the morphological evolution of the shell.
For GaAs core wurtzite NWs the specific surface energies obey the inequality

$$\gamma_{\{10\bar{1}0\}} < \gamma_{\{11\bar{2}0\}} \tag{7.9}$$

[137]. Of the three core NWs of figure 7.11, appearing brighter than the shell, only the NW in figure 7.11 a) shows an equilibrium crystal shape as can be deduced from [137]. It follows that only for $\{10\bar{1}0\}$-core NWs the chemical potential is the same on every point of the surface and that $\{11\bar{2}0\}$-core and polygonal core NWs exhibit different values of the chemical potential on their surface [87]. As a consequence, since a gradient in the chemical potential induces an adatom diffusion flux, only the growth on $\{11\bar{2}0\}$-core and polygonal core NWs is potentially affected in its initial phase by an adatom diffusion flux [87].

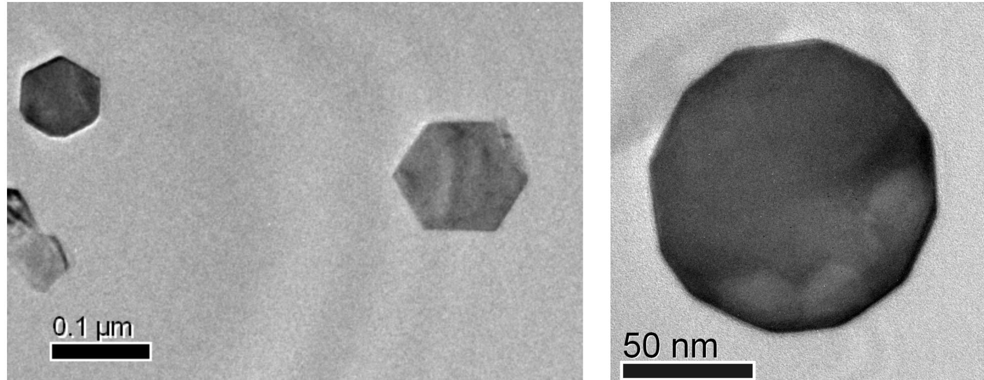

Figure 7.12: ***Morphological stability*** *- Bright field micrographs of GaAs/GaAs core/shell NWs cross sections. The shell growth temperature was 332 °C. All three core profiles observed for sample B NWs are found. Irregular shell morphologies are not found. The equilibrium between 2D nucleation rate and rate of advance of a step can be an explanation of the conservation of the original core shape.*

The conclusion that can be drawn from these considerations is that the morphology of core/shell NWs is most probably determined by the effects of potential barriers limiting the kinetics of diffusion processes. For a low temperature radial growth, kinetic barriers play a major role and morphological instability of the NW shape is the consequence [139, 140, 141, 145].
It can be figured that an intermediate temperature exist between that used for growing the (Ga,Mn)As shell, $T = 205\,^{\circ}C$, and the high value used in the published work of other groups at which morphological stability occurs and the shell exhibit the same cross section of the core because of an enhanced surface diffusion constant.
Bright field micrographs of a GaAs/GaAs core/shell sample grown at $T = 332\,^{\circ}C$ are shown in figure 7.12. The amount of deposited material, equivalent to a layer thickness of $200nm$, is the same as for the investigated GaAs/(Ga,Mn)As core/shell sample. Despite the deposition of the GaAs shell the three core shapes observed for sample B are present. A further increase of the temperature is expected to develop hexagonal shapes with lowest specific surface energy facets, irrespective of the initial shape of the core.

7.3 Mn segregation

Core NWs with $\{11\bar{2}0\}$ facets develop a round shell like that shown in figure 7.13 a). A characteristic feature of this type of shell is the presence of dark stripes extending radially and starting at the corner of the core. A local increase in Mn concentration is supposed to generate the observed contrast. In figure 7.13 a) these stripes are indicated by arrows.
The increased Mn content is proved by EDS measurements. An electron probe with a diameter $< 5nm$ and a counting time of about $10sec$ was used for the measures. Furthermore the specimen was cooled at liquid nitrogen temperature in order to reduce the carbon contamination on its surface. A small electron probe and a short counting time are fundamental for achieving a high spatial resolution which permits to resolve the difference in Mn content in the stripe. The acquisition time is the maximum time that guarantees drift-free measures.
The spectra shown in figure 7.13 c) represent the sum of 18 different measurements performed on the radial stripes and on the material between the stripes. The position of the measurements on the shell are sketched in figure 7.13 b).

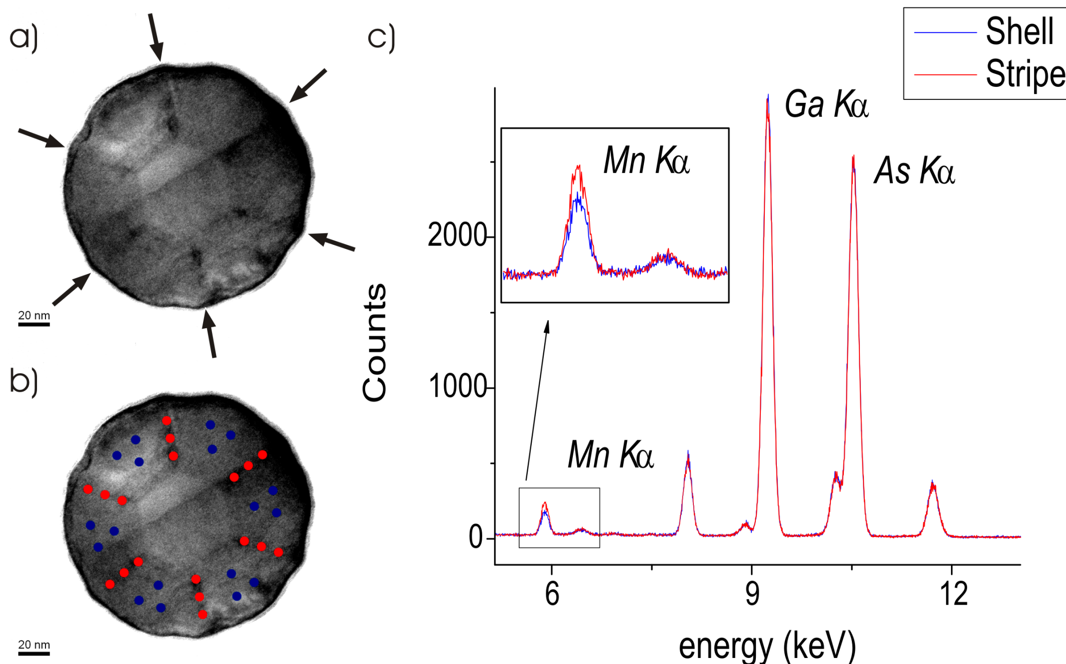

Figure 7.13: ***EDS measurements on the radial stripes** - a) bright field micrograph of a {11$\bar{2}$0}-NW cross section. The dark stripes present in correspondence of the core NW corners are indicated by arrows. b) Sketch of the EDS measurements positions on the shell, blue dots, and on the stripes, red dots. c) EDS spectra of the shell and of the stripe. Each spectrum is the sum of the 18 different measurements. The Mn peak is enlarged in the inset. A difference in the peak height demonstrates that the dark stripes are the result of a Mn segregation effect.*

In order to evaluate the Mn concentration two observations should be taken into account. The first is that an absolute value of the Mn concentration cannot be calculated due to the missing Cliff-Lorimer factors (see section 5.4). The second is that the Ga content in the shell should varies with the Mn concentration due to the substitutional character of part of the Mn ions present in the crystal [106]. For this reasons the Mn/As peak ratio is chosen as relevant quantity for comparing the Mn contents of different shell regions. The determination of the peak height was done according to the method explained in chapter 5.4 and consists in considering the $K\alpha$ line for each element and evaluating the peak height of a fitting Gaussian curve. The error affecting the value of the peak height is considered to be the mean value of the residuals of the 12 points on the curve adjacent to the peak maximum and corresponding to an energy range of ca. $50\,eV$ centered around the maximum.
The Mn/As peak ratio results significant higher for the spectrum acquired on the radial stripes than for that acquired on the remaining part of the shell, indicating an increased Mn content in the stripes. The quantified peak ratios are shown in table 7.2 also for the core.
The propagated error of the Mn/As ratio has a relative value of about 10%. The poor sensitivity has to be ascribed to the used small electron-probe and the short counting time. The product of the electron-probe current and the counting time determines the mean value of the counts and therefore, assuming a Poisson statistic, the variance of the measure.
Despite the high error the result lead to the conclusion that Mn segregation occurs during radial growth at the corners of the {11$\bar{2}$0}-core NWs.
In presence of an induced diffusion flux, segregation effects are explained by Sköld et al. as a consequence of different surface diffusion constants of the elements constituting the semi-

	Ga/As peak count ratio	**Mn/As** peak count ratio $[\times 10^{-2}]$
core	1.23 ± 0.07	
shell	1.17 ± 0.06	7.06 ± 0.88
stripe	1.15 ± 0.08	9.54 ± 1.20

Table 7.2: ***EDS peaks count ratios*** *- Sample B GaAs/(Ga,Mn)As cross sections EDS data are reported. The measured regions are sketched in figure 7.13.*

conductor AlInP [143]. If this is the case also for (Ga,Mn)As, implying $D_{s(Ga)} > D_{s(Mn)}$, depends on the presence of an induced diffusion flux during growth. Its presence for $\{11\bar{2}0\}$-core NWs was deduced by the analysis on the equilibrium crystal shape presented above but has to be verified by further experiments.

7.4 Summary

In conclusion it was demonstrated that the low temperature radial growth of (Ga,Mn)As on GaAs core NWs is epitaxial and that the obtainable crystal quality strongly depends on the SFs density of the core NWs. As a consequence the shell morphology of (Ga,Mn)As grown on faulty and on perfect crystal segments was investigated. With the aid of analytical TEM techniques and SEM analysis it was demonstrated that the cluster formation in correspondence of faulty segments is not a MnAs segregation related effect. It could be interpreted as a consequence of the minimization of the Gibb´s free energy during radial growth.
The analysis of the morphology of GaAs/(Ga,Mn)As cross sections revealed a change of the NW shape between core and shell. The observed shell shapes are most probable the result of the prevailing of kinetic limiting effects over thermodynamically driven diffusion effects. An increased Mn content was detected by EDS measurements on the stripes present in the shell of a NW with a $\{11\bar{2}0\}$-core. The origin of this segregation effect is supposed to be an induced surface diffusion during growth but has to be verified by further experiments.

8 Summary

The question of a structural and morphological characterization of GaAs based nanowires was the research interest of this thesis. For this purpose standard and analytical transmission electron microscopy techniques were employed. As first TEM thesis of the University of Regensburg on this topic adequate specimen preparation and investigation methodologies were introduced in order to obtain a reliable interpretation of the results.
The principal achievement on developing a new investigation method was the necessity to relate the results of crystal structure and morphology characterizations to microscopic and NW-specific parameters and not to macroscopic and general growth parameters. This allows a reliable comparison of NW characteristics and enhances the comprehension of their growth mechanism.
The analysis of the results on crystal structure investigations, assuming this new perspective, delivered the fundamental finding that the axial growth of Au-assisted GaAs NWs can change in a pseudo Ga-assisted growth due to a non steady-state regime of the Ga accumulation process in the liquid droplet.
The attempt to associate the observed crystal structures to one of these two growth modes revealed that zinc blende segments are most probably generated when a pseudo Ga-assisted growth occurs. This experimental evidence is in accordance with investigations developed by Glas et al. and Spirkoska et al. and with the current understanding of the NW growth mechanism and unifies the interpretation of catalytic growth of GaAs NWs.
The Mn doped GaAs shell deposited at low temperature on core GaAs NWs was characterized for the first time. The growth was found to be epitaxial and to confer the quality of the core crystal to the shell crystal. As a consequence a high stacking fault density of the core NW limits the temperature of the shell growth due to the formation of clusters.
Cross sections of (Ga,Mn)As shells grown on stacking faults free core NWs was investigated. Simple kinetic and thermodynamical considerations leaded to the conclusion of morphological instability of the low temperature radial growth. Analytical measurements on a shell cross section revealed the presence of Mn segregation effects and suggested, as a first interpretation, a higher diffusion coefficient on the (Ga,Mn)As wurtzite surfaces for Ga than for Mn adatoms.

Bibliography

[1] K. A. Dick, *A review of nanowire growth promoted by alloys and non-alloying elements with emphasis on Au-assisted III–V nanowires*, Progress in Crystal Growth and Characterization of Materials 54, 138 (2008).

[2] H. Sakaki, *Scattering Suppression and High-Mobility Effect of Size-Quantized Electrons in Ultrafine Semiconductor Wire Structures*, Jap. J. Appl. Phys. 19, L735 (1980).

[3] L. Huang, D. Li, P. Chang, S. Chu, H. Bozler, I. S. Beloborodov, J. G. Lu, *Quantum transport in indium nitride nanowires*, Phys. Rev. B 83, 245310 (2011).

[4] C. A. Dartora, G. G. Cabrera, *Quantum transport in a ferromagnetic nanowire: conductance and MR effect*, Physics Letters A 334, 46-54 (2005).

[5] C. Weisbuch, B. Vinter, *Quantum Semiconductor Structures: Fundamentals and Applications*, Academic Press, Boston (1991).

[6] H. Pan, Y. P. Feng, *Semiconductor Nanowires and Nanotubes: Effects of Size and Surface-to-Volume Ratio*, ACS Nano 2, 2410-2414 (2008).

[7] B. Tian1, X. Zheng, T. J. Kempa, Y. Fang, N. Yu, G. Yu, J. Huang, C. M. Lieber, *Coaxial silicon nanowires as solar cells and nanoelectronic power sources*, Nature 449, 885-889 (2007).

[8] O. Hayden , R. Agarwal, C. M. Lieber, *Nanoscale avalanche photodiodes for highly sensitive and spatially resolved photon detection*, Nature Materials 5, 352-356 (2006).

[9] Z. M. Liaoa, H. Z. Zhangb, Y. B. Zhoua, J. Xua, J. M. Zhanga, D. P. Yu, *Surface effects on photoluminescence of single ZnO nanowires*, Physics Letters A 372, 4505-4509 (2008).

[10] J. X. Wang, D. F. Liu, X. Q. Yan, H. J. Yuan, L. J. Ci, Z. P. Zhou, Y. Gao, L. Song, L. F. Liu, W. Y. Zhou, G. Wang, S. S. Xie, *Growth of SnO_2 nanowires with uniform branched structures*, Solid State Communications 130, 89-94 (2004).

[11] X. J., B. Tiana, J. Xianga, F. Qiana, G. Zhenga, H. Wangb, L. Maia, C. M. Liebera, *Rational growth of branched nanowire heterostructures with synthetically encoded properties and function*, www.pnas.org/cgi/doi/10.1073/pnas.1108584108.

[12] P. Krogstrup, J. Yamasaki, C. B. Sørensen, E. Johnson, J. B. Wagner, R. Pennington, M. Aagesen, N. Tanaka, J. Nygård, *Junctions in Axial III–V Heterostructure Nanowires Obtained via an Interchange of Group III Elements*, Nano Lett. 9, 3689-3693 (2009).

[13] D. M. Cornet, R. R. LaPierre, *InGaAs/InP core–shell and axial heterostructure nanowires*, Nanotechnology 18, 385305 (2007).

[14] R. S. Wagner and W. C. Ellis, *Vapor-Liquid-Solid Mechanism of Single Crystal Growth*, Appl. Phys. Lett. 4, 89 (1964).

[15] M. Yazawa, M. Koguchi, K. Hiruma, *Heteroepitaxial ultrafine wire-like growth of InAs on GaAs substrates*, Appl. Phys. Lett. 58, 1080 (1991).

[16] K. Haraguchi, T. Katsuyama, K. Hiruma, K. Ogawa, *GaAs p-n junction formed in quantum wire crystals*, Appl. Phys. Lett. 60, 745 (1992).

[17] Y. Li, F. Qian, J. Xiang, C. M. Lieber, *Nanowire electronic and optoelectronic devices*, Materials Today 9, 18-27 (2006).

[18] E. Tutuc, J. Appenzeller, M. C. Reuter, S. Guha, *Realization of a Linear Germanium Nanowire p−n Junction*, Nano Lett. 6, 2070-2074 (2006).

[19] H. Y. Cha, H. Wu, Mvs. Chandrashekhar, Y. C. Choi, S. Chae, G. Koley, M. G. Spencer, *Fabrication and characterization of pre-aligned gallium nitride nanowire field-effect transistors*, Nanotechnology 17, 1264 (2006).

[20] S. A. Dayeh, D. P. R. Aplin, X. Zhou, P. K. L. Yu, E. T. Yu, D. Wang, *High Electron Mobility InAs Nanowire Field-Effect Transistor*s, Small 3, 326-332 (2007).

[21] J. Goldberger, A. I. Hochbaum, R. Fan, P. Yang, *Silicon Vertically Integrated Nanowire Field Effect Transistors*, Nano Lett. 6, 973-977 (2006).

[22] C. Thelander, T. Martensson, M. T. Bjrk, B. J. Ohlsson, M. W. Larsson, L. R. Wallenberg, and L. Samuelson, *Single-electron transistors in heterostructure nanowires*, Appl. Phys. Lett. 83, 2052 (2003).

[23] A. R. Guichard, D. N. Barsic, S. Sharma, T. I. Kamins, M. L. Brongersma, *Tunable Light Emission from Quantum-Confined Excitons in $TiSi_2$-Catalyzed Silicon Nanowires*, Nano Lett. 6, 2140-2144 (2006).

[24] L. Yang, J. Motohisa, J. Takeda, K. Tomioka, T. Fukui, *Size-dependent photoluminescence of hexagonal nanopillars with single InGaAs/GaAs quantum wells fabricated by selective-area metal organic vapor phase epitaxy*, Appl. Phys. Lett. 89, 203110 (2006).

[25] Y. Cui, Q. Wei, H. Park, C. M. Lieber, *Nanowire Nanosensors for Highly-Sensitive, Selective and Integrated Detection of Biological and Chemical Species*, Science 293, 1289-1292 (2001).

[26] W. Lu, C. M. Lieber, *Nanoelectronics from the bottom up*, Nat. Mater. 6, 841–850 (2007).

[27] C. Thelander, H. A. Nilsson, L. E. Jensen, L. Samuelson, *Nanowire Single-Electron Memory*, Nano Lett. 5, 635-638 (2005).

[28] F. Glas, *A simple calculation of energy changes upon stacking fault formation or local crystalline phase transition in semiconductors*, J. Appl. Phys. 104, 093520 (2008).

[29] M.C. Plante, R.R. LaPierre, *Au-assisted growth of GaAs nanowires by gas source molecular beam epitaxy: Tapering, sidewall faceting and crystal structure*, Journal of Crystal Growth 310, 356 (2008).

[30] V. G. Dubrovskii, N. V. Sibirev, G. E. Cirlin, M. Tchernycheva, J. C. Harmand, and V. M. Ustinov, *Shape modification of III-V nanowires: The role of nucleation on sidewalls*, Phys. Rev. E 77, 031606 (2008).

[31] H. J. Joyce, J. Wong-Leung, Q. Gao, H. H. Tan and C. Jagadish, *Phase Perfection in Zinc Blende and Wurtzite III−V Nanowires Using Basic Growth Parameters*, Nano Lett. 10, 908 (2010).

[32] H. J. Joyce, Q. Gao, H. Hoe Tan, C. Jagadish, Y. Kim, X. Zhang, Y.Guo and J. Zou, *Twin-Free Uniform Epitaxial GaAs Nanowires Grown by a Two-Temperature Process*, Nano Lett. 7, 921 (2007).

[33] F. Glas, J. C. Harmand, G. Patriarche, *Why Does Wurtzite Form in Nanowires of III-V Zinc Blende Semiconductors?*, Phys. Rev. B 99, 146101 (2007).

[34] V. G. Dubrovskii, N. V. Sibirev, G. E. Cirlin, A. D. Bouravleuv, Yu. B. Samsonenko, D. L. Dheeraj, H. L. Zhou, C. Sartel, J. C. Harmand, G. Patriarche, and F. Glas, *Role of nonlinear effects in nanowire growth and crystal phase*, Phys. Rev. B 80, 205305 (2009).

[35] M. Tchernycheva, L. Travers, G. Patriarche, F. Glas, J. C. Harmand, G. E. Cirlin, and V. G. Dubrovskii, *Au-assisted molecular beam epitaxy of InAs nanowires: Growth and theoretical analysis*, J. Appl. Phys. 102, 094313 (2007).

[36] V. G. Dubrovskii, N. V. Sibirev, G. E. Cirlin, I. P. Soshnikov, W. H. Chen, R. Larde, E. Cadel, P. Pareige, T. Xu, B. Grandidier, J.-P. Nys, D. Stievenard, M. Moewe, L. C. Chuang, C. Chang-Hasnain, *Gibbs-Thomson and diffusion-induced contributions to the growth rate of Si, InP, and GaAs nanowires*, Phys. Rev. B 79, 205316 (2009).

[37] M. C. Plante and R. R. LaPierre, *Analytical description of the metal-assisted growth of III–V nanowires: Axial and radial growths*, J. Appl. Phys. 105, 114304 (2009).

[38] J.C. Harmand, F. Glas, G. Patriarche, *Growth kinetics of a single* $InP_{1-x}As_x$ *nanowire*, Phys. Rev. B 81, 235436 (2010).

[39] V. G. Dubrovskii, G. E. Cirlin, I. P. Soshnikov, A. A. Tonkikh, N. V. Sibirev, Yu. B. Samsonenko, and V. M. Ustinov, *Diffusion-induced growth of GaAs nanowhiskers during molecular beam epitaxy: Theory and experiment*, Phys. Rev. B 71, 205325 (2005).

[40] V.G. Dubrovskii, N.V. Sibirev, *General form of the dependences of nanowire growth rate on the nanowire radius*, Journal of Crystal Growth, 304, 504 (2007).

[41] V.G. Dubrovskii, N.V. Sibirev, R.A. Suris, G.E. Cirlin, J.C. Harmand, V.M. Ustinov, *Diffusion-controlled growth of semiconductor nanowires: Vapor pressure versus high vacuum deposition*, Surface Science 601, 4395 (2007).

[42] V. G. Dubrovskii, N. V. Sibirev, J. C. Harmand, F. Glas, *Growth kinetics and crystal structure of semiconductor nanowires*, Phys. Rev. B 78, 235301 (2008).

[43] F. Glas and J. C. Harmand, *Calculation of the temperature profile in nanowhiskers growing on a hot substrate*, Phys. Rev. B 73, 155320 (2006).

[44] M. C. Plante and R. R. LaPierre, Control of GaAs nanowire morphology and crystal structure, Nanotechnology 19, 495603 (2008).

[45] J. C. Harmand, G. Patriarche, N. Péré-Laperne, M-N. Mérat-Combes, L. Travers, F. Glas, *Analysis of vapor-liquid-solid mechanism in Au-assisted GaAs nanowire growth*, Appl. Phys. Lett. 87, 203101 (2005).

[46] K. A. Dick, P. Caroff, J. Bolinsson, M. E. Messing, J. Johansson, K. Deppert, L. R. Wallenberg, L. Samuelson, *Control of III–V nanowire crystal structure by growth parameter tuning*, Semicond. Sci. Technol. 25, 024009 (2010).

[47] D. Spirkoska, J. Arbiol, A. Gustafsson, S. Conesa-Boj, F. Glas, I. Zardo, M. Heigoldt, M. H. Gass, A. L. Bleloch, S. Estrade, M. Kaniber, J. Rossler, F. Peiro, J. R. Morante, G. Abstreiter, L. Samuelson, A. Fontcuberta i Morral, *Structural and optical properties of high quality zinc-blende/wurtzite GaAs nanowire heterostructures*, Phys. Rev. B 80, 245325 (2009).

[48] N. S. Dellas, J. Liang, B. J. Cooley, N. Samarth, S. E. Mohney, *Electron microscopy of GaAs/MnAs core/shell nanowires*, Appl. Phys. Lett. 97, 072505 (2010).

[49] M. Hilse, Y. Takagaki, J. Herfort, M. Ramsteiner, C. Herrmann, S. Breuer, L. Geelhaar, H. Riechert, *Ferromagnet-semiconductor nanowire coaxial heterostructures grown by molecular-beam epitaxy*, Appl. Phys. Lett. 95, 133126 (2009).

[50] M. I. van der Meulen, N. Petkov, M. A. Morris, O. Kazakova, X. Han, K. L. Wang, A. P. Jacob, J. D. Holmes, *Single Crystalline* $Ge_{1-x}Mn_x$ *Nanowires as Building Blocks for Nanoelectronics*, Nano Lett. 9, 50-56 (2009).

[51] Y. C. Lin, Y. Chen, A. Shailos, Y. Huang, *Detection of Spin Polarized Carrier in Silicon Nanowire with Single Crystal MnSi as Magnetic Contacts*, Nano Lett. 10, 2281-2287 (2010).

[52] M. Soda, A. Rudolph, D. Schuh, J. Zweck, D. Bougeard, E. Reiger, *Transition from Au to pseudo Ga-catalyzed growth mode observed in GaAs nanowires grown by MBE*, submitted to Phys. Rev. B.

[53] C. Thelander, P. Agarwal, S. Brongersma, J. Eymery, L. F. Feiner, A. Forchel, M. Scheer, W. Riess, B. J. Ohlsson, U. Gosele, and L. Samuelson, *Nanowire-based one-dimensional electronics*, Materials Today 9, 28 (2006).

[54] L. J. Lauhon, M. S. Gudiksen, D. Wang, C. M. Lieber, *Epitaxial core–shell and core–multishell nanowire heterostructures*, Nature 420, 57 (2002).

[55] D. Wang, F. Quian, C. Yang, Z. Zhong, C. M. Lieber, *Rational Growth of Branched and Hyperbranched Nanowire Structures*, NanoLetters 4, 871–874 (2004).

[56] T. Dietl, H. Ohno, F. Matsukura, J. Cibert, and D. Ferrand, *Zener Model Description of Ferromagnetism in Zinc-Blende Magnetic Semiconductors*, Science 287, 1019 (2000).

[57] T. Dietl, A. Haury, and Y. Merle d'Aubigné, *Free carrier-induced ferromagnetism in structures of diluted magnetic semiconductors*, Phys. Rev. B 55, R3347 (1997).

[58] N. W. Ashcroft and N. D. Mermin, *Electronic properties of Doped Semiconductors*, Saunders College Publishing, Philadelphia (1976).

[59] H. Ohno, *Making Nonmagnetic Semiconductors Ferromagnetic*, Science 281, 951 (1998).

[60] M. Sawicki, K.-Y. Wang, K. W. Edmonds, R. P. Campion, C. R. Staddon, N. R. S. Farley, C. T. Foxon, E. Papis, E. Kaminska, A. Piotrowska, T. Dietl, and B. L. Gallagher, *In-plane uniaxial anisotropy rotations in (Ga,Mn)As thin films*, Phys. Rev. B 71, 121302 (2005).

[61] K. Pappert, S. Hümpfner, J. Wenisch, K. Brunner, C. Could, G. Schmidt, and L. Molenkamp, *Transport characterization of the magnetic anisotropy of (Ga,Mn)As*, Appl. Phys. Lett. 90, 062109 (2007).

[62] G. Schmidt, D. Ferrand, L. W. Molenkamp, A. T. Filip, B. J. van Wees, *Fundamental obstacle for electrical spin injection from a ferromagnetic metal into a diffusive semiconductor*, Phys. Rev. B 62, R4790 (2000).

[63] M. Ciorga, C. Wolf, A. Einwanger, M. Utz, D. Schuh, D. Weiss, *Local spin valve effect in lateral (Ga,Mn)As/GaAs spin Esaki diode devices*, AIP Advances 1, 022113 (2011).

[64] A. Rudolph, M. Soda, M. Kiessling, T. Wojtowicz, D. Schuh, W. Wegscheider, J. Zweck, C. Back, E. Reiger, *Ferromagnetic GaAs/GaMnAs Core-Shell Nanowires Grown by Molecular Beam Epitaxy*, Nano Lett. 9, 3860-3866 (2009).

[65] C. H. Butschkow, S. Geißler, A. Rudolph, M. Soda, E. Reiger, D. Schuh, G. Woltersdorf, W. Wegscheider, D. Weiss, *Magnetoresistance of individual ferromagnetic GaAs/(Ga,Mn)As core-shell nanowires*, submitted.

[66] V. Novák, K. Olejník, J. Wunderlich, M. Cukr, K. Výborný, A. W. Rushforth, K. W. Edmonds, R. P. Campion, B. L. Gallagher, Jairo Sinova, T. Jungwirth, *Curie Point Singularity in the Temperature Derivative of Resistivity in (Ga,Mn)As*, Phys. Rev. Lett. 101, 077201 (2008).

[67] T. Ando, Y. Arakawa, K. Furuya, S. Komiyama, H. Nakashima, *Mesoscopic Physics and Electronics*, Springer (1998).

[68] G. Schmid, *Nanotechnology*, Wiley-VCM (2008).

[69] L. Samuelson, *Self forming nanoscale devices*, Materials Today 6, 22 (2003).

[70] M. A. Reed, J. N. Randall, R. J. Aggarwal, R. J. Matyi, T. M. Moore, and A. E. Wetsel, *Observation of discrete electronic states in a zero-dimensional semiconductor nanostructure*, Phys. Rev. Lett. 60, 535 (1988).

[71] M. Borgström, K. Deppert, L. Samuelson and W. Seifert, *Size- and shape-controlled GaAs nano-whiskers grown by MOVPE: a growth study*, Journal of Crystal Growth 260, 18 (2004).

[72] S. Kodambaka, J. Tersoff, M. C. Reuter, and F. M. Ross, *Diameter-Independent Kinetics in the Vapor-Liquid-Solid Growth of Si Nanowires*, Phys. Rev. Lett. 96, 096105 (2006).

[73] P. Paiano, P. Prete, N. Lovergine, and A. M. Mancini, *Size and shape control of GaAs nanowires grown by metalorganic vapor phase epitaxy using tertiarybutylarsine*, J. Appl. Phys. 100, 094305 (2006).

[74] A. I. Persson, L. E. Fröberg, S. Jeppesen, M. T. Björk, and L. Samuelson, *Surface diffusion effects on growth of nanowires by chemical beam epitaxy*, J. Appl. Phys. 101, 034313 (2007).

[75] M. A. Verheijen, G. Immink, T. de Smet, M. T. Borgström, and E. P. A. M. Bakkers, *Growth Kinetics of Heterostructured GaP−GaAs Nanowires*, J. Am. Chem. Soc. 128 (4), 1353 (2006).

[76] R. Veresegyházya, I. Mojzesa and B. Pécza, *Comparative mass spectrometric study of* A^{III}*-*B^{V} *compounds covered with a gold layer*, Vacuum 36, 547 (1986).

[77] C. J. Cooke, W. Hume-Rothery, *The equilibrium diagram of the system gold-gallium*, Journal of the Less Common Metals 10, 42 (1966).

[78] S. E. R. Hiscocks and W. Hume-Rothery, *The Equilibrium Diagram of the System Gold-Indium*, Proc. R. Soc. Lond. 282, 318 (1964).

[79] C. Chatillon, F. Hodaj, A. Pisch, *Thermodynamics of GaAs nanowire MBE growth with gold droplets*, J. Crystal Growth 311, 3598 (2009).

[80] M. Mattila, T. Hakkarainen, H. Lipsanen, *Catalyst-free fabrication of InP and InP(N) nanowires by metalorganic vapor phase epitaxy*, Journal of Crystal Growth 298, 640 (2007).

[81] S. N. Mohammad, *Self-catalysis: A contamination-free, substrate-free growth mechanism for single-crystal nanowire and nanotube growth by chemical vapor deposition*, J. Chem. Phys. 125, 094705 (2006).

[82] C.J. Novotny and P. K. L. Yu, *Vertically aligned, catalyst-free InP nanowires grown by metalorganic chemical vapor deposition*, Appl. Phys. Lett. 87, 203111 (2005).

[83] B. Mandl, J. Stangl, T. Mårtensson, A. Mikkelsen, J. Eriksson, L. S. Karlsson, G. Bauer, L. Samuelson, and W. Seifert, *Au-Free Epitaxial Growth of InAs Nanowires*, Nano Lett. 6, 1817 (2006).

[84] J. E. Allen, E. R. Hemesath, D. E. Perea, J. L. Lensch-Falk, Z.Y. Li, F. Yin, M. H. Gass, P. Wang, A. L. Bleloch, R. E. Palmer, L. J. Lauhon, *High-resolution detection of Au catalyst atoms in silicon nanowires*, Nature Nanotechnology 3, 168 (2008).

[85] K. W. Kolasinski, *Catalytic growth of nanowires: Vapor–liquid–solid, vapor–solid–solid, solution–liquid–solid and solid–liquid–solid growth*, Current Opinion in Solid State and Materials Science 10, 182 (2006).

[86] B. A. Wacaser, K. A. Dick, J. Johansson, M. T. Borgström, K. Deppert and L. Samuelson, *Preferential Interface Nucleation: An Expansion of the VLS Growth Mechanism for Nanowires*, Advanced Materials 21, 153 (2009).

[87] I. V. Markov, *Crystal Growth for Beginners: Fundamentals of Nucleation, Crystal Growth and Epitaxy* 2nd Edition, World Scientific (2003).

[88] P. Cheyssac, M. Sacilotti, and G. Patriarche, *Vapor-liquid-solid mechanisms: Challenges for nanosized quantum cluster/dot/wire materials*, J. Appl. Phys. 100, 044315 (2006).

[89] V. A. Nebol'sin and A. A. Shchetinin, *Role of Surface Energy in the Vapor–Liquid–Solid Growth of Silicon*, Inorganic Materials 39, 899 (2003).

[90] M.H. Magnusson, K. Deppert, J.-O. Malm, J.-O. Bovin and L. Samuelson, *Gold nanoparticles: Production, reshaping, and thermal charging*, Journal of Nanoparticle Research 1, 243 (1999).

[91] T Mårtensson, M Borgström, W Seifert, B J Ohlsson and L Samuelson, *Fabrication of individually seeded nanowire arrays by vapour–liquid–solid growth*, Nanotechnology 14, 1255 (2003).

[92] N.N. Ledenstov, *Growth Process and Surface Phase Equilibria in Molecular Beam Epitaxy*, Springer-Verlag Berlin Heidelberg (1999).

[93] M. Tchernycheva, J. C. Harmand, G. Patriarche, L. Travers, G. E. Cirlin, *Temperature conditions for GaAs nanowire formation by Au-assisted molecular beam epitaxy*, Nanotechnology 17, 4025 (2006).

[94] A. T. Galisultanov, I. A. Fedorov, N. V. Sibirev, I. P. Soshnikov, and V. G. Dubrovskii, *Effect of growth atmosphere on the temperature profile along a nanowhisker* , Tech. Phys. Lett. 34, 512 (2008).

[95] C. Sartel, D. L. Dheeraj, F. Jabeen, J. C. Harmand, *Effect of arsenic species on the kinetics of GaAs nanowires growth by molecular beam epitaxy*, Journal of Crystal Growth 312, 2073-2077 (2010).

[96] K. W. Schwarz and J. Tersoff, *From Droplets to Nanowires: Dynamics of Vapor-Liquid-Solid Growth*, Phys. Rev. Lett. 102, 206101 (2009).

[97] H. Shtrikman, R. Popovitz-Biro, A. Kretinin, and M. Heiblum, *Stacking-Faults-Free Zinc Blende GaAs Nanowires*, Nano Lett. 9, 215 (2009).

[98] C.-Y. Yeh, Z. W. Lu, S. Froyen, and A. Zunger, *Zinc-blende–wurtzite polytypism in semiconductors*, Phys. Rev. B 46, 10086 (1992).

[99] W. T. Read, *Dislocation in crystals*, McGraw-Hill (1953).

[100] R. Leitsmann and F. Bechstedt, *Surface influence on stability and structure of hexagon-shaped III-V semiconductor nanorods*, J. Appl. Phys. 102, 063528 (2007).

[101] T. Akiyama, K. Sano, K. Nakamura and T. Ito, *An Empirical Potential Approach to Wurtzite–Zinc-Blende Polytypism in Group III–V Semiconductor Nanowires*, Jpn. J. Appl. Phys. 45, L275 (2006).

[102] G. E. Cirlin, V. G. Dubrovskii, Yu. B. Samsonenko, A. D. Bouravleuv, K. Durose, Y. Y. Proskuryakov, B. Mendes, L. Bowen, M. A. Kaliteevski, R. A. Abram, D. Zeze, *Self-catalyzed, pure zincblende GaAs nanowires grown on Si(111) by molecular beam epitaxy*, Phys. Rev. B 82, 035302 (2010).

[103] Q. Xiong, J. Wang, and P. C. Eklund, *Coherent Twinning Phenomena: Towards Twinning Superlattices in III–V Semiconducting Nanowires*, Nano Lett. 6, 2736 (2006).

[104] B. A. Wacaser, K. Deppert, L. S. Karlsson, L. Samuelson, W. Seifert, *Growth and characterization of defect free GaAs nanowires*, Journal of Crystal Growth 287, 504 (2006).

[105] M. Ilegems, R. Dingle, and L. W. Rupp Jr., *Optical and electrical properties of Mn-doped GaAs grown by molecular-beam epitaxy*, J. Appl. Phys. 46, 3059 (1975).

[106] H. Ohno, A. Shen, F. Matsukura, A. Oiwa, A. Endo, S. Katsumoto, and Y. Iye, *(Ga,Mn)As: A new diluted magnetic semiconductor based on GaAs*, Appl. Phys. Lett. 69, 363 (1996).

[107] M. Reinwald, *Herstellung und Charakterisierung von ferromagnetischem GaMnAs auf der GaAs (001)- und (311)A-Oberfläche*, Dissertation, Universität Regensburg (2006).

[108] U. Wurstbauer, *Herstellung und Charakterisierung von Mangan dotierten III-V Halbleiterheterostrukturen*, Dissertation, Universität Regensburg (2008).

[109] M. Kaminska, Z. Liliental-Weber, E. R. Weber, T. George, J. B. Kortright, F. W. Smith, B.-Y. Tsaur, and A. R. Calawa, *Structural properties of As-rich GaAs grown by molecular beam epitaxy at low temperatures*, Appl. Phys. Lett. 54, 1881 (1989).

[110] X. Liu, A. Prasad, J. Nishio, and E. R. Weber, *Native point defects in lowtemperature-grown GaAs*, Appl. Phys. Lett. 67, 279 (1995).

[111] S. Sanvito, G. Theurich, and N. Hill, *Density Functional Calculations for III–V Diluted Ferromagnetic Semiconductors: A Review*, J. Supercond. 15, 85 (2002).

[112] K. M. Yu, W. Walukiewcz, T. Wojtowicz, I. Kuryliszyn, X. Liu, Y. Sasaki, and J. K. Furdyna, *Effect of the location of Mn sites in ferromagnetic $Ga_{1-x}Mn_xAs$ on its Curie temperature*, Phys. Rev. B 65, 201303 (2002).

[113] F. Máca and J. Mašek, *Electronic states in $Ga_{1-x}Mn_xAs$: Substitutional versus interstitial position of Mn*, Phys. Rev. B 65, 235209 (2002).

[114] S. C. Erwin and A. G. Petukhov, *Self-Compensation in Manganese-Doped Ferromagnetic Semiconductors*, Phys. Rev. Lett. 89, 227201 (2002).

[115] J. Blinowski, P. Kacman, *Spin interactions of interstitial Mn ions in ferromagnetic GaMnAs*, Phys. Rev. B 67, 121204 (2003).

[116] J. De Boeck, R. Oesterholt, A. Van Esch, H. Bender, C. Bruynseraede, C. Van Hoof, and G. Borghs, *Nanometer-scale magnetic MnAs particles in GaAs grown by molecular beam epitaxy*, Appl. Phys. Lett. 68, 2744 (1996).

[117] M. Sperl, *Magnetische Eigenschaften von (Ga,Mn)As-Schichten und Fe/(Ga,Mn)As-Hybridstructuren*, Dissertation, Universität Regensburg (2009).

[118] T. Hayashi, Y. Hashimoto, S. Katsumoto, and Y. Iye, *Effect of low-temperature annealing on transport and magnetism of diluted magnetic semiconductor (Ga, Mn)As*, Appl. Phys. Lett. 78, 1691 (2001).

[119] K. W. Edmonds, P. Boguslawski, K. Y. Wang, R. P. Campion, S. N. Novikov, N. R. S. Farley, B. L. Gallagher, C. T. Foxon, M. Sawicki, T. Dietl, M. Buongiorno Nardelli, and J. Bernholc, *Mn Interstitial Diffusion in (Ga,Mn)As*, Phys. Rev. Lett. 92, 037201 (2004).

[120] K. C. Ku, S.J. Potashnik, R. F. Wang, S. H. Chun, P. Schiffer, N. Samarth, M. J. Seong, A. Mascarenhas, E. Johnston-Halperin, R. C. Meyers, A. C. Gossard, and D. D. Awschalom, *Highly enhanced Curie temperature in low-temperature annealed [Ga,Mn]As epilayers*, Appl. Phys. Lett. 82, 2302 (2003).

[121] D. Chiba, K. Takamura, F. Matsukura, and H. Ohno, *Effect of low-temperature annealing on (Ga,Mn)As trilayer structures*, Appl. Phys. Lett. 82, 3020 (2003).

[122] S. J. Potashnik, K. C. Ku, S. H. Chun, J. J. Berry, N. Samarth, and P. Schiffer, *Effects of annealing time on defect-controlled ferromagnetism in $Ga_{1-x}Mn_xAs$*, Appl. Phys. Lett. 79, 1495 (2001).

[123] S. J. Potashnik, K. C. Ku, R. Mahendiran, S. H. Chun, R. F. Wang, N. Samarth, and P. Schiffer, *Saturated ferromagnetism and magnetization deficit in optimally annealed $Ga_{1-x}Mn_xAs$ epilayers*, Phys. Rev. B 66, 012408 (2002).

[124] M. A. Herman, Epitaxy, *Physical Priciples and Technical Implementation*, Springer-Verlag Berlin Heidelberg (2004).

[125] F. Glas, *Nanowire growth mechanism and their impact on morphology, crystal structure, extended defects and heterostructure formation*, NODE summer school on semiconductor nanowires, Cortona (2008).

[126] D. Spirkoska, G. Abstreiter and A. Fontcuberta i Morral, *GaAs nanowires and related prismatic heterostructures*, Semicond. Sci. Technol. 24 113001 (2009).

[127] D. B. Williams and C. B. Carter, *Transmission Electron Microscopy, A Textbook for Materials Science*, Plenum Press, New York (1996).

[128] Y. M. Parka, D.-S. Koa, K.-W. Yia, I. Petrovb, Y.-W. Kima, *Measurement and estimation of temperature rise in TEM sample during ion milling*, Ultramicroscopy 107, 663 (2007).

[129] J. Bill, Diploma thesis, Universität Regensburg (2011).

[130] Reichert-Jung Optische Werke AG Austria, *ULTRACUT E, Gebrauchsanweisung*, A Cambridge Instruments Company.

[131] L. Reimer, *Transmission Electron Microscopy, Physics of Image Formation and Microanalysis, 4th Edition*, Springer-Verlag Berlin Heidelberg (1997).

[132] R. F. Egerton, *Electron Energ-Loss Spectroscopy in the Electron Microscope, second edition*, Plenum Press, New York (1996).

[133] F. J. Heinrich, *Electron Beam X-ray Microanalysis*, Van Nostrand Reinhold Company, New York (1981).

[134] J. C. Harmand, G. Patriarche, N. Péré-Laperne, M-N. Mérat-Combes, L. Travers, F. Glas, *Analysis of vapor-liquid-solid mechanism in Au-assisted GaAs nanowire growth*, Appl. Phys. Lett. 87, 203101 (2005).

[135] J.C. Harmand, F. Glas, G. Patriarche, *Growth kinetics of a single $InP_{1-x}As_x$ nanowire*, Phys. Rev. B 81, 235436 (2010).

[136] F. Glas, J. C. Harmand, G. Patriarche, *Nucleation Antibunching in Catalyst-Assisted Nanowire Growth*, Phys. Rev. Lett. 104, 135501 (2010).

[137] N. V. Sibirev, M. A. Timofeeva, A. D. Bol'shakov, M. V. Nazarenko and V. G. Dubrovskiĭ, *Surface energy and crystal structure of nanowhiskers of III–V semiconductor compounds*, Physics of the Solid State 52, 1531-1538 (2010).

[138] F.Glas, *Chemical potentials for Au-assisted vapor-liquid-solid growth of III-V nanowires*, J. Appl. Phys. 108, 073506 (2010).

[139] J. Y. Guo, Y. W. Zhang, V. B. Shenoy, *Morphological Evolution and Ordered Quantum Structure Formation in Heteroepitaxial Core-Shell Nanowires*, ACS Nano 4, 4455 (2010).

[140] H. Wang, M. Upmanyu, C. V. Ciobanu, *Morphology of Epitaxial Core–Shell Nanowires*, Nano Lett. 8, 4305 (2008).

[141] R. F. Sekerka, *Equilibrium and growth shapes of crystals: how do they differ and why should we care?*, Cryst. Res. Technology. 40, 291 (2005).

[142] M. Ozdemir, A. Zangwill, *Morphological equilibration of a facetted crystal*, Phys. Rev. B 45, 3718 (1992).

[143] N. Sköld, J. B. Wagner, G. Karlsson, T. Hernán, W. Seifert, M. Pistol, and Lars Samuelson, *Phase Segregation in AlInP Shells on GaAs Nanowires*, Nano Lett. 6, 2743-2747 (2006).

[144] J. B. Wagner, N. Sköld, L. R. Wallenberg, L. Samuelson, *Growth and segregation of GaAs–AlxIn1–xP core-shell nanowires*, Journal of Crystal Growth 312, 1755-1760 (2010).

[145] M. A. Hermann, T. G. Andersson, *Morphological Stability in Epitaxy of Semiconductors - Application to Optoelectronic Monolithically Integrated Structures*, Appl. Ohys. A 41, 243 (1986).

[146] G. Biasiol and E. Kapon, *Mechanisms of Self-Ordering of Quantum Nanostructures Grown on Nonplanar Surfaces*, Phys. Rev. Lett. 81, 2962-2965 (1998).

[147] G. Biasiol, A. Gustafsson, K. Leifer, and E. Kapon, *Mechanisms of self-ordering in nonplanar epitaxy of semiconductor nanostructures*, Phys. Rev. B 65, 205306 (2002).

Grazie a...

... diejenige die das Entstehen dieser Arbeit ermöglicht haben, und mich in jeder Hinsicht unterstützt haben.
Insbesondere möchte ich Danke sagen an...

... Joe, der mich in seiner Arbeitsgruppe aufgenommen und all diese Jahre unterstützt hat

... Olga, für die endlose Gespräche bezüglich... alles!

... Martin Beer, für die gemeinsamen Reisen um das Globus, mit und ohne Meriva!! Gell *coach*...!?

... allen ehmaligen und aktuellen Mitglieder der TEM-Truppe

... allen ehmaligen und aktuellen Mitglieder der AG Back und AG Bayreuther

... Matthias Sperl, für die Profi-Betreuung in Fragen Magnetismus, und das Abnehmen von Olivenöl!

... allen Synchrotron-Teams für die tolle geleistete Arbeit in Trieste und Grenoble und vor allem an Francesco Maccherozzi und Matthias Sperl; auch an Laura Felisari die sich um unseres Überleben gekümmert hat

... an Christian Back für die Möglichkeit nach Trieste und Grenoble fahren zu dürfen

... an Daniel Wolf der TU Dresden für die Tomographie-Holographie Messungen am Triebenberg: 1D Nanostructuren in 3D...!? ;-)

... an Elisabeth Reiger für die Zusammenarbeit und ein immer offenes Ohr für meine *Theorien*

... an Joe, Dominique Bougeard, Elisabeth Reiger, Andreas Rudolph, Matthias Sperl, Johannes Thalmair und Martin Beer für das Korrekturlesen

... an meinen Lieblingsitalienern am Lehrstuhl, Federico & Eduardo, für alle gemeinsame außeruniversitäre Erlebnisse

... und an allen Freunde und Bekannte die mich in diesen Jahren begleitet haben, inklusive alle Mitbewohner die ich durch fünf mal Umziehen hatte

Grazie a...

... diejenige die das Entstehen dieser Arbeit ermöglicht haben, und mich in jeder Hinsicht unterstützt haben.
Insbesondere möchte ich Danke sagen an...

... Joe, der mich in seiner Arbeitsgruppe aufgenommen und all diese Jahre unterstützt hat

... Olga, für die endlose Gespräche bezüglich... alles!

... Martin Beer, für die gemeinsamen Reisen um das Globus, mit und ohne Meriva!! Gell *coach*...!?

... allen ehmaligen und aktuellen Mitglieder der TEM-Truppe

... allen ehmaligen und aktuellen Mitglieder der AG Back und AG Bayreuther

... Matthias Sperl, für die Profi-Betreuung in Fragen Magnetismus, und das Abnehmen von Olivenöl!

... allen Synchrotron-Teams für die tolle geleistete Arbeit in Trieste und Grenoble und vor allem an Francesco Maccherozzi und Matthias Sperl; auch an Laura Felisari die sich um unseres Überleben gekümmert hat

... an Christian Back für die Möglichkeit nach Trieste und Grenoble fahren zu dürfen

... an Daniel Wolf der TU Dresden für die Tomographie-Holographie Messungen am Triebenberg: 1D Nanostructuren in 3D...!? ;-)

... an Elisabeth Reiger für die Zusammenarbeit und ein immer offenes Ohr für meine *Theorien*

... an Joe, Dominique Bougeard, Elisabeth Reiger, Andreas Rudolph, Matthias Sperl, Johannes Thalmair und Martin Beer für das Korrekturlesen

... an meinen Lieblingsitalienern am Lehrstuhl, Federico & Eduardo, für alle gemeinsame außeruniversitäre Erlebnisse

... und an allen Freunde und Bekannte die mich in diesen Jahren begleitet haben, inklusive alle Mitbewohner die ich durch fünf mal Umziehen hatte